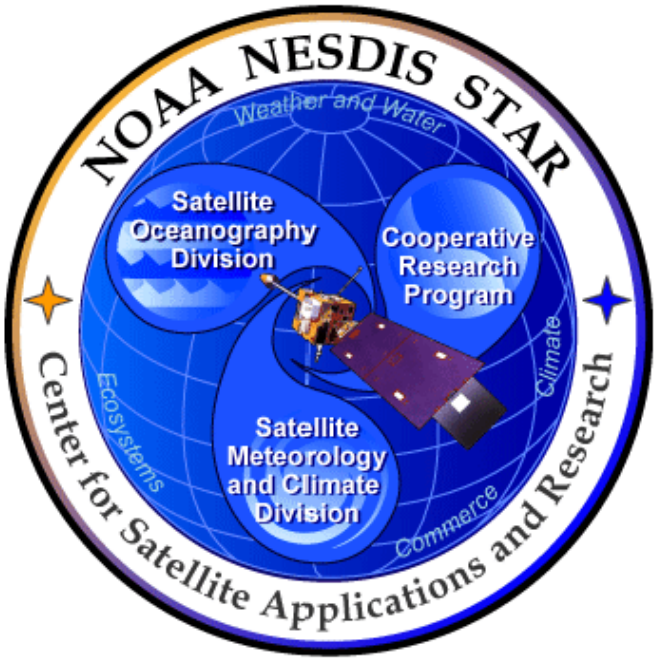


# The NOAA Unique CrIS/ATMS Processing System (NUCAPS): Algorithm Theoretical Basis Documentation

Prepared by
Antonia Gambacorta

antonia.gambacorta@noaa.gov
NOAA Center for Weather and Climate Prediction (NCWCP)
5830 University Research Court 2nd Floor, Office 2684 College Park, MD 20740-3818 USA
phone: 301-613-3539

Version 1.0
August 21, 2013

# Contents

# List of Figures

# List of Tables

# Chapter 1

# Introduction

Launched on board the Joint Polar Satellite System (JPSS) Suomi National Polar-orbiting Partnership (NPP) platform on October 28th 2011, the Cross-track Infrared Sounder and the Advanced Technology Microwave Sounder represent the US next generation of polar-orbiting operational hyper spectral sounders.

The Cross-track Infrared Sounder (CrIS) is a Fourier transform spectrometer with a total of 1305 infrared sounding channels covering the longwave (655-1095 $cm^{-}1$), midwave (1210-1750 $cm^{-}1$), and shortwave (2155-2550 $cm^{-}1$) spectral regions. The Advanced Technology Microwave Sounder (ATMS) is a cross-track scanner with 22 channels in spectral bands from 23 GHz through 183 GHz. These two instruments together represent the latest addition to a long series of atmospheric satellite sounders that originated in the late 1970's (http://www.ipo.noaa.gov). This suite of instruments has been designed to guarantee continuity to the 1:30am/pm equatorial crossing time orbit, in replacement of the AIRS/AMSU instruments on board the NASA Aqua satellite and in conjunction with the European MetOp satellite series operating the mid-morning orbit. Specifically, CrIS has been designed to continue the advances in atmospheric observations and research that started with the Atmospheric InfraRed Sounder (AIRS) launched on the Aqua platform in 2002 (Aumann et al., 2033) and followed by the Infrared Atmospheric Sounding Interferometer (IASI), launched on the MetOp-A platform in 2006 (http://smsc.cnes.fr/IASI/). ATMS will similarly continue the series of observations that started with the Advanced Microwave Sounding Unit (AMSU) first launched by NOAA in 1998 [reference here].

In this document we describe the algorithm theoretical basis of the NOAA Unique CrIS/ATMS Processing System (NUCAPS). NUCAPS is a heritage algorithm of the AIRS Science Team algorithm (Susskind, Barnet, Blaisdell, 2003), in operations since 2002. The NOAA/NESDIS/STAR implementation of this algorithm is a modular architecture that was specifically designed to be compatible with multiple instruments: the same retrieval algorithm and the same underlying spectroscopy are currently used to process the AIRS/AMSU suite, the IASI/AMSU/MHS suite (operationally since 2008) and now the CrIS/ATMS suite (approved for operations in January 2013). The robustness of this system has allowed first light results to be available at an early stage (6 months after launch) of the Suomi NPP post launch mission (Gambacorta et al., 2012a, 2012b, 2012).

NUCAPS suite of products includes two different files in NETCDF format: the Standard Product and the Cloud-Cleared Radiance Product. The Standard Product consists of retrieved estimates of hydrological variables such as temperature, water vapor, cloud fraction and cloud top pressure, along with trace gas retrievals such as ozone, methane, carbon monoxide, carbon dioxide, $SO_2$, $N_2O$, and $HNO_3$, and a flag indicating the presence of dust and volcano emission. The vertical sampling of each retrieved atmospheric profile variable consists of 100 points total between 1100 mb

and 0.016 mb; Intermediate solutions from the microwave only step and the regression first guess are also part of the delivered standard output. Full spectrum Cloud-Cleared Radiances are produced along with the Standard Product, as they are the radiances used to retrieve the Standard Product. Both the Standard Product and the cloud-cleared radiance file are generated at all locations where the atmospheric soundings are taken.

Each product file encompasses one *granule* of CrIS/ATMS data. Granules are formally defined as the smallest cluster of data that is independently managed (i.e., described, inventoried, retrievable). A NUCAPS granule has been set as 32 seconds of data, corresponding to 4 scan lines of CrIS/ATMS data. Each scans contains 32 Fields of Regard (FOR) viewed on the Earth's surface with a scan width of 50. Each FOR contains a simultaneously measured 3X3 set of Fields of View (FOVs). The CrIS FOVs are circular and have a diameter of 14 km at nadir. The UTC start time of the N-th granule of each data is (146+(N-1)*360)/3600 hours.

Granule products are operationally accessible to the science community in near real time (i.e only a 3 hour delay from the raw data acquisition) through the CLASS environment. Detailed information on the NUCAPS product requirements including content, format, latency and quality can be found in the NUCAPS Requirements Allocation Document (RAD) (NESDIS/STAR, 2011) which is available in the NUCAPS project artifact repository.

This document is divided into multiple chapters. Chapter 2 describes the attributes of the CrIS and ATMS sensing system. Chapter 3 introduces a general description of the algorithm. Chapter 4 describes the algorithm inputs. Chapter 5 describes the microwave module component of the algorithm. Chapter 6 describes the regression module for both the cloud clearing input profile and the first guess. Chapter 7 is dedicated to cloud clearing. Chapter 8 describes the physical and mathematical basis of the algorithm, along with the technical characteristics of the algorithm processing flow.

## 1.1 References

ATMS (2013), The Advanced technology Microwave Sounder, http://www.ipo.noaa.gov.

CLASS, The Comprehensive Large Array-data Stewardship System , www.class.noaa.gov.

CrIS (2013), The cross-track infrared sounder, http://www.ipo.noaa.gov.

JPSS (2013), The joint polar satellite system, www.jpss.noaa.gov/.

Gambacorta, A. and Barnet, C.D. and Wolf, W.W and King, T.S. and Xiong, X. and Nalli, N.R. and Maddy, and E.S. and Divakarla, M. and Goldberg, M., 2012, The NOAA Unique CrIS/ATMS processing System (NUCAPS): first light results, Proceedings of the International TOVS Working Group Meeting, Toulouse, France.

Gambacorta, A. and Barnet, C.D. and Wolf, W.W and King, T.S. and Xiong, X. and Nalli, N.R. and Maddy, E.S. and Divakarla, M. and Goldberg, M., 2012, The NOAA Unique CrIS/ATMS processing System (NUCAPS): 1 year in orbit, Proceedings of the Eumetsat meeting, Sopot, Poland.

Gambacorta, A. and Barnet, C.D., Methodology and information content of the NOAA NESDIS operational channel selection for the Cross-Track Infrared Sounder (CrIS), IEEE transactions on Geoscience and Remote Sensing, 2012, doi = 10.1109/TGRS.2012.2220369.

Susskind, Barnet, and Blaisdell, (2003), Retrieval of atmospheric and surface parameters from AIRS/AMSU/HSB data in the presence of clouds, *IEEE Trans. Geosci. Remote Sensing*, *41*(2), 390–409.

# Chapter 2

# Satellite instrument Description

## 2.1 The Advanced Technology Microwave Sounder (ATMS)

The Advanced Technology Microwave Sounder (ATMS) is a cross-track scanner which combines all the channels of the preceding AMSU-A1, AMSU-A2, and AMSU-B sensors into a single package consisting of 22 channels in spectral bands from 23 GHz through 183 GHz. Channel 3 - 15 fall within the 50-60 GHz portion of the oxygen band to temperature and precipitation information. In addition, ATMS contains three window-channels at 23.8, 31.4, and 89 GHz to provide total precipitable water, cloud liquid water content, and precipitation measurements, respectively. These channels can also be used to provide information on sea-ice concentration and snow cover. ATMS also has one window-channel at 166.31 GHz to obtain high-resolution measurements of precipitation, snow cover, and sea-ice. Three additional channels in the 183 GHz water vapor line are used to retrieve atmospheric humidity profiles. The 3-dB beam diameter of an ATMS FOV is 1.1, corresponding to about 16 km at nadir. This beam is co-located with the CrIS field-of-view (FOV).

The scanning geometry and footprint sizes of ATMS are somewhat different for every channel. Channels 1 and 2 have a beam width of 5.2 degrees, which corresponds to a footprint size of 74.8 km at nadir. Channels 3-16 have a beam width of 2.2 degrees, which corresponds to a footprint size of 31.6 km at nadir. Channels 17-22 have a beam size of 1.1 degrees, which corresponds to a footprint size of 15.8 km. The footprints are shown in Figure 8. Because the ATMS scans at a rate of 8/3 seconds per scan, the scan pattern overlaps, but does not match exactly, the scan pattern of CrIS. The EDR algorithm assumes that the ATMS data will be re-sampled to match the CrIS FOR configuration prior to ingestion by the CrIS software.

## 2.2 The Cross-Track Infrared Sounder (CrIS)

CrIS is one of the most advanced instruments onboard the NPP platform, measuring infrared radiation emitted from the surface of the Earth. CrIS is a Fourier transform spectrometer with a total of 1305 infrared sounding channels covering the longwave (655-1095 $cm^{-}1$), midwave (1210-1750 $cm^{-}1$), and shortwave (2155-2550 $cm^{-}1$) spectral regions. The nominal spectral resolution is defined as 1/2L, where L is the maximum optical path difference of the interferometer. Each band has different spectral resolutions. The frequency range adopted in the current design of the CrIS instrument is listed in Table 1. Figure 2 shows an example of simulated clear-sky radiances in the CrIS bands. The radiances are expressed in brightness temperature units. The emission in the spectral region 650-800 $cm^{-}1$ is mainly from atmospheric CO2 and is used for atmospheric temperature sounding. The atmospheric window region in LWIR extends from 800 to 950 $cm^{-}1$

and provides sounding channels for the surface properties and the lower troposphere temperatures. The main emission band of O3 is centered around 1050 cm-1. The main emission in MWIR is due to atmospheric moisture, although there are some contributions from methane and nitrous oxide near 1250 $cm^{-}1$. MWIR contains most of the CrIS atmospheric moisture sounding channels. The main feature in SWIR is the emission from the 4.18 band of CO2 that is also used for atmospheric temperature sounding.

## 2.3 References

CrIS (2013), The cross-track infrared sounder, http://www.ipo.noaa.gov.
ATMS (2013), The Advanced technology Microwave Sounder, http://www.ipo.noaa.gov.
JPSS (2013), The joint polar satellite system, www.jpss.noaa.gov/.

# Chapter 3

# Algorithm Description

NUCAPS consists of six modules as described below: 1) A preliminary input quality control, look up tables and ancillary product acquisition 2) A microwave retrieval module which derives cloud liquid water flags and microwave surface emissivity uncertainty (Rosenkranz, 2000); 3) A fast eigenvector regression retrieval for temperature and moisture that is trained against ECMWF analysis and CrIS all sky radiances (Goldberg et al., 2003;). 4) A cloud clearing module that combines a set of microwave and IR channels (along with, in the future, visible observations provided by the onboard VIIRS instrument) to produce cloud-cleared IR radiances (Chahine, 1974). 5) A second fast eigenvector regression retrieval for temperature and moisture that is trained against ECMWF analysis and CrIS cloud cleared radiances (Goldberg et al., 2003;). 6) The final infrared physical retrieval, which employs the previous regression retrieval as a first guess (Susskind, Barnet, Blaisdell (2003) ).

Figure 3.1 describes the complete flow diagram of the algorithm software architecture. The full description of the attributes of all input data used by the algorithm, including primary sensor data, ancillary data, forward models and look-up tables is provided in the next chapter.

## 3.1 References


Goldberg, M., Y. Qu, L. McMillin, W. Wolf, L. Zhou, and M. Divakarla (2003), AIRS 179 Near-Real-Time products and algorithms in support of operational numerical weather 180 prediction, IEEE, 41, 379.

Chahine, M. T., Remote sounding of cloudy atmospheres in a single cloud layer, J. Atmos. Sci., 1974, vol. 31, pages 233 - 243.

Rosenkranz, P. (2000), Retrieval of temperature and moisture pro
les from AMSU-A and 198 AMSU-B measurements, IEEE, 39, 2429.

Susskind, Barnet, and Blaisdell, (2003), Retrieval of atmospheric and surface parameters from AIRS/AMSU/HSB data in the presence of clouds, *IEEE Trans. Geosci. Remote Sensing*, *41*(2), 390–409.

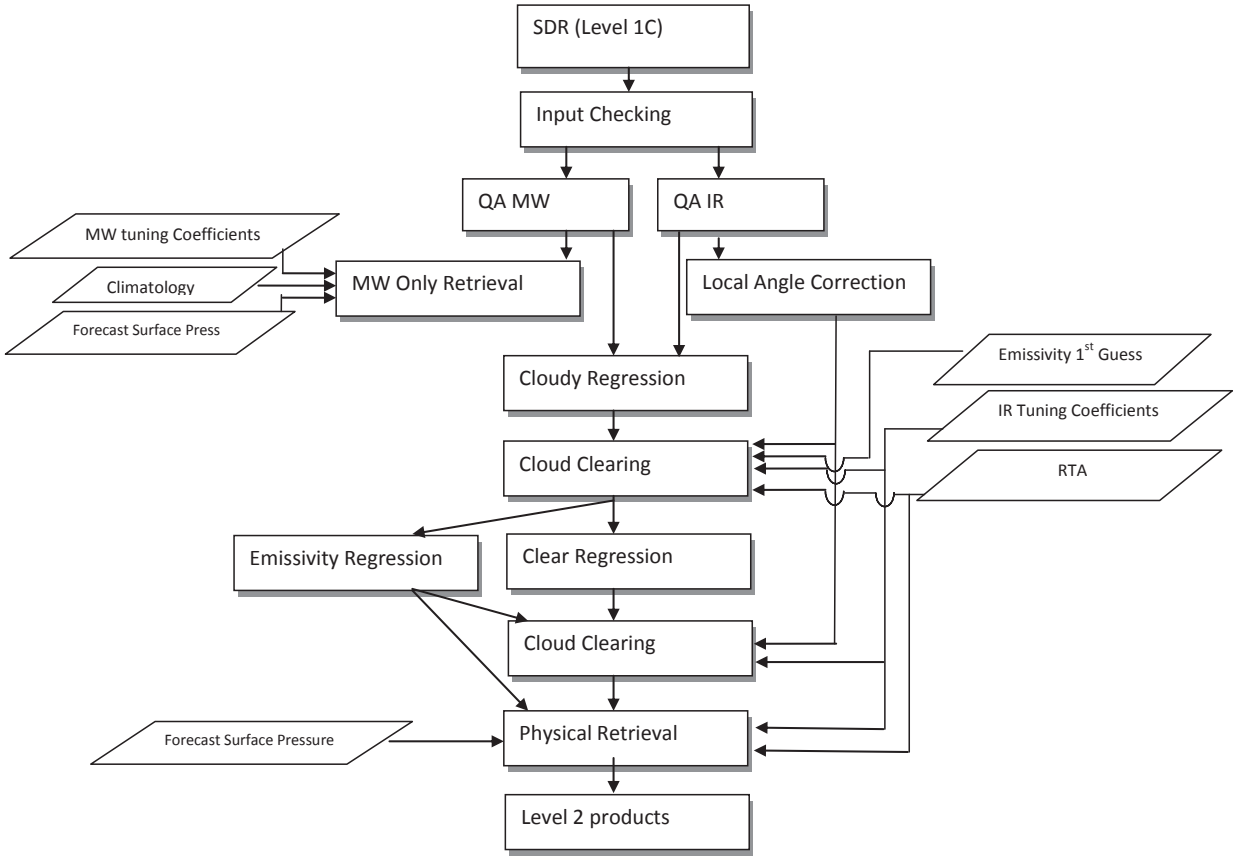


Figure 3.1: NUCAPS Level 2 processing flow chart

# Chapter 4

# Algorithm Inputs

## 4.1 Background Climatology Look Up Tables

A background climatology is available to all retrievals on a 2.5 degree Mercator grid using 100 levels. Climatological profiles of temperature, water vapor are used extensively in the MW-Only retrieval step. Climatological profiles of trace gases are also used as first guess in the physical retrieval step. The climatology is based on two sources: (1) the National Center for Environmental Prediction (NCEP) temperature and water vapor monthly means derived from the 20 year (1979-1998) reanalysis on a 2.5 degree Mercator latitude/longitude grid; and (2) the Upper Atmosphere Research Satellite (UARS) temperature, water vapor and ozone profiles. The climatological temperature profile is obtained from the NCEP source from the surface up to 100mb, tri-linearly interpolated by month, latitude and longitude and then log-pressure interpolated onto the 100 levels. A $P^4$ extrapolation is used for altitudes above 100mb. The climatological water vapor profile is derived from the NCEP source from the surface up to 300mb, tri-linearly interpolated by month, latitude and longitude and then log-pressure interpolated onto the 100 levels. Above 300mb the information comes from the UARS source, linearly interpolated between two latitude zones. The ozone climatology is derived from the UARS source, linearly interpolated between two latitude zones. No time interpolation is computed.

The CO a priori is a 12 month set of two single CO profiles, for the northern and southern hemisphere respectively, computed from the Measurements of Pollution In The Troposphere (MOPITT) version 4 CO monthly averages. These profiles are temporally and spatially interpolated during the retrieval.

A first-guess $CH_4$ profile [Xiong, X. et al., 2008] as a function of latitude and altitude was generated to capture its strong latitudinal and vertical gradients. This $CH_4$ first-guess profile was generated by using a nonlinear polynomial fitting to different data, including the in situ aircraft observation data from six sites (the first six sites in Table 1) of the NOAA Earth System Research Laboratory, Global Monitoring Division (ESRL/GMD), some ground-based flask network data[GLOBALVIEW-CH4, 2005], Matsueda aircraft observation data [Matsueda and Inoue, 1996] and HALOE satellite observation data [Park et al., 1996](http://haloedata.larc.nasa.gov/download/index.php). In the fitting only the mean profiles as a representative of its climatology for each location and altitude were used. For example, for each NOAA/ESRL/GMD site only the mean of all profiles observed in the past 3 years from 2003 to early 2006 was used. Matsueda aircraft data from GLOBALVIEW-CH4[2005] and HALOE data were interpolated to several latitudinal grids first, and then the mean profiles corresponding to different latitude and altitude were used. Monthly average of model simulated data using the TM3[Houweling et al., 2006] was used to extrapolate

the in situ aircraft data to higher altitudes. Over the southern hemisphere oceans where in situ measurements are not available, yearly zonal mean profiles in several latitude grids from the TM3 model are also used.

The $N_2O$ climatology is given as a smoothed function of latitude and pressure. The generation of N2O first-guess profile was from model data only. The model simulations are made by the Center for Climate System Research/National Institute for Environmental Studies/Frontier Research Center for Global Change (CCSR/NIES/FRCGC) using an Atmospheric General Circulation Model (AGCM)-based chemistry transport model.

## 4.2 Local Angle Adjustment Coefficients

CrIS makes a 90-degree measurement, cross-track between -49 and +49 degrees. The data analysis, however, uses the data in 3x3 clusters with 30 scan angles between -49 and +49 degrees. A primary assumption of cloud clearing is that within a 3x3 array of 9 CrIS FOVs the differences are solely attributed to differences in clouds. Local angle adjustment removes one potentially confounding source of intra-FOV variation: differences in observing geometry. In each 3x3 cluster there are 3 observations at each of 3 different scan angles. This step makes small adjustments to the spectra for the 3 highest- angle and 3 lowest-angle FOVs so all FOVs resemble those which would be observed at the central angle. No adjustment is applied to the central FOVs. In the AIRS retrieval algorithm, the actual adjustment is calculated using a PCs approach. Given the rotating scanning geometry of the CrIS instrument a more complex solution needs to be taken and is the subject of a work in progress. Unpublished studies have shown though that the local angle correction does not have significant impact on the retrieval performance and can be neglected with no noticeably detrimental effects.

## 4.3 Forecast Surface Pressure

The AVN forecast surface pressure, PSurf, are used by the L2 retrieval. The surface pressure is available on a one-degree grid. The surface pressure is calculated from the 3-,6-, and 9-hour forecasts from the same model run, interpolated in space and time to match observed location.

## 4.4 Surface Emissivity First Guess

The Mazuda emissivity model is employed over ocean. A regression formulation is employed instead over land.

## 4.5 Microwave and Infrared Tuning Coefficients

A large category of inversion algorithms relies on least square residual minimizations of observed brightness temperature and brightness temperatures computed from first guess profiles. In these algorithms, generally referred to as "physical", radiative transfer calculations are performed by mean of theoretical forward models and there is a need for identifying and removing those components of the residuals arising from modeling, measurement errors and instrumental noise. This process, commonly referred to as *brightness temperature tuning*, is fundamental to achieve retrieval performance

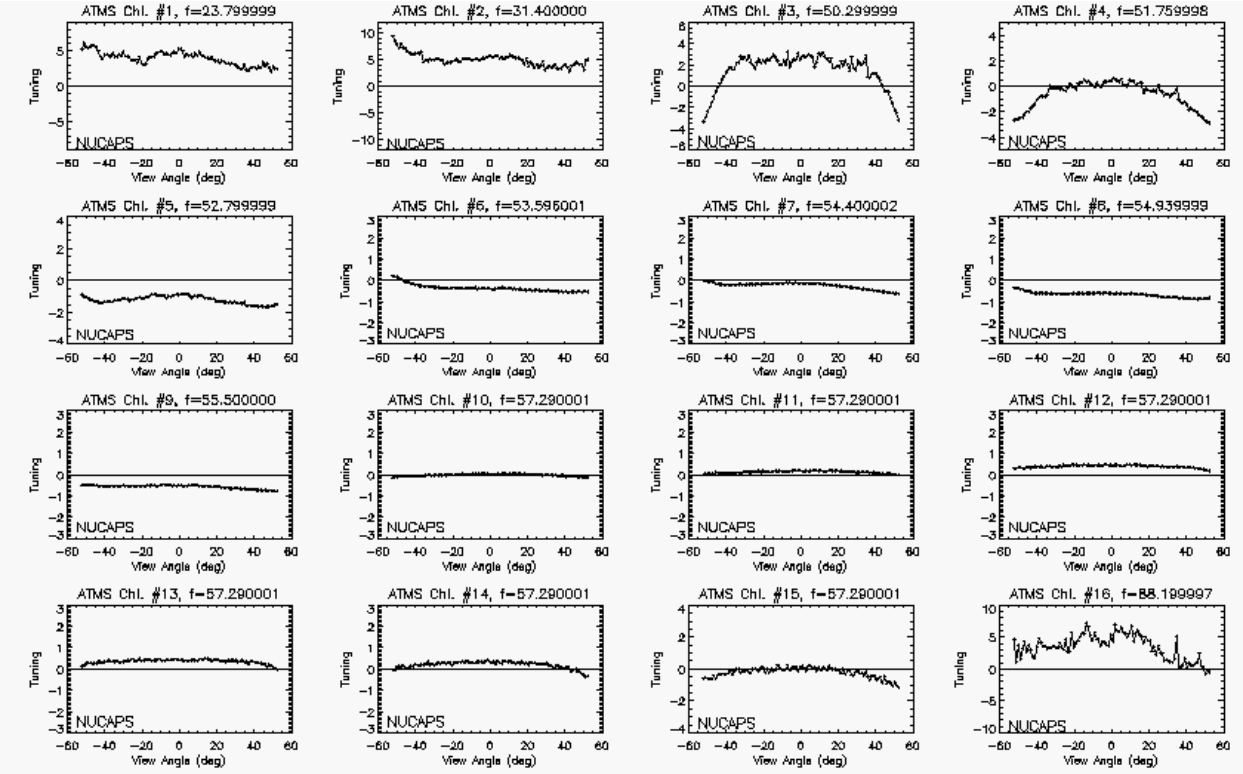


Figure 4.1: ATMS tuning correction for channels 1 - 16, as a function of view angle.

accuracy, in that it removes artificial systematic biases that could be otherwise ascribed to a physical atmospheric source and, in long term applications, erroneously confused with climate signals. Specifically, forward model errors may include both systematic and profile-dependent components ros:2003. Systematic errors may include radiometric calibration, thermal emission from parts of the space-craft, and, for microwave sensors, antenna side lobe effects mo:1999. These systematic sources of error can contribute to a large part of the overall bias and in the microwave case show dependence on view angle and slightly on the temperature profile.

Using forward model computations, a tuning coefficient set is computed as an average bias difference of a global sample of observed minus computations (OBS - CALC), for each channel and in the microwave case, scan angle position (for ATMS there are 96 consecutive acquisitions per scan line). In reality, we limit the collection of OBS-CALC samples over a restricted area of the globe, which only includes open ocean, clear sky, day-time and non-high latitude areas, where the collection of correlative "truth" profiles is relatively more reliable. Specifically, the sub-field of view variability is usually higher over land, coastal and broken cloud scenarios, as opposed to the more uniform open ocean and clear sky conditions, hence our choice to restrict the tuning training sample to the more uniform ocean-only and clear-sky areas of the globe. The selection of non precipitating cases is also dictated by the fact that microwave forward modes, in general, do not handle precipitation. Besides sampling errors, measurement errors can also represent a significant source of uncertainty in the truth. This is the case for high latitude and daytime atmospheric measurements, whether performed by mean of in situ acquisitions (radiosondes) or independent retrievals and re-analyses. Specifically, truth profiles collected over high latitude regimes by mean of Vaisala radiosondes tend to suffer from temperature dependent errors (the colder the temperature, the larger the error)

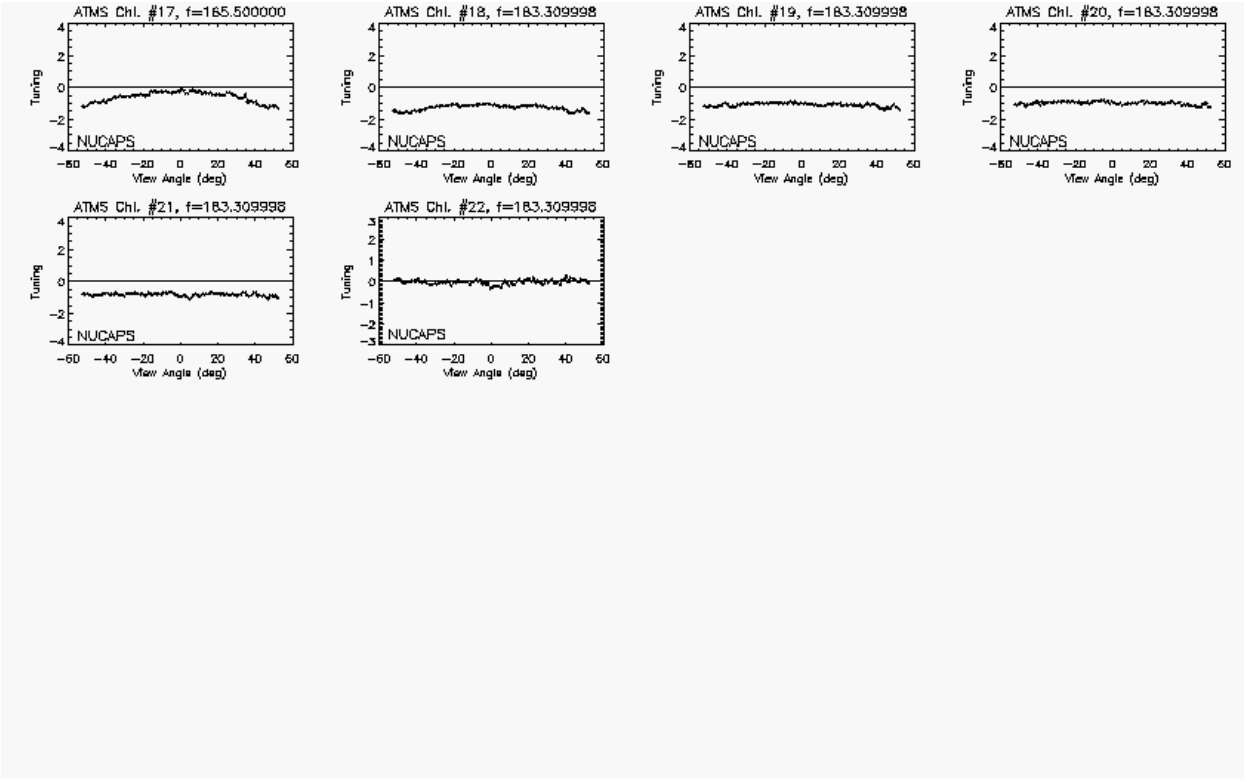


Figure 4.2: ATMS tuning correction for channels 17 - 22, as a function of view angle.

in the form of a significant dry bias in the relative humidity measurements wang:02. Furthermore, radiosonde daytime measurements suffer from so called solar arm heating (SAH) errors, originated by radiational heating of the temperature and humidity sensor prior to launch, and resulting in a higher temperature and drier humidity measurements. It has been observed that a temperature difference of 1 degree Celsius between the ambient and the sensor arm corresponds to 4% SAH error in relative humidity wang:02. Alternative measurements, such as independent infrared retrievals or re-analyses, suffer from high latitude law signal to noise temperature gradients, besides being subject to large uncertainties in snow/ice infrared emissivity, daytime non local thermodynamic equilibrium and solar reflectivity parameterization. These measurement uncertainties in daytime and cold conditions dictate the necessity to further limit our sampling selection to nighttime and tropical to mid latitude regions only. More details on the microwave and infrared tuning methodology employed in the NUCAPS algorithm can be found in [Gambacorta et al., 2013a] and Gambacorta et al., 2013b]. The ATMS tuning file is shown in Figure-4.5, Figure-4.5 as a function of view angle. Figure-**??** shows the CrIS tuning file. A comparison with respect to the AIRS and IASI operational tuning file is also shown. Both instruments tuning were performed foillowing the same methodology as in NUCAPS.

## 4.6 The Radiative Transfer Model

The physical retrieval methodology utilized by the NUCAPS depends on the ability to accurately and rapidly calculate the outgoing radiance based on the state of the surface and the atmosphere.

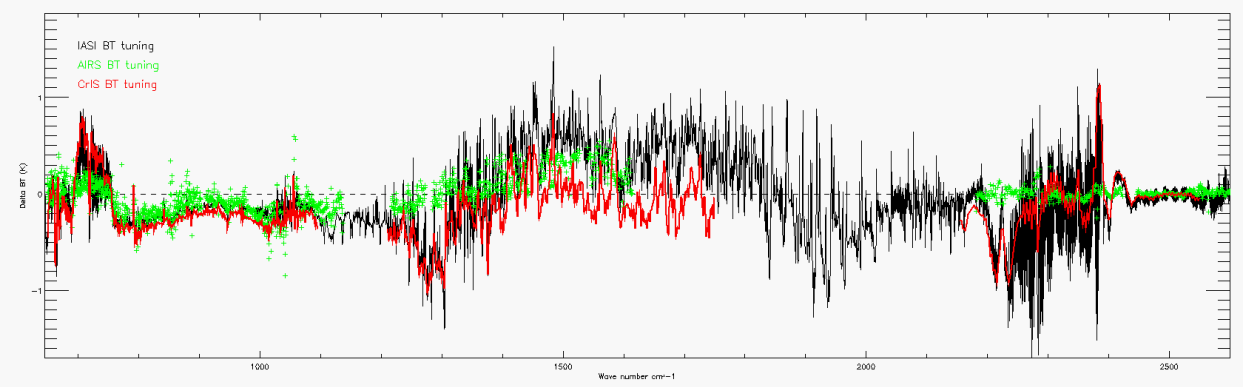


Figure 4.3: IR bias tuning comparison: CrIS (green), IASI (black) and AIRS (red).

The radiative transfer model consists of a parameterized algorithm to compute atmospheric transmittance, a model for surface brightness temperature, and a model for the reflected downwelling atmospheric emission. The following sections discuss the microwave and infrared radiative transfer models and error estimates.

### 4.6.1 Radiative Transfer Model of the Atmosphere in the Microwave

At the frequencies measured by ATMS, the most important absorbing gases in the atmosphere are oxygen and water vapor. The oxygen molecule has only a magnetic dipole moment, and its lines are intrinsically much weaker than those which result from the electric dipole of water vapor; however, the much greater abundance of oxygen in the atmosphere more than compensates for this difference. When clouds are present, liquid water also plays a role in radiative transfer. However, fair-weather cirrus composed of ice particles small compared to the wavelength are generally transparent to the ATMS frequencies.

#### Oxygen

O2 spin-rotation transitions comprise approximately 30 lines between 50 and 70 GHz and an isolated line at 118.75 GHz (which is not observed by AMSU or HSB). Several groups have measured the pressure-broadened widths of the lines in the 50-70 GHz band. The line parameters used for the forward model are from the Millimeter-wave Propagation Model (MPM92) (Liebe, et al., 1992). The characteristic of oxygen's microwave spectrum that introduces difficulty for construction of models is the significant degree of line mixing. In MPM92, line mixing was treated by a first-order expansion in pressure. The coefficients for this expansion were determined by a constrained linear fit to laboratory measurements made on an O2 - N2 mixture over the frequency range of 49-67 GHz and the temperature range 279-327 K, with a noise level of approximately 0.06 dB/km. Within that range, the model represents the measurements to 0.2 dB/km (see for example, Figure 4.1.1). It is possible that extrapolation to colder temperatures introduces larger errors. Measurements from the NASA ER-2 at 52-56 GHz (Schwartz, 1997) seem to be in agreement with the model, however.

#### Water Vapor

Water has a weak rotational line at 22.23 GHz that is semi-transparent at normal atmospheric humidity, and a much stronger, opaque line at 183.31 GHz. Intensities of these lines have been

calculated and tabulated by Poynter and Pickett (1996 version of JPL line catalog) and Rothman et al., (1998) (HITRAN), among others. The HITRAN intensities are used here. For the 22-GHz line, the JPL intensity is higher than the HITRAN value by 0.3%. There is a measurement by Liebe et al., (1969) (estimated error 0.3%) which is 3.5% lower than the HITRAN value. At 183 GHz, the JPL line intensity is 0.1% higher than HITRAN. Widths have been measured by Liebe et al., (1969) and Liebe and Dillon (1969) at 22 GHz with estimated uncertainty of 1% for both self and foreign-gas broadening; and by Bauer et al., (1989) and Tretyakov et al. (2003) at 183GHz, with uncertainties of 0.5% for self-broadening and 1.0% for foreign-gas broadening, respectively. However, Gamache et al. (1994) concluded from a survey of measurements of many H2O lines that, in general, measured line widths should be considered to have uncertainties of 10-15%. The line at 183 GHz is a case in which published measurements of width differ significantly, but the value of Tretyakov et al. (2003), which is used here, lies near the centroid of the measurements. At frequencies away from these two lines, microwave absorption by water vapor is predominantly from the continuum, which is attributed to the low-frequency wing of the intense infrared and submillimeter rotational band lines. In the microwave part of the spectrum, the foreign-broadened component of the continuum is stronger than the self- broadened component, for atmospheric mixing ratios. Measurements of continuum absorption as a function of temperature have been made at various frequencies by Liebe and Layton (1987), Godon, et al. (1992) and Bauer et al. (1993, 1995). There are also numerous measurements at single temperatures and frequencies in the laboratory, and in the atmosphere where temperature and mixing ratio are variable. The measurements do not present an entirely consistent picture. Rosenkranz (1998) proposed that the most satisfactory overall agreement with laboratory and atmospheric measurements of the water continuum was obtained with a combination of the foreign-broadened component from MPM87 (Liebe and Layton, 1987) with the self-broadened component from MPM93 (Liebe et al., 1993). The combined model is used here.

**Liquid Water**

It is useful to distinguish between precipitating and non-precipitating clouds with respect to their interactions with microwaves. Over the range of wavelengths measured by ATMS, non-precipitating droplets (with diameters of 50 m or less) can be treated using the Rayleigh small-droplet approximation. In this regime, absorption is proportional to the liquid water content of the air, and scattering can be neglected. The model for the dielectric constant limits the accuracy of these calculations. The double- Debye model of Liebe et al., (1991) is used here; for temperatures ¿ 0 C, it has an estimated maximum prediction error of 3% between 5 and 100 GHz, and 10% up to 1THz. Although some measurements of static dielectric constant at temperatures as low as -20 C were used by Liebe et al. to develop their model, its use for supercooled water must be considered to be an extrapolation, with uncertain accuracy. (The model is implemented using the alternate eq. 2b in Liebe et al.) Precipitation, on the other hand, requires Mie theory to calculate both absorption and scattering. The latter is generally not negligible, and is the dominant term at some wavelengths. In the case of convective storms, scattering from ice at high altitudes is often the most important process. The rapid transmittance algorithm uses only the small- droplet approximation for cloud liquid water, and scattering is not included. For this reason, retrieved profiles with more than 0.5 kg/m2 cloud liquid water are rejected, as probably rain-contaminated.

**The microwave rapid transmittance algorithm**

The modeled brightness temperature $T_b$ received by a space born microwave radiometer over a smooth surface of emissivity $\varepsilon$ can be expressed as:

$$
\begin{aligned}
&\mathrm{T}_B = \omega^{-1} \textstyle\int_0^{\infty} \mathrm{d}\nu H(\nu) \\
&\mathrm{x}\, \{\textstyle\int_0^{P_s} \mathrm{d}P[-\mathrm{d}\tau_\nu(0,P)/\mathrm{d}P]T(P) \\
&+ \varepsilon\tau_\nu(0,P_s)T_s \\
&+ \text{(1-}\varepsilon)\tau_\nu(0,P_s) \textstyle\int_0^{P_s} \mathrm{d}P[-\mathrm{d}\tau_\nu(P_s,P)/\mathrm{d}P]T(P) \\
&+ (1-\varepsilon)\tau_\nu(0,P_s)^2 T_{cb} \\
&(4.1)
\end{aligned}
$$

where $H(\nu)$ represents the passband of the radiometer channel of frequency $\nu$, $\omega$ is the spectral total width of the passband, $\tau_\nu(P_1, P_2)$ is the transmittance at frequency $\nu$ between the pressure levels $P_1$ and $P_2$, $T(P)$ is the atmospheric temperature at level P, $T_s$ and $P_s$ are surface temperature and pressure, and $T_{bc}$ is the cosmic background brightness temperature.

Near real time operations require rapid data processing which precludes the use of a line-by-line transmittance model. The rapid algorithm employed in this study and operationally used at NOAA/NESDIS to process the ATMS, AMSU-A and MHS instruments is the microwave rapid transmittance algorithm developed by ros:1995 and ros:2003 and later validated by ros:2006. In this rapid algorithm, the integration over frequency in (1) is replaced by a passband-averaged transmittance $< \tau(0,P) >$. The average transmittance between two adjacent pressure levels, $P_1$ and $P_2$, is computed as:

$$< \tau(P_1, P_2) >= exp{-}[\alpha + \beta V + \gamma L] \tag{4.2}$$

where $V$ is the vertical column density integral of water vapor between the two levels and $L$ is the cloud liquid vertical column density integral; $\alpha$ represents the opacity of fixed gases (oxygen and nitrogen) in the layer. The coefficient $\alpha$, $\beta$ and $\gamma$ are computed for each layer and channel, given the inputs of $V$, temperature, pressure and secant of observation angle. Window channels, water vapor channels and oxygen-band channels are considered separately. Each band employs tabular or polynomial approximations to line-wing or near-line absorption from water vapor or oxygen. Absorption by cloud liquid water and ozone is also included. For a complete description of the derivation of $\alpha$, $\gamma$ and $\beta$ the reader can refer to ros:1995 and ros:2003.

For oxygen-band channels sounding the atmosphere above 40km, Zeeman splitting produced by the terrestrial magnetific field becomes important. For those channels, transmittance is parametrized as a function of the magnetic field strength $B$ and the angle $\Theta_B$ between the direction of propagation and the magnetic field. References ros:1995 and ros:2003 also provide an in depth description of the transmittance parametrization in presence of Zeeman splitting.

Transmittances are computed for 101 layers between 0.5 and 1100 hPa, chosen with approximately even spacing on $P^{2/7}$. The total transmittance is derived as the product of transmittances (2) for each of those layers. This total transmittance, $< \tau(0, P_s) >$, is then used in a simplified form of the radiative transfer equation expressed by:

$$\mathrm{T}_B = T_B^{direct} + < \tau(0, P_s) > [T_B^{surface} + T_B^{sky}(1 - T_B^{surface}/T_s] \tag{4.3}$$

where $T_B^{direct}$ is the simplified version of the first term in Equation 2.2.1 representing the direct path from surface footprint to satellite:

$$T_B^{direct} = \int_{P_s}^{0} T(P)\mathrm{d} < \tau(0, P) > \tag{4.4}$$

$T_B^{surface}$ is the surface brightness temperature given by the product between the surface emissivity and the skin temperature $T_s$, and $T_B^{sky}$ is the downward propagating sky brightness temperature (including the cosmic background contribution, $T_{cb}$) as it would be observed from the surface and represented by:

$$\mathrm{T}_B^{sky} = \textstyle\int_0^{P_s} T(P)\mathrm{d} < \tau(P, P_s) > + T_{cb} < \tau(0, P_s) > \tag{4.5}$$

Planck's equation for radiant intensity is a nonlinear function of temperature. For microwave frequencies, however, the physical temperatures encountered in the earth's atmosphere lie at the high-temperature asymptote of this function. Hence, as discussed by Janssen (1993), brightness temperature can be used as a surrogate for radiance in the equation of radiative transfer with an accuracy of a few hundredths of a Kelvin, provided that the cosmic background is assigned an effective brightness temperature at frequency of

$$T_{cb} = \frac{h\nu}{2K} x \frac{exp[h\nu/KT_c] + 1}{exp[h\nu/KT_c] - 1} \tag{4.6}$$

instead of its actual temperature $T_c = 2.73K$, in order to linearize the Planck's function.

It has been shown that this rapid transmittance model requires thirty times less computation than a line-by-line algorithm with an accuracy comparable to or better than the channel sensitivities ros:1995.

**Surface emissivity model for open ocean**

The ocean surface emissivity for frequency $\nu$, $\varepsilon(\nu)$ for a flat surface at local thermodynamical equilibrium is defined by:

$$\varepsilon(\nu) = 1 - R_p \tag{4.7}$$

where $p$ is the polarization of the signal, horizontal (H) or vertical (V), and $R_p$ is the square of the Fresnel reflection coefficient for polarization $p$, defined as:

$$R_H = \left| \frac{\cos\theta_{za} - \sqrt{e - \sin^2\theta_{za}}}{\cos\theta_{za} + \sqrt{e - \sin^2\theta_{za}}} \right|^2 \tag{4.8}$$

$$R_V = \left| \frac{e\cos\theta_{za} - \sqrt{e - \sin^2\theta_{za}}}{e\cos\theta_{za} + \sqrt{e - \sin^2\theta_{za}}} \right|^2 \tag{4.9}$$

In these equations, $e$ is the dielectric permittivity of saline water. We employ a revised Debye model, the *Double Debye model*, developed and validated by ell:03 which is obtained as a linear fit of experimental data for synthetic seawater and at seven different temperatures representative of the world's oceans, in the frequency range 3 -105 GHz. An extrapolation is being used for higher frequencies.

The ATMS radiometer front-end scanning optics are of a rotating reflector and fixed feedhorn type design. With this configuration, the polarization vector rotates with the cross-track scanning reflector. As a result, at any beam position making an angle $\theta$ with respect to nadir, the received polarization is a linear combination of the vertical and horizontal polarization vectors.

ATMS channels 1 (23.8 GHz), 2 (31.4GHz) and 16 (88.2GHz) are vertically polarized (perpendicular to the ground track) at nadir and generally *quasi-vertically* polarized at any other viewing angle $\theta_v a$. All other ATMS channels are *quasi-horizontally* polarized and fully horizontally polarized at nadir (polarization vector parallel to the ground track). The surface emissivity for quasi-vertical and quasi-horizontal polarized channels can be expressed rispectively as:

$$\begin{aligned} \varepsilon_V(\nu) &= (1 - R_V)\cos^2\theta_{va} \\ &+ (1 - R_H)\sin^2\theta_{va} \end{aligned} \tag{4.10}$$

$$\begin{aligned} \varepsilon_H(\nu) &= (1 - R_V)\sin^2\theta_{va} \\ &+ (1 - R_H)\cos^2\theta_{va} \end{aligned} \tag{4.11}$$

### 4.6.2 Radiative Transfer Model of the Atmosphere in the Infrared

The total monochromatic radiance, $R(\nu, \theta, X)$, at frequency $\nu$, zenith angle $\theta$, for an atmosphere with geophysical state, $X$, emerging from the top of the atmosphere can be broken into the following components

$$\begin{aligned} R(\nu,\theta,X) &= R_s(\nu,\theta,X) && \text{Surface} \\ &+ R_a(\nu,\theta,X) && \text{Atmospheric Column} \\ &+ R_d(\nu,\theta,\theta',X) && \text{Down} - \text{welling} \\ &+ R_\odot(\nu,\theta,\theta_\odot,X) && \text{Reflected Solar} \end{aligned} \tag{4.12}$$

Specifically, $R_s(\nu, \theta, X)$ is the contribution due to the surface radiance, averaged over the footprint, attenuated by the atmospheric column of the observation. $R_a(\nu, \theta, X) = \sum_{L=1}^{N_L} R_L(\nu, \theta)$ is the sum of all the contributions $R_L(\nu, \theta)$ from all the layers within the IFOV. $R_d(\nu, \theta, X)$ is the contribution due to the down-welling radiation from the entire atmospheric volume reflected by the surface and transmitted through the observed atmospheric column. $R_\odot(\nu, \theta, \theta_\odot, \rho_\odot, X)$ accounts for the transmission of sunlight from the TOA through the atmosphere at angle $\theta_\odot$, reflected from the surface, and transmitted out of the atmosphere at angle $\theta$ to the spacecraft.

Since the Planck function is linear in the microwave region (see Eqn. **??**) then Eqn. 4.12 can be written in terms of brightness temperatures as well

$$\Theta(\nu,\theta) = \Theta_s(\nu,\theta) + \Theta_a(\nu,\theta) + \Theta_d(\nu,\theta) + \Theta_b(\nu,\theta) \tag{4.13}$$

#### Radiance contribution from the surface

The radiance emerging at the top of the atmosphere is given by the contributions from the surface and attenuated by the atmospheric transmittance. We will begin by considering only the radiation upwelling from the surface emission.

The component of out-going radiance from the surface is given by a black-body radiance at the surface skin temperature, $T_s$, multiplied by the surface emissivity, $\epsilon_\nu$.

The surface radiance must pass through the entire atmosphere and is, therefore, multiplied by the column transmittance from the surface to the top of the atmosphere. The monochromatic out-going surface radiance is given by

$$R_s(\nu,\theta) = \epsilon_\nu \cdot B_\nu(T_s) \cdot \tau_\nu^\uparrow(P_s,\theta) \tag{4.14}$$

where we employ a short hand notation for the surface to space transmittance

$$\tau_\nu^\uparrow(P_s,\theta) \equiv \tau_\nu(P_s \to 0,\theta) \tag{4.15}$$

The monochromatic brightness temperature equation for the surface contribution is given by

$$\Theta_s(\nu,\theta) = \epsilon_\nu \cdot T_s \cdot \tau_\nu^\uparrow(P_s,\theta) \tag{4.16}$$

and, as discussed in Section **??**, the channel averaged equation for the surface contribution is given by

$$\Theta_s(n,\theta) = \epsilon_n \cdot T_s \cdot \tau_n^{\uparrow}(P_s,\theta) \tag{4.17}$$

The surface component, $R_s$, is given as

$$R_s(\nu,\theta) = \epsilon_\nu \cdot B_\nu(T_s) \cdot \tau_\nu^{\uparrow}(P_s,X,\theta) \tag{4.18}$$

- $\epsilon_\nu$ is the spectral surface emissivity, and
- $B_\nu(T)$ is the Planck function, $B_\nu(T)$, which is the specific intensity (brightness) of a black-body emitter, usually written as

$$B_\nu(T) = \frac{\alpha_1 \cdot \nu^3}{\exp(\frac{\alpha_2 \cdot \nu}{T}) - 1} \tag{4.19}$$

- $\tau_\nu^{\uparrow}(P_s,X,\theta)$ is the transmittance of the atmosphere from the surface, at pressure $P_s$ to the instrument.

**Radiance contribution from the atmosphere**

For a thin layer of the atmosphere, defined between pressure layers at $p(L)$ and $p(L-1)$, the monochromatic radiance contribution at the top of the atmosphere from the atmospheric layer is analogous to the surface radiance and is given by

$$\begin{aligned}
R_L(\nu) &= \epsilon_{eff}(L) \cdot B_\nu(\overline{T(L)}) \cdot \tau_\nu(p(L-1) \to 0,\theta) && (4.20)\\
&= [1 - \tau_\nu(p(L) \to p(L-1),\theta)] \cdot B_\nu(\overline{T(L)}) \cdot \tau_\nu(p(L-1) \to 0,\theta) && (4.21)\\
&= B_\nu(\overline{T(L)}) \cdot [\tau_\nu(p(L-1) \to 0,\theta) - \tau_\nu(p(L) \to 0,\theta)] && (4.22)\\
&= B_\nu(\overline{T(L)}) \cdot \Delta\tau_\nu^{\uparrow}(L,\theta) && (4.23)
\end{aligned}$$

$$\Delta\tau_\nu^{\uparrow}(L,\theta) \equiv \tau_\nu(p(L-1) \to 0,\theta) - \tau_\nu(p(L) \to 0,\theta) \tag{4.24}$$

The term $(1 - \tau_\nu(p(L) \to p(L-1),\theta)$ in Eqn. 4.20 can be thought of as a effective emissivity of the layer. When the layer is opaque the gas emits as a black-body; however, when completely transmissive we do not see any contribution from that layer.

The proper derivation begins with the equation of radiation transfer (*e.g.*, see Chandrasekar, 1960 or Mihalis, 1978),

$$\begin{aligned}
\frac{\partial R_\nu}{\partial \phi_\nu} &= \frac{1}{\mu}(S_\nu - R_\nu) && (4.25)\\
\partial R_\nu &= \frac{1}{\mu}(S_\nu - R_\nu) \cdot \partial\phi_\nu && (4.26)
\end{aligned}$$

For an atmosphere in *local* thermal equilibrium with no scattering the radiation source function, $S_\nu = B_\nu(T)$, can be described by the Planck function. The radiative transfer equation (*e.g.*, see Mihalis 1978 pg. 38) is a function of the optical depth, $\phi_\nu$, and the cosine of the zenith angle, $\mu$,

$$\frac{\partial R_\nu}{\partial \phi_\nu} = \frac{1}{\mu}\left(B_\nu - R_\nu\right) \tag{4.27}$$

We can find an integration factor to obtain

$$\frac{\partial R_\nu}{\partial \phi_\nu} \cdot e^{-\phi_\nu/\mu} = \frac{B_\nu(T)}{\mu} \cdot e^{-\phi_\nu/\mu} - \frac{R_\nu}{\mu} \cdot e^{-\phi_\nu/\mu} \tag{4.28}$$

$$\frac{\partial \left(R_\nu \cdot e^{-\phi_\nu/\mu}\right)}{\partial \phi_\nu} = \frac{B_\nu(T)}{\mu} \cdot e^{-\phi_\nu/\mu} \tag{4.29}$$

And then we can integrate the equation directly. The integration constant is the boundary condition, which is the surface term we discussed earlier.

$$R_\nu = \int_\infty^0 B_\nu(T(z)) \cdot e^{-\phi_\nu/\mu} d\phi/\mu \tag{4.30}$$

We can change the integration parameter from optical depth, $\phi$, to either altitude, $z$, or pressure, $p$ and obtain:

$$e^{-\phi_\nu/\mu} \cdot \frac{d\phi}{\mu} = \frac{\partial \tau_\nu}{\partial z} dz = \frac{\partial \tau_\nu}{\partial p} dp \tag{4.31}$$

so that

$$R_\nu = \int_{z=0}^{\infty} B_\nu(T(z)) \frac{\partial \tau_\nu}{\partial z} \partial z \tag{4.32}$$

The atmospheric radiance component, $R_a$, is the vertical integral of the Planck radiance as seen through the level to space transmittance

$$R_a(\nu,\theta) = \int_{p=P_s}^{0} B_\nu(T(p)) \cdot \frac{d\tau_\nu^{\uparrow}(p, X, \theta)}{dp} \cdot dp \tag{4.33}$$

This equation is the most important one for atmospheric sounding. In remote sounding the contribution of a single channel usually comes from a narrow vertical region in which $\tau \simeq \frac{1}{2}$. For discrete radiative transfer algorithms the total contribution from the atmosphere is given by the sum of the individual layer contributions over the entire isobaric grid

$$R_a(\nu) = \sum_{L=1}^{N_L} R_L(n) = \sum_{L=1}^{N_L} B_\nu(\overline{T(L)}) \cdot \Delta\tau_\nu^{\uparrow}(L,\theta) \tag{4.34}$$

In the microwave we can utilize the Rayleigh-Jeans approximation for write the total contribution from the atmospheric column in terms of microwave brightness temperature, $\Theta$,

$$\Theta_a(\nu) = \sum_{L=1}^{N_L} \Theta_L(\nu) = \sum_{L=1}^{N_L} \overline{T(L)} \cdot \Delta\tau_\nu^{\uparrow}(L,\theta) \tag{4.35}$$

In the microwave spectrum used for remote sounding we can utilize the channel averaged transmittance because the spectral characteristics of the species used for sounding ($O_2$ and $H_2$) do not

interact with inferring species such as water. This simplifies the atmospheric radiance computation and makes the radiative transfer equation much more linear.

$$\Theta_a(n) = \sum_{L=1}^{N_L} \Theta_L(n) = \sum_{L=1}^{N_L} \overline{T(L)} \cdot \Delta\tau_n^{\uparrow}(L,\theta) \tag{4.36}$$

**Solar Reflected Component**

In a non-scattering atmosphere sunlight is absorbed by the atmospheric particles. We utilize the radiative transfer equation (Eqn. 4.25) with the boundary condition (integration constant) equal to the solar radiance at the top of the atmosphere. The solar energy propagates down to the surface at which point it is reflected into the view of the satellite.

$$R_{\odot} = \rho_{\odot}(\nu,\theta,\theta_{\odot}) \cdot \tau_{\nu}^{\downarrow\uparrow}(p_s,X,\theta,\theta_{\odot}) \cdot \Omega(t) \cdot H_{\odot}(\nu) \cdot \cos(\theta) \tag{4.37}$$

- The reflected solar component requires computation of the transmittance along the bi-directional path from the sun to the surface, $p_s$, and back to the spacecraft. For channel radiances the bi-directional transmittance is NOT equal to the product of the down-welling and up-welling transmittances.

$$\int \tau_{\nu}^{\downarrow\uparrow}(p_s,X,\theta,\theta_{\odot})d\nu \neq \int \tau_{\nu}^{\downarrow}(p_s,X,\theta_{\odot})d\nu \cdot \int \tau_{\nu}^{\uparrow}(p_s,X,\theta)d\nu \tag{4.38}$$

- $H_{\odot}$ is the solar radiance outside the Earth's atmosphere. .
- $\Omega$ is the solid angle, given in terms of the Sun's radius and distance. It varies by $\pm$ 3.4% over the year. $\Omega(t) = \pi \cdot \left(\frac{0.6951 \cdot 10^9}{D_{\odot}(t)}\right)^2 \simeq 6.79 \cdot 10^{-5} - 0.23 \cdot 10^{-5} \cdot \cos(2\pi(t-t_0)/t_y)$ where, $t$ is the time of year, $t_y$ is the time the Earth takes to complete 1 orbit (365.25 days), and $t_0$ is the perihelion date (Jan. 4 or $t_0$=4).
- The solar surface reflectivity, $\rho_{\odot}$, is a function of surface type, zenith angle, solar zenith angle, azimuth angle, and wavenumber.

**Monochromatic down-welling thermal component**

The radiation from an atmospheric layer at $p(L)$ emits radiation in all directions. Some of that radiation reflects off the surface and into the solid angle of observation. The down-welling term requires integration over all zenith angles, $\theta'$, and azimuthal angles, $\alpha$, and all levels.

$$\begin{aligned} R_d(\nu,\theta) &= \tau_{\nu}^{\uparrow}(P_s,X,\theta) \cdot \int_{\alpha=0}^{2\pi} \int_{\theta'=0}^{\frac{\pi}{2}} \rho_{\nu}(\theta,\theta',\alpha) \cdot \sin(\theta') \cdot \cos(\theta') \cdot d\theta' \cdot d\alpha \\ &\quad \cdot \int_{p=P_s}^{0} B_{\nu}(T(p)) \cdot \frac{d\tau_{\nu}^{\downarrow}(p,X,\theta')}{dp} \cdot dp \end{aligned} \tag{4.39}$$

- The thermal reflectivity, $\rho_\nu(\theta, \theta', \alpha)$, is usually a small number $\simeq \frac{1}{\pi}(1-\epsilon_\nu)$ (except over ocean in SWIR and the microwave).
- Effectively, there is a product of up-welling and down-welling transmittance so that this term is only important in channels in which the transmittance is $\approx \frac{1}{2}$.

where we employ the short hand notation for the surface to space transmittance (Eqn. 4.15) and a short hand notation for the down-welling layer transmittance

$$\begin{aligned} \Delta\tau_\nu^\downarrow(L,\theta') &\equiv \tau_\nu(p(L-1) \rightarrow p(L), \theta') && (4.40) \\ &= \tau_\nu(p(L-1) \rightarrow P_s, \theta') - \tau_\nu(p(L) \rightarrow P_s, \theta') && (4.41) \end{aligned}$$

But the monochromatic down-welling transmissivity is related to the upwelling transmissivity by

$$\tau_\nu(p(L) \rightarrow P_s, \theta'_\nu) = \frac{\tau_\nu(P_s \rightarrow 0, \theta'_\nu)}{\tau_\nu(p(L) \rightarrow 0, \theta'_\nu)} \tag{4.42}$$

so that

$$\Delta\tau_\nu^\downarrow(L,\theta'_\nu) = \frac{\tau_\nu(P_s \rightarrow 0, \theta'_\nu)}{\tau_\nu(p(L) \rightarrow 0, \theta'_\nu)} - \frac{\tau_\nu(P_s \rightarrow 0, \theta'_\nu)}{\tau_\nu(p(L-1) \rightarrow 0, \theta'_\nu)} \tag{4.43}$$

Also, since the lines are resolved and not overlapping the channel averaged down-welling transmittance can be written in terms of the upwelling level-to-space channel averaged transmittances in the form shown in Eqn. 4.43

The order of integration can be changed in Eqn. 4.39

$$\begin{aligned} R_d(\nu,\theta) &= \tau_\nu^\uparrow(P_s, X, \theta) \cdot \int_{p=P_s}^{0} B_\nu(T(p)) \\ &\quad \cdot \int_{\alpha=0}^{2\pi} \int_{\theta'=0}^{\frac{\pi}{2}} \rho_\nu(\theta, \theta', \alpha) \cdot \sin(\theta') \cdot \cos(\theta') \cdot d\theta' \cdot d\alpha \cdot \frac{d\tau_\nu^\downarrow(p, X, \theta')}{dp} \cdot dp \end{aligned} \tag{4.44}$$

**Infrared Down-welling Term**

The infrared down-welling term has felt by anyone who has stood out on a warm humid day. The warmth of the hot atmosphere can be larger than the direct solar radiation in the mid- to far-infrared. For an upwelling instrument or in-situ instrument the thermal down-welling integral must be computed properly.

In this section, we will show that for a space-borne measurement only certain channels will have a measurable thermal down-welling radiation and even those channels the effect is still small. We can employ many approximations, including

- because the surface reflectivity, $\rho$, is a small number, usually only a few %

- $\tau^{\uparrow} \cdot \int \tau^{\downarrow}$ is important only when $\tau \simeq \frac{1}{2}$ because when the atmosphere is opaque ($\tau \rightarrow 0$) the surface term vanishes can we cannot "see" the down-welling and when the atmosphere is transmissive ($\tau \rightarrow 1$) there is little down-welling radiance.
- $\alpha$ and $\theta'$ can be approximated by an effective diffusive angle by the mean value theorem.
- Usually the dependence on azimuthal angle is small the integral w.r.t. $\int_0^{2\pi} d\alpha$ can be replaced by $2 \cdot \pi$.

We will begin by assuming that we can represent the thermal reflectivity by a mean value so that Eqn. 4.39 can be written as

$$R_d(\nu, \theta) \simeq \tau_\nu^{\uparrow}(P_s, X, \theta) \cdot \rho(\nu, \theta) \cdot \pi \cdot R_\nu^{\downarrow} \tag{4.45}$$

The factor of $\pi$ arises by assuming azimuthal symmetry, $\int d\alpha = 2\pi$ and assuming we can represent the integral of zenith angle by a diffusive term $\int cos(\theta) sin(\theta) d\theta = \frac{1}{2}$. In Kornfield and Susskind (Mon. Wea. Review **105**, 1977, p. 1605) the down-welling term is shown to be simplified as follows. First, we can insert the surface radiance into the integral

$$R_\nu^{\downarrow} = \int_{\tau(P_s)}^{1} B_\nu(T) \cdot d\tau^{\downarrow} = \int_{\tau(P_s)}^{1} B_\nu(T_s) \cdot d\tau^{\downarrow} + \int_{\tau(P_s)}^{1} (B_\nu(T) - B_\nu(T_s)) \cdot d\tau^{\downarrow} \tag{4.46}$$

the left hand integral can be written exactly

$$R_\nu^{\downarrow} = B_\nu(T_s) \left(1 - \tau_\nu^{\downarrow}(P_s)\right) + \int_{\tau(P_s)}^{1} (B_\nu(T) - B_\nu(T_s)) \cdot d\tau^{\downarrow} \tag{4.47}$$

Most of the absorption takes place very low in the atmosphere, say in the lowest 150 mb (*i.e.,* between 1000 and 850 mb) and $B_\nu(\tau) - B_\nu(T_s)$ is a slowly varying function, therefore, the integral is adequately represented by the mean value theorem

$$R_\nu^{\downarrow} \simeq B_\nu(T_s) \left(1 - \tau_\nu^{\downarrow}(P_s)\right) + \overline{B_\nu(T) - B_\nu(T_s)} \left(1 - \tau_\nu^{\downarrow}(P_s)\right) \tag{4.48}$$

where $\overline{B_\nu - B_\nu(T_s)}$ is the mean difference between atmospheric Planck function and the surface Planck function over the range of most absorption. This equation can be re-written in the form of

$$R_\nu^{\downarrow} \simeq F_\nu \cdot B_\nu(T_s) \left(1 - \tau_\nu^{\downarrow}(P_s)\right) \qquad F_\nu \equiv 1 + \frac{\overline{B_\nu - B_\nu(T_s)}}{B_\nu(T_s)} \tag{4.49}$$

$F_\nu$ differs from unity to the extent that the mean value of the atmospheric Planck function differs from the surface Planck function. Notice that a similar derivation is done in Section **??** resulting in Eqn. **??**.

Now we can see that monochromatic down-welling radiance is a function of the product of $\tau \cdot (1 - \tau)$. The maximum thermal down-welling radiation will occur when $\tau \approx \frac{1}{2}$. For channel averaged transmittances this is not necessarily true as illustrated in the Fig. **??**. In the top example the transmittance is constant across the channel integration whereas in the bottom example the channel is a mixture of opaque and transmissive components. In the top case, $\tau \cdot (1 - \tau)$ is simply

equal to $\frac{1}{4}$, as expected. But in the bottom case $\tau$ is zero everywhere where $1-\tau$ is unity and vice-a-versa. Therefore, the product is zero.

Therefore, the calculation of $\tau \cdot (1-\tau)$ needs to be done in a channel averaged sense; however, we will show shortly that this usually introduces a small error. Given that the entire down-welling radiance is small at the spacecraft the error is tolerable. We can assume that the integral of the monochromatic product of $\tau$ is related to the channel averaged product with a correlation factor, and this will be absorbed into the $F_\nu$ factor. Inserting Eqn. 4.49 into Eqn. 4.45 yields

$$R_d(\nu,\theta) = \pi\rho_\nu(\theta,\bar{\theta}_i)\cdot B_\nu(T_s)F_\nu \cdot \tau_\nu(p_s,\theta)\left(1-\tau_\nu(p_s,\bar{\theta})\right) \tag{4.50}$$

Using the derivation in Section **??** a better fitting equation for channel averaged radiances might be

$$R_d(i,\theta) = \pi\rho_i(\theta,\bar{\theta}_i)\cdot B_{\nu_i}(T(\bar{p}_i))F_i \cdot \tau_i(p_s,\theta)\left(1-\tau_i(p_s,\bar{\theta}_i)\right) \tag{4.51}$$

Where $p_i$ is an effective pressure of down-welling for channel $i$. Each channel could have an effective diffusive angle or the effective diffusive angle, $\theta_i$, could be defined w.r.t. the angle of observation, $\theta$. We can also assume that the bi-directional reflectance is given by either

- $\rho_i(\theta,\bar{\theta}_i) = \frac{1-\epsilon_i}{\pi}$ for nighttime and long-wave (*i.e.,* $\nu_i < 2300$ cm$^{-1}$)
- $\rho_i(\theta,\bar{\theta}_i) = \rho_i(\theta,\theta_\odot)$ for daytime short wave channels.

To estimate the thermal down-welling term we can calculate an approximate form of the down-welling term using the nadir rapid algorithm

$$R_d(\nu,\theta) = \frac{1}{2}\cdot(1-\epsilon(\nu))\cdot\tau(p_s)\cdot(1-\tau(p_s))\cdot B_\nu(T(\bar{p}=700) \tag{4.52}$$

To first order, if we ignored the effect entirely, a larger $\epsilon_i$ would be determined and radiance residuals would be smaller.

### The Rapid Transmittance Algorithm

This fast transmittance model is based on methods developed and used by Larry McMillan, Joel Susskind, and others. An introduction to the theoretical development of the approximations employed can be found in: McMillin and Fleming (1976), McMillin *et al.* 1995b, Hannon *et al.* 1996, Strow *et al.* 1998, and Strow *et al.* 1998.

a. Select the Regression Profiles:

   48 regression profiles were chosen that cover the realistic range of profile variability. Each profile consists of temperature and gas amounts of 4 variable gases: water, ozone, carbon monoxide, and methane. All other gases are "fixed" (do not vary in amount with profile).

b. Calculate Monochromatic Transmittances:

   Monochromatic layer-to-space transmittances for the regression profiles are computed. This was done using our KCARTA package. The layer-to-space transmittances are grouped into sets of "mixed" gases. For this production, there were 4 different ways in which the gases were grouped, depending upon the frequency region:

   FOW : 3 groups of transmittances: F, FO, FOW

FOWp : 4 groups of transmittances: F, FO, FOW, FOWp

FMW : 3 groups of transmittances: F, FM, FMW

FCOWp: 5 groups of transmittances: F, FC, FCO, FCOW, FCOWp

where F refers to "fixed" gases, W to water, O to ozone, C to carbon monoxide, and M to methane. The "p" refers to perturbed CO2, in which the CO2 amount has been increased by +5"FM" refers to the transmittance of the "fixed" gases and methane together.

For channels under 1620 cm-1, 6 angles were computed with the secant angles equal to 1.00 1.19 1.41 1.68 1.99 2.37. For the shortwave channels 6 additional angles were added to extend out to the larger angles need for the for reflected solar radiance: 2.84 3.47 4.30 5.42 6.94 9.02

c. Convolve the Transmittances:

The monochromatic transmittances are convolved with the appropriate Spectral Response Functions (SRF). For this production run, there was a separate SRF for each channels. The SRFs are based upon laboratory measurements of the SRFs. In particular, we used interpolations of measurements for test 261, with the wings added on using a model. The channels in module 11 which are based on test 266 due to noise problems with test 261 for that module.

d. Calculate Effective Layer Transmittances:

For each layer, the convolved layer-to-space transmittances are ratio-ed with transmittances in the layer above to form effective layer transmittances for fixed, water, ozone, CO, methane, and perturbed CO2 are:

```
For FOW:
   Feff(L) = F(L)/F(L-1)
   Oeff(L) = ( FO(L)/F(L) )/( FO(L-1)/F(L-1) )
   Weff(L) = ( FOW(L)/FO(L) )/( FOW(L-1)/FO(L-1) )
 For FOWp:
   Feff(L) = F(L)/F(L-1)
   Oeff(L) = ( FO(L)/F(L) )/( FO(L-1)/F(L-1) )
   Weff(L) = ( FOW(L)/FO(L) )/( FOW(L-1)/FO(L-1) )
   peff(L) = ( FOWp(L)/FOW(L) )/( FOWp(L-1)/FOW(L-1) )
For FMW:
   Feff(L) = F(L)/F(L-1)
   Meff(L) = ( FM(L)/F(L) )/( FM(L-1)/F(L-1) )
   Weff(L) = ( FMW(L)/FM(L) )/( FMW(L-1)/FM(L-1) )
For FCOWp:
   Feff(L) = F(L)/F(L-1)
   Ceff(L) = ( FC(L)/F(L) )/( FC(L-1)/F(L-1) )
   Oeff(L) = ( FCO(L)/FC(L) )/( FCO(L-1)/FC(L-1) )
   Weff(L) = ( FCOW(L)/FCO(L) )/( FCOW(L-1)/FCO(L-1) )
   peff(L) = ( FCOWp(L)/FCOW(L) )/( FCOWp(L-1)/FCOW(L-1) )
The zeroeth layer transmittance (ie when L-1=0) is taken to be exactly 1.0.
```

e. Regress the Effective Layer Transmittances and Predictors:

The effective layer transmittances are converted to optical depth (by taking the negative of the logarithm ), and then weighted according to some estimated relative importance. A regression is done on this data with a set of profile dependent predictors (see note below) as the independent variables. The regression, which is of the form A*X=B, where A is a matrix of predictors and B is the data, calculates X, the fast transmittance coefficients.

Note: The predictors are generally various combinations of the main profile variables such as the temperature and gas amount, as well as the satellite viewing angle. One of the most time consuming and tiring aspects in developing a fast model using this method is in selecting/inventing the optimum set of predictors. It is essentially a trial and error exercise; try somthing and see how it works.

The fast transmittance coefficients may be used to quickly compute effective layer transmittances for almost any desired profile simply by calculating the appropriate predictor values for the profile and multiplying them by the coefficients. The individual component gases ("fixed", water, ozone, CO, methane, and the far-wing water continuum) are calculated separately. The total layer transmittance is the product of the individual component transmittances.

## 4.7 References

Burns, B., X. Wu and G.R. Diak 1997. Effects of precipitation and cloud ice on brightness temperatures in AMSU moisture channels. IEEE Trans. Geosci. Remote Sens. v.35 p.1429-1437.

Chandrasekar, S. 1960. Radiative Transfer. *Dover*, New York

Fleming, H.E. and L.M. McMillin 1977. Atmospheric transmittance of an absorbing gas. 2. A computationally fast and accurate transmittance model for slant paths at different zenith angles. Applied Optics v.16 p.1366-1370.

A. Gambacorta, C.D. Barnet, W.W. Wolf, T.S. King, E.S. Maddy, N.R. Nalli, X. Xiong, A methodology for computing systematic biases of the top of atmosphere brightness temperature calculations. Part I: Infrared brightness temperature computations. A case study using the Cross-track Infrared Instrument (CrIS), IEEE geoscience and remote sensing, in submission, 2013a.

A. Gambacorta, C.D. Barnet, W.W. Wolf, T.S. King, E.S. Maddy, N.R. Nalli, X. Xiong, A methodology for computing systematic biases of the top of atmosphere brightness temperature calculations. Part II: Microwave brightness temperature computations. A case study using the Advanced Techonology Microwave Sounder (ATMS), IEEE geoscience and remote sensing, in submission, 2013b.

Hanel, R.A. 1983. Planetary exploration with space-borne Michelson interferometers in the thermal infrared. In *Spectroscope Techniques*, Vol. III, G.A. Vanasse (ed.), Academic, New York, pp. 43-135.

Hannon, S.E., L.L. Strow and W.W. McMillan 1996. Atmospheric infrared fast transmittance models: a comparison of two approaches. SPIE v.2830 p.94-105.

Janssen, M.A. 1993. Atmospheric remote sensing by microwave radiometry. John Wiley and Sons, Inc, New York.

Kleespies, T,J, P. V. Delst, L. M. McMillin, and J. Derber 2004. Atmospheric transmittance of an absorbing gas. 6. An OPTRAN status report and introduction to the NESDIS/NCEP community radiative transfer model, Accepted by *Appl. Opt.*.

Klein, L.A. and C.T. Swift 1977. "An improved model for the dielectric constant of sea water at microwave frequencies." *IEEE Trans. on Ant. and Prop.* **25** p.104-114.

Kornfield, J. and J. Susskind 1977. "On the effect of surface emissivity on temperature retrievals." Monthly Weather Review **105** pp.1605-1608.

McMillin, L.M., L.J. Crone and T.J. Kleespies 1995b. Atmospheric transmittance of an absorbing gas. 5. Improvements to the OPTRAN approach. Applied Optics v.34 p.8396-8399.

McMillin, L.M., L.J. Crone, M.D. Goldberg and T.J. Kleespies 1995a. Atmospheric transmittance of an absorbing gas. 4. OPTRAN: a computationally fast and accurate transmittance model for absorbing gases with fixed and ... Applied Optics v.34 p.6269-6274.

McMillin, L.M. and C. Dean 1982. Evaluation of a new operational technique for producing clear radiances. J. Appl. Meteor. **21** p.1005- 1014.

McMillin, L.M., H.E. Fleming and M.L. Hill 1979. Atmospheric transmittance of an absorbing gas. 3. a computationally fast and accurate transmittance model for slant paths at different zenith angles. Applied Optics v.18 p.1600-1606.

McMillin, L.M. and H.E. Fleming 1976. Atmospheric transmittance of an absorbing gas: a computationally fast and accurate model for absorbing gases with constant mixing ratios in inhomogeneous atmospheres. Applied Optics v.15 p.358-363.

Mihalas, D. 1978. Stellar Atmospheres, 2nd edition. *W.H. Freeman and Company* San Francisco, 632 pages.

Rosenkranz, P.W. 1995. A rapid atmospheric transmittance algorithm for microwave sounding frequencies. IEEE Trans. Geosci. Remote Sens. v.33 p.1135-1140.

Strow, L.L., H.E. Motteler, R.G. Benson, S.E. Hannon and De Souza-Machado, S 1998. Fast-computation of monochromatic infrared atmospheric transmittances using compressed look-up tables. J. Quant. Spectrosc. Radiat. Transfer v.59 p.481-493.

Strow, L.L., D.C. Tobin, W.W. McMillan, S.E. Hannon, W.L. Smith, H.E. Revercomb and R.O. Knuteson 1998. Impact of a new water vapor continuum and line shape model on observed high resolution infrared radiances. J. Quant. Spectrosc. Radiat. Transfer v.59 p.303-317.

Thekaekara, M.P. 1973. Solar Energy **14**, p.109-127

Xiong, X. and L.M. McMillin 2004. An Alternative to the Effective Transmittance approach for Calculating Polychromatic Transmittances in Rapid Transmittance Models, Submitted to *Appl. Opt.*.

Xiong, X., C. Barnet, E. Maddy, C. Sweeney, X. Liu, L. Zhou, and M. Goldberg, 2008, Characterization and validation of methane products from the Atmospheric Infrared Sounder (AIRS), J. Geophys Res., 113, G00A01, doi:10.1029/2007JG000500.

Wiscombe, W.J and J.W. Evans 1977. Exponential sum fitting of radiative transmission functions. *J. Computational Physics* **24** p. 416-444.

# Chapter 5

# Description of the Core Retrieval Algorithm
# Step I: Microwave Retrieval Algorithm

## 5.1 Introduction

The NUCAPS microwave module is a heritage algorithm of the AIRS Science Team microwave retrieval algorithm [Rosenkranz, 2000, 2006]. The reader is referred to the AIRS ATBD for an in depth description of the subject of this chapter.

## 5.2 Precipitation Flags, Rate Retrieval and ATMS Corrections

The precipitation algorithm produces the following: (1) flags indicating possible precipitation-induced perturbations impacting ATMS channels 5, 6, 7, 8, and 9, (2) estimates of corrections that may, at the user's option, be applied to ATMS brightness temperatures for channels 5, 6, 7, 8 and 9, to compensate for precipitation, if present, and (3) a precipitation-rate retrieval (mm/h) for each 50-km ATMS spot which was tuned for mid-latitudes using all-season NEXRAD data.

### 5.2.1 Precipitation Flags

The objective of the flags for each of ATMS channels 5-9 is to alert users of this data to the possibility that retrievals based on these microwave channels might be impacted by precipitation. The four possible flag states are the following. Flag = 0: The magnitude of the detected precipitation perturbations (if any) are less than 0.5 K; Flag = 1: Small perturbations are present (nominally between 0.5 and 2 K), which are approximately correctable; Flag = 2: Estimated ATMS precipitation-induced brightness temperature perturbations for this channel may exceed 2 K in magnitude, so perturbation corrections are less reliable; Flag = -1 It is unknown whether perturbations due to precipitation are present (e.g., surface elevation greater than 2 km). These perturbations are discussed further later in this chapter.

### 5.2.2 Perturbation Corrections

Perturbation corrections are entirely based on the methodology employed for the AMSU instrument. The reader is referred to the AIRS ATBD and the reference therein for a complete description of the methodology.

Perturbation corrections are estimated for ATMS Channels 5, 6, 7, 8 and 9. In addition, for each ATMS beam position a precipitation-rate estimate (mm/h) is provided when flag states 0, 1, or 2 exist for ATMS channel 5 (52.8 GHz). Users of ATMS data for temperature profile retrievals should use brightness temperatures flagged with 2 or -1 with caution, even if the suggested perturbation corrections are employed. These perturbations are computed for ATMS channels 5-9 at 50-km resolution using the algorithm discussed further down. It should be noted that 52.8-GHz brightness temperatures can suffer warm perturbations over ocean due to low altitude absorption and emission by clouds or precipitation. Such warm perturbations could be flagged and corrected as are the cold perturbations. The 23.8/31.4 GHz combination could be used to validate the locations of such excess absorption and perturbations over ocean.

### 5.2.3 Rain Rate Retrieval Algorithm

The rain rate retrieval algorithm is an adaptation of the AQUA AMSU-A AMSU-B algorithm. The reader is referred to the AIRS ATBD for an in depth description of this methodology.

Accurate remote sensing of precipitation rate is challenging because the radiometric signatures of irregularly formed hydrometeors can depend strongly on their distributions in size, temperature, ice content and structure. As a result, all active and passive microwave remote sensing methods rely on the statistical regularity of precipitation characteristics. Experimental validation typically involves comparisons with rain gauges, radar, and other sensors, each of which has its own limitations. The primary precipitation-rate retrieval products of ATMS are 15- and 50-km resolution contiguous retrievals over the viewing positions of ATMS within 43 of nadir. The two outermost 50-km viewing positions (six outermost for 15-km) on each side of the swath are currently omitted due to their grazing angles. The algorithm architectures for these two retrieval methods are presented below.

The 15-km resolution precipitation-rate retrieval algorithm begins with identification of potentially precipitating pixels. All 15-km pixels with brightness temperatures at 183 7 GHz that are below a threshold $T_7$ are flagged as potentially precipitating, where:

$$T_7 = 0.667(T_{53.6} - 248) + 252 + 6 \cdot cos(\Theta) \tag{5.1}$$

and where $\Theta$ is the satellite zenith angle. If, however, the spatially filtered brightness temperature $T_{53.6}$ at 53.6 GHz is below 249 K, then the brightness temperature at 183 3 GHz is compared instead to a different threshold $T_3$, where:

$$T_3 = 242.5 + 5 \cdot cos(\Theta) \tag{5.2}$$

This spatial filter picks the warmest spot within an array of ATMS pixels. The 1833-GHz band is used to flag potential precipitation when the 1837-GHz flag could be erroneously set by low surface emissivity in very cold dry atmospheres, as indicated by $T_{53.6}$. These thresholds $T_7$ and $T_3$ are slightly colder than a saturated atmosphere would be, therefore lower brightness temperatures imply the presence of a microwave-absorbing cloud. If the locally filtered $T_{53.6}$ is less than 242 K, then the pixel is assumed not to be precipitating. Within these flagged regions strong precipitation is generally characterized by cold cloud-induced perturbations of the ATMS tropospheric temperature

sounding channels in the range 52.5-55.6 GHz. Examples of 1837-GHz data and the corresponding cold perturbations at 52.8 GHz are illustrated in Figures 5.3(a) and (c), respectively, of the AIRS ATBD (see reference). These 50-km resolution 52.8-GHz perturbations $\Delta T_{50,52.8}$ are then used to infer the perturbations $\Delta T_{15,52.8}$ (see Figure 5.3(d) of AIRS ATBD) that might have been observed at 52.8 GHz with 15-km resolution had those perturbations been distributed spatially in the same way as the cold perturbations observed at either 183 7 GHz or 183 3 GHz, the choice between these two channels being the same as described above. This requires the bi-linearly interpolated 50-km AMSU data to be resampled at the HSB beam positions. These inferred 15-km perturbations are computed for five ATMS channels using:

$$\Delta T_{15,54} = (T_{15,183}/\Delta T_{50,183})\Delta T_{50,54} \tag{5.3}$$

The perturbation $\Delta T_{15,183}$ near 183 GHz is defined to be the difference between the observed brightness temperature and the appropriate threshold given above. The perturbation $\Delta T_{50,54}$ near 54 GHz is defined to be the difference between the limband- surface-corrected brightness temperature and its Laplacian-interpolated brightness temperature based on those pixels surrounding the flagged region (Staelin and Chen, IEEE Trans. Geosci. Remote Sensing, vol. 38, pp. 2232-2332, Sept. 2000). Limb and surface-emissivity corrections to nadir for the five 54-GHz channels are produced by neural networks for each channel; they operate on nine AMSU-A channels above 52 GHz, the cosine of the viewing angle $\Phi$ from nadir, and a land-sea flag (see Figure 5.2 of AIRS ATBD). They were trained on 7 orbits spaced over one year for latitudes up to 55o. Inferred 50- and 15-km precipitation-induced perturbations at 52.8-GHz are shown in Figures 5.3 (c) and (d), respectively, of AIRS ATBD, for a frontal system. Such estimates of 15-km perturbations near 54 GHz help characterize heavily precipitating small cells.

Such inferred 15-km resolution perturbations at 52.8, 53.6, 54.4, 54.9, and 55.5 GHz are then combined with 1) the 1831-, 3-, and 7-GHz 15-km ATMS data, 2) the leading three principal components characterizing the original five corrected 50-km ATMS temperature brightness temperatures, and 3) two surface-insensitive principal components that characterize the window channels at 23.8, 31.4, 50.3, and 89 GHz, plus the 166.31 and the five 183 GHz channels. channels. All 13 of these variables, plus the secant of the satellite zenith angle $\Theta$, are input to the neural net used for 15-km precipitation rate retrievals, as shown in Figure 5.2 of AIRS ATBD. This network was trained to minimize the rms value of the difference between the logarithms of the ATMS and NEXRAD retrievals; use of logarithms prevented undue emphasis on the heaviest rain rates, which were roughly three orders of magnitude greater than the lightest rates. Adding 1 mm/h prevented undue emphasis on the lightest rates. NEXRAD precipitation retrievals with 2-km resolution were smoothed to approximate Gaussian spatial averages that were centered on and approximated the view-angle distorted 15- or 50-km antenna beam patterns. The accuracy of NEXRAD precipitation observations are known to vary with distance, so only points beyond 30 km but within 110 km of each NEXRAD radar site were included in the data used to train and test the neural nets. Eighty different networks were trained using the Levenberg-Marquardt algorithm, each with different numbers of nodes and water vapor principal components. A network with nearly the best performance over the testing data set was chosen; it used two surface-blind water vapor principal components, and only slightly better performance was achieved with five water vapor principal components with increased surface sensitivity. The final network had one hidden layer with 5 nodes that used the tanh sigmoid function. These neural networks are similar to those described by Staelin and Chen (IEEE TGARS, vol. 38, no. 5, pp. 2232-2332, 2000). The resulting 15-km resolution precipitation retrievals are then smoothed to yield 50-km retrievals. The 15-km retrieval neural network was

trained using precipitation data from the 38 orbits listed in Table 5.1.1. Each 15-km pixel flagged as potentially precipitating using 183 7 GHz or 183 3 GHz brightness temperatures was used either for training, validation, or testing of the neural network. For these 38 orbits over the United States 15,160 15-km pixels were flagged and considered suitable for training, validation, and testing; half were used for training, and one-quarter were used for each of validation and testing, where the validation pixels were used to determine when the training of the neural network should cease. Based on the final ATMS and NEXRAD 15-km retrievals, approximately 14 and 38 percent, respectively, of the flagged 15-km pixels appear to have been precipitating less than 0.1 mm/h for the test set.

## 5.3 Profile Retrieval Algorithm

The microwave initial guess profile retrieval algorithm derives temperature, water vapor and non-precipitating cloud liquid water profiles from ATMS brightness temperatures. This module was originally intended to provide the starting point for the cloud clearing and retrieval algorithm but has been later replaced by a cloudy regression solution. Nonetheless, ATMS has improved spectral resolution and coverage with respect to previous AMSU/HSB and AMSU/MHS instruments. Since the ATMS retrieval performance is still under exam, it has been decided to leave it as part of the NUCAPS processing flow.

The microwave retrieval algorithm is an iterative algorithm in which the profile increments are obtained by the minimum-variance method, using weighting functions computed for the current temperature and moisture profiles with the rapid transmittance algorithm described later in this document. The input vector of measured brightness temperatures is accompanied by an input validity vector whose elements are either one or zero. This provides a way of handling missing or bad data.

### 5.3.1 Preliminary Surface Type Classification

The surface classification algorithm is diagrammed in Figure 5.4 of AIRS ATBD. The classification rules are from Grody et al. (2000), and make use of discriminant functions that are linear combinations of ATMS channels 1, 2, 3, and 16. If sea ice is indicated by the classification algorithm, then its concentration fraction is estimated from a linear operation on channels 1, 2, and 3. If the surface type is glacier or snow-covered land, then the snow or ice fraction is estimated using channels 3 and 16. Parameters of the surface brightness model are assigned according to surface type as in Table 5.1. A priori emissivities for the ice and snow types were estimated from NOAA-15 and Aqua data. For land $\epsilon_o = 0.95$ at all frequencies; for seawater, the dielectric constant model of Ellison et al. (2003) was used to compute the emissivity of a flat surface viewed in the polarization of the ATMS radiometer.

### 5.3.2 Atmospheric Moisture and Condensation Model

Brightness temperatures at the ATMS channel 16 -22 depend on the vertical profile of atmospheric opacity relative to temperature, but do not by themselves distinguish, at any given altitude, between opacity due to water vapor and opacity due to liquid water. However, the physics of water vapor condensation add some a priori information or constraints. Cloud coverage is parameterized as in a stratiform condensation model, where a relative humidity threshold determines the onset of condensation. Although the water vapor profile is saturated within the cloudy part of the field of

view, it is assumed that the condensation process is not spatially resolved, hence the threshold is less than 100% relative humidity. Currently, the threshold is set to 85%.

In the condensation model, the vapor and cloud liquid water density profiles are both linked to a single parameter$H$. When $H$ is <= 85%, H is equal to relative humidity; in the range 85% to 115%, changes from a water-vapor variable to liquid-water, and values of $H$ greater than 115% increase liquid water while the vapor remains at saturation. Because convergence, to be discussed later, is determined from the brightness temperature residuals, which in turn are computed using the vapor and liquid column densities, the role of $H$ in this algorithm is only to introduce the textita priori statistics and constraints. The average vapor density in the field of view is related to $H$ by

$$\rho_\nu = \rho_s \cdot [ramp(H, 10) - f(H)]/10 \tag{5.4}$$

where $\rho_s$ is the saturation value of mixing ratio and:

$$\text{ramp}(x, c) = x; x \geq c \tag{5.5}$$

$$\text{ramp}(x, c) = c \cdot \exp(x/c - 1); x < c \tag{5.6}$$

and

$$f(H) = ramp(H - H_L, 6) \tag{5.7}$$

Thus, the value of $\rho_\nu/\rho_s$ lies between zero and $H_L/100$. the liquid water mixing ratio averaged over the field of view is assumed to be given by:

$$\rho_L = c_1 \cdot f(H) \tag{5.8}$$

where $c_1$ is a coefficient equivalent to a liquid/air mass mixing ratio of $10^{-5}$ %.

The saturation vapor mixing ratio is computed from the temperature profile by the formula of Liebe (1981). Saturation is calculated with respect to liquid water (by extrapolation) even when the temperature is below 273 K. This model therefore allows supercooled liquid water and water vapor greater than the saturation value with respect to ice.

### 5.3.3 Estimation of surface brightness and atmospheric moisture

This section is taken from the AIRS ATBD, chapter 5 and describes an algorithm based on retrieval methods described by Wilheit (1990), Kuo et al. (1994), Wilheit and Hutchison (1997), and Rosenkranz (2006).

It uses ATMS channels 1, 2, 3, 16 - 22. The measurements are weighted averages over 3x3 spatial arrays which approximate the AMSU-A field of view. The H profile, $H_L$, and four surface parameters $T_0$, $T_1$, $T_2$, and $p_g$ are concatenated into a vector Y. The parameter $p_g$ when the surface type is either water or coastline, determines the secant ratio $\rho$ by:

$$\rho = sec(\Theta_{ref})/sec(\Theta) = 1 + ramp(p_\rho, 0.02) \tag{5.9}$$

The cost function to be minimized is given by:

$$(Y_{est} - Y_o)^T S_Y^{-1}(Y_{est} - Y_o) + (\Theta_{obs} - \Theta - \Theta')^T (S_e = S_f)^{-1}(\Theta_{obs} - \Theta - \Theta')$$

in which $Y_{est}$ is the estimate of Y, $Y_o$ is its a priori value and $S_Y$ is its covariance matrix with respect to $T_o$. $\Theta_{obs}$ is a vector of the eight measured sntenna temperatures, $S_e$ is their error covariance matrix (assumed diagonal), $\Theta'$ is the tuning correction for sidelobe effects and possible transmittance error, and $\Theta$ is a brightness temperature vector computed from the current values of temperature, moisture and surface brightness. $S_f$ is a diagonal covariance matrix which approximately represents errors in $\Theta$ resulting from errors in the temperature profile retrieval and tuning.

The estimate of Y is obtained by Newtonian iteration (see Rodgers, 1976), except that Eyres (1989) method of damping is used to avoid large relative humidity increments, because of the nonlinearity of the problem.

### 5.3.4 iteration procedure and convergence tests

Convergence is tested separately for the temperature channels and for the moisture/surface channels. Iteration of either part of the algorithm is suspended when one of the following conditions is met : (1) the computed brightness temperature vector $\Theta$ meets the closure criterion; or (2) when successive computations of the residuals change by less than 1% for temperature channels and 2% for water vapor channels of a given threshold; or (3) when the number of iterations exceeds a preset limit, which is 12 for the temperature channels and 16 for the moisture/surface channels. Typically, iteration of the temperature profile ceases after one or two iterations, but the moisture profile often requires six or more iterations.

## 5.4 References

Chedin, A., N. A. Scott, C. Wahiche, and P. Moulinier, 1985: The improved initialisation inversion method: A high resolution physical method for temperature retrievals from the TIROS-N series. J. Clim. Appl. Meteor., 24, 128-143.

Ellison, W. J., S. J. English , K. Lamkaouchi, A. Balana, E. Obligis, G. Deblonde, T. J. Hewison, P. Bauer, G. Kelly and L. Eymard, 2003: "A comparison of ocean emissivity models using the Advanced Microwave Sounding Unit, the Special Sensor Microwave Imager, the TRMM Microwave Imager, and airborne radiometer observations," J. Geophys. Res., 108(D21), 4663, doi:10.1029/2002JD003213.

Eyre, J. R., 1989: Inversion of cloudy satellite sounding radiances by nonlinear optimal estimation. I: Theory and simulation for TOVS. Q. J. R. Meteorol. Soc. , 115, 1001-1026.

Grody, N., F. Weng, and R. Ferraro, 2000: "Application of AMSU for obtaining hydrological parameters." In Microwave Radiometry and Remore Sensing of the Earths Surface and Atmosphere, (P. Pampaloni and S. Paloscia, eds.) VSP (ISBN 90-6764-318-1), pp. 339-352.

Kistler, R., E. Kalnay, W. Collins, S. Saha, G. White, J. Woollen, M. Chelliah, W. Ebisuzaki, M. Kanamitsu, V. Kousky, H. van den Dool, R. Jenne, and M. Fiorino, 2001: "The NCEP-NCAR 50-Year Reanalysis: Monthly Means CD-ROM and Documentation," Bull. Am. Meteor. Soc. 82, 247-267.

Kuo, C. C., D. H. Staelin and P. W. Rosenkranz, 1994: Statistical Iterative Scheme for Estimating Atmospheric Relative Humidity Profiles, IEEE Trans. Geosci. and Remote Sensing , 32, 254-260.

Liebe, H. J., 1981: "Modeling attenuation and phase of radio waves in air at frequencies below 1000 GHz," Radio Sci., 16, 1183-1199.

Rodgers, C. D., 1976: Retrieval of atmospheric temperature and composition from remote measurements of thermal radiation. Rev. Geophys. and Space Phys., 14, 609-624.

Rosenkranz, P. (2000), Retrieval of temperature and moisture pro

les from AMSU-A and 198 AMSU-B measurements, IEEE, 39, 2429.

Rosenkranz, P. W., 2006: "Cloud liquid-water profile retrieval algorithm and validation," J. Geophys. Res., 111, D09S08, doi:10.1029/2005JD005832.

Schaerer, G. and T. T. Wilheit, 1979: A passive microwave technique for profiling of atmospheric water vapor. Radio Science, 14, 371-375.

Wilheit, T. T., 1990: An algorithm for retrieving water vapor profiles in clear and cloudy atmospheres from 183 GHz radiometric measurements: Simulation studies. J. App. Meteor., 29, 508-515.

Wilheit, T. T., and K. D. Hutchinson, 1997: Water vapour profile retrievals from the SSM/T-2 data constrained by infrared-based cloud parameters. Int. J. Remote Sensing, 18, 3263-3277.

# Chapter 6

# Description of the Core Retrieval Algorithm
# Step II: Regression Retrieval

## 6.1 Post-Launch First Guess Regression Procedure

NOAA/NESDIS uses an eigenvector global regression procedure to provide fast and accurate initial guesses for temperature and moisture profiles as well as surface emissivity and reflectivity using simulated CrIS data. Eigenvector regression for atmospheric sounding was first demonstrated by Smith and Woolf (1976). It is assumed that all independent CrIS radiances have been preprocessed by the cloud clearing module described in the last section. Eigenvectors are computed from a training dataset of radiances that have been normalized by the CrIS expected noise and are used as basis functions to represent the CrIS radiometric information. Eigenvectors are commonly referred to as Empirical Orthogonal Functions (EOF's) in the literature, a convention that will be adopted throughout the remainder of this section. Because of the large number of channels measured by CrIS, the eigenvector form of regression is crucial for exploiting the information content of all channels in a computationally efficient form. By representing radiometric information in terms of a reduced set of EOF's (much fewer in number than the total number of instrument channels) the dimension of the regression problem is reduced by approximately one order of magnitude. Another advantage of using a reduced set of EOF's is that the influence of random noise is reduced by elimination of higher order EOF's which are dominated by noise structure. It should be noted that if all EOF's are retained as basis functions the eigenvector regression reduces to the ordinary least squares regression solution in which satellite measurements are used directly as predictors. The mathematical derivation of the EOF regression coefficients is detailed in the following sub-sections.

### 6.1.1 Generating the Covariance Matrix and Regression Predictors

A training ensemble of temperature, humidity, and ozone profile data are used to generate radiances for all CrIS channels that meet specified instrument performance. Expected instrumental noise is added to the simulated radiances. Note that real observations will be used after launch to generate the eigenvectors. Computed radiances are only used for prelaunch coefficients. The deviations of the radiance scaled by noise from their sample mean are stored in the matrix $\Delta\tilde{\Theta}_{n(m),j}$ (see Eqn. 6.1), a matrix of dimensions $[m = 1, M \; j = 1, J]$, where $M$ is the total number of instrument channels and $J$ is the sample size of the training data set. We begin by normalizing the measured radiances,

$R(n(m)$, for a subset of channels $n(m)$, by the measured instrument noise, NE$\Delta$N$(n(m))$. The noise scaled radiance covariance matrix from which the EOF's are derived is then generated as follows:

$$\Delta\tilde{\Theta}_{n(m),j} \equiv \frac{R_{n(m),j}}{\mathrm{NE}\Delta\mathrm{N}_n(m)} - \frac{< R_{n(m),j} >_j}{\mathrm{NE}\Delta\mathrm{N}_n(m)} \equiv \frac{R_{n(m),j}}{\mathrm{NE}\Delta\mathrm{N}_n(m)} - < \tilde{\Theta} >_{n(m)} \quad (6.1)$$

We compute the eigenvectors of the signal to noise covariance of $\Delta\tilde{\Theta}_{n(m),j}$. For the CrIS v1.0 regression two days were determined to be adequate to describe the entire variance of radiances: may 15th, 2012 and September 20th, 2012.

$$\Theta_{\mathrm{cov}} \equiv \frac{1}{J}\sum_{j=1}^{J} \Delta\tilde{\Theta}_{n(m),j} \cdot \Delta\tilde{\Theta}_{j,n(m)}(\theta) = E^T_{n(m)),k} \cdot \Lambda_{k,k'} \cdot E_{k',n(m)} \quad (6.2)$$

The diagonal elements of represent the variance of the respective channel noise scaled radiance while the off diagonal elements represent the covariance between pairs of channels. An eigenvector decomposition is performed on the matrix giving:

The eigenvectors of the normalized signal-to-noise covariance are orthogonal and $\Lambda_{k,k'}$ is a diagonal matrix with elements equal to $\lambda_k$. We normalize $\Delta\Theta\Delta\Theta^T$ by the number of observations $J$ so that the magnitude of the eigenvalues does not change with the size of the training ensemble.

### 6.1.2 Replacing BAD CrIS Channels using Principal Components

For training of eigenvectors or regression coefficients spectra containing bad channels should be removed from the training ensemble. When applying the regression operationally the use of a bad channel can be quite detrimental, therefore, we need a dynamic ability to remove BAD channels from our algorithm. In the physical algorithm, the channel is simply removed from consideration; however, in regression algorithms a bad channel can seriously degrade the results.

If channel $n_0$ is BAD in radiance set $R_{n,j}$ for case $j$ it be *crudely estimated* by the average value of the neighboring radiances.

$$\Delta\tilde{\Theta}_{n_0,j} = \Delta\tilde{\Theta}_{n_1,j} + \Delta\tilde{\Theta}_{n_2,j} \quad (6.3)$$

where $n_1$ is the closest valid radiance on the low wavenumber side of $n_0$ and $n_2$ is the the closest valid radiance on the high wavenumber side. We begin by using this estimate of the bad radiance to compute an initial guess for the principal component score, $P^0_{k,j}$

$$P^0_{k,j} = \frac{1}{\sqrt{\lambda(k)}} \cdot E_{k,n} \cdot \Delta\tilde{\Theta}_{n,j} \quad (6.4)$$

Once $P^0_{k,j}$ is computed the BAD radiance for channel $n_0$ can be estimated from all the remaining good radiances and our estimate of the bad radiance. This approach can only work if there is redundant information contained within the spectrum. For CrIS the 1305 channels can be represented by approximately 85 principal components, therefore, the is $\approx$ 20:1 redundancy in the CrIS spectrum.

$$\Delta\tilde{\Theta}_{n_0,j} = \sqrt{\lambda(k)} \cdot E^T_{n_0,k} \cdot P^0_{k,j}, \quad \text{where, } n_0 \text{ is the index of the BAD channel} \quad (6.5)$$

Then the principal components can be recomputed from the improved estimate of the bad radiance along with the good radiances.

$$P^1_{k,j} = \frac{1}{\sqrt{\lambda(k)}} \cdot E_{k,n} \cdot \Delta\tilde{\Theta}_{n,j} \tag{6.6}$$

This process can be iterated until $P^i_{k,j}$ converges; however, the first iteration appears to be adequate in operation.

### 6.1.3 NOAA eigenvector file format

The eigenvector file is written out with the following components

- A header block with
  - the number of channels in the subset, $M = 1688$,
  - and the eigenvectors, $K_{store} = 200$
  - A flag if radiances are used (set to T)
  - A flag is the mean is subtracted (set to T)
- The average of $\tilde{\Theta}$ for the $M$ channels

$$< \tilde{\Theta} > \equiv \frac{< R_{n(m),j} >_j}{\mathrm{NE}\Delta\mathrm{N}_n(m)} \tag{6.7}$$

- Each eigenvector, $E_{k,n(m)}$, is written out a single record for each value of $k = 1, K_{store}$.
- The value of $\lambda(k)$ for $k = 1, M$.
- The value of $\mathrm{NE}\Delta\mathrm{N}(n_m))$ for $m = 1, M$.
- The value of $f(n(m))$ for $m = 1, M$.
- The value of $n(m)$ for $m = 1, M$.

### 6.1.4 Post-launch regression computation

The radiances can be represented by their principal component scores. In this algorithm we normalize by the square root of the eigen-value to normalize the principal component scores so that they are numerically significant. Otherwise, the first principal component would have values approximately 1000 times the signal as $P(K_{max})$.

$$P_{k,j} = \frac{1}{\sqrt{\lambda_k}} E_{k,n(m)} \cdot \Delta\tilde{\Theta}_{n(m),j} \tag{6.8}$$

an estimate of the propagated error in the principal components for case $j$, $\delta\hat{P}_{k,j}$, can be given by the root-sum-square (RSS) of the linear combination and an estimate of the error in the radiance for case $j$, $\delta R_{n(m),j}$. This results in an error in the argument of $\delta\tilde{\Theta}_{n(m),j} \equiv \delta R_{n(m),j}/\mathrm{NE}\Delta\mathrm{N}_{n(m)}$ and

$$\delta\hat{P}_{k,j} = \sqrt{\frac{1}{\sqrt{\lambda_k}}\left(E_{k,n(m)} \cdot \delta\tilde{\Theta}_{n(m),j}\right)^2} \tag{6.9}$$

Only $k = 1, K_{max}$ principal components are kept, where $K_{max}$ is the number of significant eigenvalues. The regression is trained using ensembles at similar view angles. Currently, there are four view angle regimes as defined in Table 6.1. A predictor array is constructed using the principal component scores for those cases, $j(v)$ with $\alpha_1(v) < |\alpha| \leq \alpha_2(v)$, where $\alpha$ is the instrument view angle. For AIRS this angle varies from $-48.95° \leq \alpha \leq 48.95°$. The predictor argument for the sub-set of cases is assembled with the first $K_{max}$ elements being set equal to $P_{k,j}$. The element $i = K_{max} + 1$ is set equal to one if $\alpha < 0$ or zero if $\alpha \geq 0$.

$$P_{k,j(v)} = \begin{pmatrix} P_{1,j(v)} \\ P_{2,j(v)} \\ \cdots \\ P_{K_{max},j(v)} \\ \frac{1-sign(v)}{2} \\ 1 - \cos(\frac{\pi \cdot v}{180}) \end{pmatrix} \qquad i = 1, K_{max} + 2 \tag{6.10}$$

Table 6.1: View-angle regimes in post-launch regression

| $v$ | $\alpha_1(v)$ | $\alpha_2(v)$ |
|---|---|---|
| 1 | 53.130 | 42.269 |
| 2 | 42.269 | 31.788 |
| 3 | 31.788 | 19.948 |
| 4 | 19.948 | 0.000 |

Another issue for the regression is that topography limits the available training ensemble for some altitude layers. For each case, $j$, there is a maximum number of vertical levels defined by the surface pressure (that is, some of the 100 layer grid is below the surface). If this lower level is given as $L_{bot}$ then the number of cases in the training ensemble is a function of how many cases have surface pressure above that level, therefore, the number of cases, $J$, in the training ensemble is a function of both view angle and $L_{bot}$ and will can write that index as $j(v, L_{bot})$ which is the subset of cases that satisfy the criteria in Table 6.1 and have valid geophysical parameters in the layer under consideration in $X_i$. See Table 6.2 for a translation from $X_i$ to layer index $L$. We can compute the average predictor argument for this subset ensemble and subtract that from the training ensemble

$$\Delta P_{k,j(v,L_{bot})} = P_{k,j(v,L_{bot})} - < P_{k,j(v,L_{bot})} >_{J(v,L_{bot})} \tag{6.11}$$

The equation we will solve is given by

$$X_{i,j(v,L_{bot})} = < X_{i,j(v,L_{bot})} >_{j(v,L_{bot})} + A^v_{i,k} \cdot \Delta P_{k,j(v,L_{bot})} \tag{6.12}$$

where we can write,

$$\Delta X_{i,j(v,L_{bot})} = X_{i,j(v,L_{bot})} - < X_{i,j(v,L_{bot})} >_{j(v,L_{bot})} \tag{6.13}$$

The geophysical parameters in the NOAA regression are defined in Table 6.2. For moisture the regression is trained on both the $\log_e(r(L))$ and $r(L)$, where $r$ is the mass mixing ratio in grams/kilogram (g/kg).

$$q = \frac{_w \cdot \Delta C_w(L)}{_t \cdot \Delta C_t(L)} = \frac{_w \cdot \Delta C_w(L)}{\frac{_t}{_d} \cdot N_A \cdot 1000 \cdot \frac{\Delta p(L)}{g}} \tag{6.14}$$

If we assume $_t \simeq 0.98 \cdot_d + 0.02 \cdot_w \simeq 1$ and $g = 980.64 \approx 1000$ then we obtain the form used in the code (mx2mr.F), which is

$$q(L) = \frac{_w \cdot \Delta C_w(L)}{N_A \cdot \Delta p(L)} \tag{6.15}$$

and the mass mixing ratio is then given by

$$r_w(L) = \frac{q(L)}{1 - q(L)} \tag{6.16}$$

Table 6.2: Geophysical parameters, $X_i$, solved in NOAA real-time regression (NOTE: $r_w$ = mass mixing ratio of water, $r_o$ = mass mixing ratio of ozone). The index $i$ is used in the data file and the index $L = 1 + (i-1)/4$ is used in a storage vector in the retrieval code.

| $i$ | $L$ | interpretation |
|---|---|---|
| 1 | 1 | $T(1)$ |
| 2 | 1 | $r_w(1)$ |
| 3 | 1 | $\log_e(r_w(1))$ |
| 4 | 1 | $\log_e(r_o(1))$ |
| 5 | 2 | $T(2)$ |
| 6 | 2 | $r_w(2)$ |
| 7 | 2 | $\log_e(r_w(2))$ |
| 8 | 2 | $\log_e(r_o(2))$ |
| ... | ... | |
| 385 | 97 | $T(97)$ |
| 386 | 97 | $r_w(97)$ |
| 387 | 97 | $\log_e(r_w(97))$ |
| 388 | 97 | $\log_e(r_o(97))$ |
| 393 | 99 | $T(P_s)$ |
| 394 | 99 | $r_w(P_s)$ |
| 395 | 99 | $log_e(r_w(P_s))$ |
| 396 | 99 | $log_e(r_o(P_s))$ |
| 397 | 100 | $T_s$ |

and the least square solution is given by

$$A^v_{i,k} = \Delta X_{i,j(v,L_{bot})} \cdot \Delta P^T_{j(v,L_{bot}),k} \cdot \left[\Delta P_{k,j(v,L_{bot})} \cdot \Delta P^T_{j(v,L_{bot}),k}\right]^{-1} \tag{6.17}$$

No regularization is needed since the principal components have been essentially regularized by selecting only 85 of the principal components. Note that the regression coefficients can be related to empirical Kernel functions, $\tilde{K}_n(L)$, for channel $n$ and pressure level $L$

In the eigenvector regression the empirical Kernel functions can be computed by

$$\tilde{K}_n(L) = A_{i(L),k} \cdot E_{k,n} \tag{6.18}$$

where, $i(L)$, is the subset of indices for the selection of the geophysical parameter group (*e.g.*, T(L), is given for $L = 1, 2, 3, \ldots$, which is given by $i = 1, 5, 9, \ldots$ in Table 6.2)

Once $A^v_{i,k}$ is determined we can combine the average of the geophysical parameter given in Eqn. 6.13, $\overline{X}_j \equiv < X_{i,j(v,L_{bot})} >_{j(v,L_{bot})}$, and the average of the predictor given in Eqn. 6.11, $\overline{P}_k \equiv < P_{k,j(v,L_{bot})} >_{J(v,L_{bot})}$ into a single value, called $\overline{A}_i = \overline{X}_i + A_{i,k} \cdot \overline{P}_k$, so that our regression equation can utilize the un-normalized predictors

$$X_{i,j(v,L_{bot})} = \overline{A^v}_i + A^v_{i,k} \cdot P_{k,j(v,L_{bot})} \tag{6.19}$$

where $\overline{A^v}_i$ is defined as

$$\overline{A^v}_i \equiv < X_{i,j(v,L_{bot})} >_{j(v,L_{bot})} \quad - \quad A^v_{i,k} \cdot < P_{k,j(v,L_{bot})} >_{J(v,L_{bot})} \tag{6.20}$$

A propagated error estimate can be computed from the linear combination of principal components

$$\delta\hat{X}_{i,j(v,L_{bot})} = \sqrt{\sum_i \left(A^v_{i,k} \cdot \delta P_{k,j(v,L_{bot})}\right)^2} \tag{6.21}$$

Once the regression matrix is known it is useful to compute the mean and standard deviation of the real error between the regression, applied to the training ensemble radiances, and the geophysical value in the training ensemble. Each case has an error, $\delta X$, given by

$$\delta X_{i,j(v,L_{bot})} = X_{i,j(v,L_{bot})} - \left[\overline{A^v}_i + A^v_{i,k} \cdot P_{k,j(v,L_{bot})}\right] \tag{6.22}$$

For each geophysical parameter we can compute a mean and standard deviation of the regression error (difference of regression from the training values). The mean is given by

$$\overline{\delta X_i} \equiv \frac{1}{J(v, L_{bot})} \sum_j \delta X_{i,j(v,L_{bot})} \tag{6.23}$$

and a standard deviation is given by

$$\sigma(\delta X_i) \equiv \left[\frac{1}{J(v, L_{bot})} \sum_j \left(\delta X_{i,j(v,L_{bot})} - \overline{\delta X_i}\right)^2\right]^{\frac{1}{2}} \tag{6.24}$$

The standard deviation can be compared to the standard deviation of the training ensemble's departure from its mean, given in Eqn. 6.13.

$$\sigma(X_i) \equiv \left[\frac{1}{J(v, L_{bot})} \sum_j \left(\Delta X_{i,j(v,L_{bot})}\right)^2\right]^{\frac{1}{2}} \tag{6.25}$$

### 6.1.5 Applying the NOAA regression

When applying the regression the total precipitable water, TPW, is used to determine which regression to use for the answer. The equation used in the code does not adjust the TPW for dry gas (the equation uses mass mixing ratio instead of specific humidity)

$$\text{TPW} \simeq \sum_{L=1} \frac{r_w}{1000} \cdot \frac{\Delta p(L) \cdot 1000}{g} \tag{6.26}$$

For water If TPW, by this definition, is less 1 or if the mass mixing ratio, $r_w(L)$ is less than zero for any layer then the logarithmic form, $r_w(L) = \log_e(r_w(L))$, of the regression is used. In addition, if the mass mixing ratio exceeds saturation then the saturation value for that layer is used.

A routine from Flatau, Walko, and Cotton (1982) is used within the
where $x$ is for water or ozone. The conversion to layer column density is done by the routine colden.F, which uses the same approximations as done in the training

$$\Delta C_x(L) = \frac{r_x(L) \cdot N_A}{mw_w \cdot 1000 \cdot \Delta p(L)} \tag{6.27}$$

NOTE that presently the conversion from mass mixing ratio to specific humidity is NOT done. I believe this is an error and needs to be fixed (May 2004).

In a system that has performed a microwave physical retrieval of water vapor we can improve the regression solution over ocean if we adjust the regression water vapor to the total column water vapor from the microwave. This is done by summing the layer column densities from the microwave retrieval, $C_w^{\text{MIT}} = \sum \Delta C_w^{\text{MIT}}(L)$, which is the total column density in molecules/cm$^2$. The same calculation is done for the regression retrieval resulting in $C_w^{\text{REG}}$. We then multiply the layer column density by the ratio of the total column densities from the regression and microwave retrieval,

$$\Delta C_w^{\text{ADJ}}(L) = \Delta C_w^{\text{REG}}(L) \cdot \left( \frac{\sum\limits_{L=1} \Delta C_w^{\text{MIT}}(L)}{\sum\limits_{L=1} \Delta C_w^{\text{REG}}(L)} \right) \tag{6.28}$$

This is done in the routine amsu_adj.F.

### 6.1.6 NOAA regression file format

In the NOAA regression file each set of geophysical parameters is written for a view angle block. The index number system for the geophysical parameters is given in Table 6.2 or 6.5. In the profile regression, the 393 parameters (1-388,393-397) are written out in 4 sequential blocks in the regression file. In the surface regression the 39 emissivity regressions are written out first for land and then for ocean.

- A header line for each parameter block contains
  - parameter number (see Table 6.2 or Table 6.5)
  - number of predictors
  - pressure at level $L$ or frequency at emissivity $L$
  - number of cases in training ensemble, $J(v, L_{bot})$ or $J(l)$.
  - the mean of the training ensemble, $< X_{j(v,L_{bot}(L))} >_{j(v,L_{bot})}$
  - the standard deviation of the training ensemble, $\sigma(X(L))$
  - the standard deviation of the error in the training ensemble, $\sigma(\delta X(L))$
- A block of $I + 1$ coefficients, starting with $\overline{A^v}_i$ and then the $I$ values of $A_i(L)$.

### 6.1.7 Post-launch Surface Emissivity Regression

In the case of surface emissivity there is no truth file to train against with real radiance data. In this case, we simulated $J$ cases where the infrared radiances were computed from the ECMWF forecast and a surface emissivity model (Fishbein *et al.*, 2003). The eigenvector approach was not used. In this case, AIRS radiances for window channels, $R(n(m), j)$, were selected for the channels and frequencies given in Table 6.3. The emissivities, $\epsilon(L, j)$, were provided by a model at the 39 frequencies specified in Table 6.4. Notice that short-wave observations are not used to predict short-wave emissivity. This regression relies on statistical correlations between the short-wave and long-wave to solve for these parameters.

In this case, the predictors consisted of the $M$ radiances, written as signal-to-noise (see Eqn. 6.1), and the side of the scan and cosine of the view angle were used as additional predictors. In this case, all J cases see the surface, so there is no subset for topography. Also, window channels require only a minor adjustment for view angle, so the complete ensemble was used. The ocean emissivity is a well modeled function (i.e. the AIRS science team uses the Masuda *et al.* (1988) model as modified by Wu and Smith (1997). and the regression was performed on land and ocean separately. We will indicate the land/ocean by a superscript $l$. Therefore, the predictors are given by

$$P^l_{k,j} = \begin{pmatrix} R_{1,j(l)} \\ R_{2,j(l)} \\ \cdots \\ R_{M,j(l))} \\ \frac{1-sign(v_{j(l)})}{2} \\ 1-\cos(\frac{\pi \cdot v_{j(l)}}{180}) \end{pmatrix} \qquad i = 1, M+2 \tag{6.29}$$

where we can write,

$$\Delta X_{i,j(l)} = X_{i,j(l)} - < X_{j(l)} >_{j(l)} \tag{6.30}$$

with the $X_i$'s defined in Table 6.3
and the least square solution is given by

$$A^l_{i,k} = \Delta X_{i,j(l)} \cdot \Delta P^T_{j(l),k} \cdot \left[\Delta P_{k,j(l)} \cdot \Delta P^T_{j(l),k}\right]^{-1} \tag{6.31}$$

Again, once $A^l_{i,k}$ is determined we can combine the average of the geophysical emissivity parameter and the average of the predictor into a single value, called $\overline{A}_i$, so that our regression equation becomes

$$X_{j(v,L_{bot}(L))} = \overline{A^l}_i + A^l_{i,k} \cdot P_{k,j(v,L_{bot})} \tag{6.32}$$

where $\overline{A^l}_i$ is defined as

$$\overline{A^l}_i \equiv A^l_{i,k} \cdot < P_{k,j(v,L_{bot})} >_{J(v,L_{bot})} \tag{6.33}$$

These regression coefficients have the same format as the ones described in Sub-section 6.1.4

Table 6.3: AIRS channels used in surface emissivity regression

| v7, prior to 4/10/04 | | | v8, after to 4/10/04 | |
|---|---|---|---|---|
| $n$ | f(n), $cm^{-1}$ | | n | f(n), $cm^{-1}$ |
| 475 | 801.00 | | 475 | 801.0990 |
| 484 | 804.29 | | 484 | 804.3860 |
| 497 | 809.08 | | 497 | 809.1800 |
| 528 | 820.73 | | 528 | 820.8340 |
| 587 | 843.81 | | 587 | 843.9130 |
| 787 | 917.21 | | 787 | 917.3060 |
| 791 | 918.65 | | 791 | 918.7470 |
| 843 | 937.81 | | 843 | 937.9080 |
| 914 | 965.32 | | 870 | 948.1840 |
| 950 | 979.02 | | 914 | 965.4310 |
| 1138 | 1072.38 | | 950 | 979.1280 |
| 1178 | 1092.31 | | 1119 | 1063.285 |
| 1199 | 1103.06 | | 1123 | 1065.216 |
| 1221 | 1114.53 | | 1178 | 1092.451 |
| 1237 | 1123.02 | | 1199 | 1103.199 |
| 1252 | 1131.08 | | 1221 | 1114.675 |
| 1263 | 1216.84 | | 1237 | 1123.162 |
| 1285 | 1228.09 | | 1252 | 1131.229 |
| | | | 1263 | 1216.974 |
| | | | 1285 | 1228.225 |

Table 6.4: Frequencies for the 39 point model for emissivity regression

| | | | | |
|---|---|---|---|---|
| 649.35 | 666.67 | 684.93 | 704.22 | 724.64 |
| 746.27 | 769.23 | 793.65 | 819.67 | 847.46 |
| 877.19 | 909.09 | 943.40 | 980.39 | 1020.4 |
| 1063.8 | 1111.1 | 1162.8 | 1204.8 | 1234.6 |
| 1265.8 | 1298.7 | 1333.3 | 1369.9 | 1408.4 |
| 1449.3 | 1492.5 | 1538.5 | 1587.3 | 1639.3 |
| 2173.9 | 2222.2 | 2272.7 | 2325.6 | 2380.9 |
| 2439.0 | 2500.0 | 2564.1 | 2631.6 | |

Table 6.5: Geophysical parameters, $X_i$, solved in NOAA real-time *synthetic* regression of surface emissivity.

| L | interpretation |
|---|---|
| 401 | $\epsilon(1)$ |
| 402 | $\epsilon(2)$ |
| ... | ... |
| 439 | $\epsilon(39)$ |

## 6.2 References for Statistical Regression

Chesters, D., D.A. Keyser, D.E. Larko and L.W. Uccellini 1988. Improved VAS regression soundings of mesoscale temperature features observed during the atmospheric variability experiment on 6 March 1982. in 3rd Conf. Sat. Meteor. & Oceanography p.35-40.

Crone, L.J., L.M. McMillin and D.S. Crosby 1996. Constrained regression in satellite meteorology. J. Appl. Meteor. **35** p.2023-2035.

Goldberg, M.D., Y. Qu, L.M. McMillin, W. Wolf, L. Zhou and M. Divakarla 2003. AIRS near-real-time products and algorithms in support of operational weather prediction. IEEE Trans. Geosci. Remote Sens. v.41 p.379-389.

Fishbein, E., C. B. Farmer, S. L. Granger, D. T. Gregorich, M. R. Gunson, S. E. Hannon, M. D. Hofstadter, S. Y. Lee, S. S. Leroy and L. L. Strow 2003. Formulation and validation of simulated data for the atmospheric infrared sounder (AIRS). *IEEE Trans. Geosci. Remote Sens.* **41** p. 314-329.

Flatau, P.J., R.L. Walko and W.R. Cotton 1992. Polynomial fits to saturation vapor pressure. J. Appl. Meteor. v.31 p.1507-1513.

Fleming, H.E., M.D. Goldberg and D.S. Crosby 1988. Operation implementation of the minimum variance simultaneous retrieval method. in 3rd Conf. Sat. Meteor. & Oceanography p.16-23.

Masuda, K., T. Takashima and Y. Takayama 1988. Emissivity of pure and sea waters for the model sea surface in the infrared window regions. Rem. Sens. Envir. v.24 p.313-329.

Smith, W.L. and H.M. Woolf 1976. The use of eigenvectors of statistical covariance matrices for interpreting satellite sounding radiometer observations. J. Atmos. Sci. v.33 p.1127-1140.

Wu, X. and W.L. Smith 1997. Emissivity of rough sea surface for 8-13 um: modeling and verification. Applied Optics v.36 p.2609-2619.

# Chapter 7

# Description of the Core Retrieval Algorithm
# Step III: Cloud Clearing

Cloud clearing is the process of computing the clear column radiance for a given channel n, and represents what the channel would have observed if the entire scene were cloud free. The entire scene is defined as the ATMS field of regard (FOR) which includes and array of 3x3 CrIS filed of views (FOV).

The cloud clearing approach is based upon the following reasoning. For simplicity of argument, we momentarily consider using only K=2 adjacent FOVs and one cloud formation. The observed radiances in FOV $j = 1$ and 2, corresponding to channel n are given by:

$$R_1(n,\phi_0) = (1-\alpha_1(\phi_0)) \cdot R_{clr}(n,\phi_0) + \alpha_1(\phi_0) \cdot R_{cld}(n,\phi_0) \quad (7.1)$$

$$R_2(n,\phi_0) = (1-\alpha_2(\phi_0)) \cdot R_{clr}(n,\phi_0) + \alpha_2(\phi_0) \cdot R_{cld}(n,\phi_0) \quad (7.2)$$

where $\alpha_1(\phi_0)$ and $\alpha_2(\phi_0)$ are the zenith angle dependent effective cloud fractions for each field of view, $R_{clr}(n,\phi_0)$ is the radiance which would be observed if the entire field of view were clear, and $R_{clr}(n,\phi_0)$ is the radiance which would be observed if the entire field of view were covered by the cloud. The basic assumption of cloud-clearing is that if the observed radiances in each field-of-view are different, the differences in the observed radiances are solely attributed to the differences in the fractional cloudiness in each field of view while everything else (surface properties and atmospheric state) is uniform across the field of regard. A process referred to as *local angle adjustment* is applied to these observed radiances, channel by channel, to generate angle adjusted radiances, $R_j(n,\phi_0)$, representative of the radiance that CrIS channel n would have observed in FOV j if the observation were taken at the satellite zenith angle of the center FOV, $\phi_0$ rather than at its actual satellite zenith angle. Based on this assumption, both $R_{clr}(n,\phi_0)$ and $R_{cld}(n,\phi_0)$ are assumed to have the same respective values in each field of view. For simplicity, from now on we will omit the central satellite zenith angle term, $\phi_0$.

Combining ccronefov and ccrtwofov and eliminating $R_{cld}(n)$ one can solve for the cloud-cleared radiance term as a linear extrapolation of the radiances from the two cloudy fields of view as follows:

| Definition of cloud clearing symbols used in this chapter | |
|---|---|
| symbol | description |
| $^s$ | superscript $s$ refers to the step |
| $i$ | FOV index |
| $j$ | $\eta$ index |
| $J$ | number of $\eta_j$ |
| $k$ | $\zeta$ index |
| $n$ | channel index |
| $N_F$ | the number of FOV's within an AMSU footprint |
| $N_A$ | the number of FOV's within $\overline{R_n}$ |
| $\delta_{n,n'}$ | Kronecker delta function |
| $\eta_j$ | extrapolation parameters, determined w/o damping |
| $\tilde{\eta}_j$ | extrapolation parameters, determined w/ damping |
| $\delta\tilde{\eta}_j$ | error in $\eta$ with damping |
| $A_n^s$ | noise amplification factor |
| $R_{n,j}$ | observed radiance in FOV $j$ |
| $X_L^s$ | geophysical state $(T(p), q(p), O_3(p), \epsilon(n), \ldots)$ |
| $R_n(X_L^{s,i-1})$ | Radiance Computed from a geophysical state |
| $R(n)^{CCR}$ | clear column radiance |
| $R(n)^{EST}$ | clear radiance estimate |
| $\overline{R_n}$ | average of observed cloudy FOV's |
| $I_{n,n'}$ | instrument noise covariance |
| NE$\Delta$N | standard deviation of instrumental noise |
| $N_{n,n'}$ | error covariance of $(R(n)^{EST} - \overline{R_n})$ |
| $W_{n,n'}$ | inverse of error covariance of $(R(n)^{EST} - \overline{R_n})$ |
| $S_{n,j}$ | FOV contrast, $\overline{R_n} - R_{n,j}$ |
| $U_{j,k}$ | eigenvectors of $[(S_{j,n})^T W^s_{n,n'} S_{n,j}]$ |
| $\Lambda_{k,k}$ | eigenvalue matrix of $[(S_{j,n})^T W^s_{n,n'} S_{n,j}]$ |
| $\lambda_k$ | diagonal elements of $\Lambda_{k,k}$ |
| $\zeta_k^s$ | transformed extrapolation parameters |
| $\left(\delta\tilde{\zeta}_k \delta\tilde{\zeta}_k^T\right)^s$ | error covariance of solved components of $\zeta$ |
| $\left(\delta\hat{\zeta}_k \delta\hat{\zeta}_k^T\right)^s$ | error covariance of components of $\zeta$ not solved for |
| $\left(\delta\zeta_k \cdot \delta\zeta_k^T\right)^s$ | total error covariance of $\zeta$ |

$$R_{clr}(n) = R_1(n) + \frac{\alpha_1}{\alpha_2 - \alpha_1} \cdot (R_1(n) - R_2(n)) \tag{7.3}$$

This is done in two steps. We first use an estimate of the cloud clear radiance,$R_{clr}(n)^{EST}$ , to obtain the so called cloud-clearing parameter $\eta$, defined as:

$$\eta = \frac{\alpha_1}{\alpha_2 - \alpha_1} = \frac{R_{clr}(n)^{EST} - R_1(n)}{R_1(n) - R_2(n)} \tag{7.4}$$

The cloud-clearing term $\eta$ is channel independent and is used then in ccrtwofoveqn to solve for $R_{clr}(n)$ and cloud clear the entire spectrum.

While it is true that a single channel and 2 fields of view can be used to cloud clear the full

spectrum in the presence of one cloud, forthe case of K clouds a totla of K+1 fields of view and many channels must be used in a least squares sense to discriminate the clouds at different levels. Using the uniform scene assumption described above, Chahine (1977) showed that the reconstructed field of regard clear-column radiance for channel n, $R_{CCR}(n)$, can be written as a linear combination of the measured radiances in K+1 fields of view, according to:

$$R_{clr}(n) = R_1(n)+\eta_1\cdot[R_1(n)-R_{K+1}(n)]++...+\eta_l\cdot[R_1(n)-R_{(K+2)-l}(n)]+\eta_K\cdot[R_1(n)-R_2(n)] \quad (7.5)$$

where $\eta_K$ are unknown channel independent constants and K+1 fields of view are needed to solve for K cloud formations.

ccrmulfoveqn has been later replaced by a similar but more stable equation of the form:

$$R_{clr}(n) \equiv \overline{R_n} + \sum_{j=1}^{K} \left(\overline{R_n} - R_{n,j}\right) \cdot \eta_j \quad (7.6)$$

where $\overline{R_n}$ is called the extrapolation point and is an average of K FOV's defined by

$$\overline{R_n} \equiv \frac{1}{K} \sum_{j=1}^{K} R_{n,j} \quad (7.7)$$

Where $\overline{R_n}$ is the average radiance of all K fields of view. The expression in radclr, $\overline{R_n} - R_{n,j}$ is defined as *radiance contrast.*

As in Susskind et al. (1998), we determine the $\eta_j$values from observations in a selected set of $N_c$ cloud filtering channels which are primarily selected in between lines of the 15 micron CO2 band. If, for each channel n, one substitutes an estimated value,$R_{clr}(n)^{EST}$ , of the expected cloud-clear radiance for channel n, $R_{clr}(n)$ in radclr, this gives $N_c$ equations for K unknowns, of which only K-1 are linearly independent. Therefore, the solution for the K $\eta_j$ is given by a least square minimization whose parametrization is derived below. We can re-write the radiance contrast in matrix form as:

$$S_{n,j} \equiv \overline{R_n} - R_{n,j} \quad (7.8)$$

For nine FOVs the components of this matrix are given by:

$$S_{n,j} = \begin{pmatrix} \overline{R_1} - R_{1,9} & \overline{R_1} - R_{1,8} & \dots & \overline{R_1} - R_{1,1} \\ \overline{R_2} - R_{2,9} & \overline{R_2} - R_{2,8} & \dots & \overline{R_2} - R_{2,1} \\ \dots & \dots & \dots & \dots \\ \overline{R_N} - R_{N,9} & \overline{R_N} - R_{N,8} & \dots & \overline{R_N} - R_{N,1} \end{pmatrix} \quad (7.9)$$

The equation we need to solve can be written as:

$$R(n)^{EST} - \overline{R_n} = S_{n,j} \cdot \eta_j \quad (7.10)$$

The estimate of the clear radiances can be derived from

1. infrared radiances computed from an estimate of the clear atmosphere from a microwave physical retrieval, $R_n(X_L^{s,i-1})$

2. infrared radiances computed from an estimate of the clear atmosphere from a infrared/microwave physical retrieval which agrees with the microwave radiances,

3. infrared radiances computed from regression with microwave radiances.

We will apply a weight to the channels used in the least squares fit of this equation, $Wn, n'$, which is the inverse of an estimate of the covariance of $R(n)^{EST} - \overline{R_n}$. The error covariance is given by computational error estimates associated with $R(n)^{EST}$ derived from error estimates in the geophysical parameters, $Cn, n'$ (see Eqn. **??**) and instrumental noise, $I_{n,n'}$, associated with $\overline{R_n}$.

$$Wn, n' = \left( \frac{I_{n,n'}}{N_A} + C_{n,n'} \right)^{-1} \tag{7.11}$$

The computational covariance matrix, $C_{n,n'}$, is composed of a summation of all the radiance error estimates, $E^{s,i}_{n,g}$, for all geophysical parameters held constant during a retrieval:

$$C_{n,n'} \equiv \sum_g E^{s,i}_{n,g} \cdot \left( E^T_{g,n} \right)^{s,i} \tag{7.12}$$

The radiance error estimate, $E^{s,i}_{n,g}$, due to uncertainties in geophysical quantities is computed from error estimates in geophysical groups $X^{s,i}_{L,g}$ (*e.g.*, an entire temperature profile). As with the sensitivity functions, this can be thought of as an error estimate of a parameter, $\delta A_g$, and an associated function, $F^s_g(L)$. The partial derivatives are calculated from the current estimate of the geophysical state, $X^{s,i}_L$, and an estimate of the uncertainty in each geophysical group to be held constant in this stage of the retrieval, $\delta X^{s,i}_{L,g}$, and is calculated by a finite difference

for infrared channels (with additive functions)

$$E^{s,i}_{n,g} \equiv \delta A^{s,i}_j \cdot \left. \frac{\partial R_n \left( X^{s,i}_L + F_j \otimes \hat{A}_j \right)}{\partial A_j} \right|_{X^{s,i}_L} \tag{7.13}$$

$$\simeq \left( R_n \left( X^{s,i}_L + \delta X^{s,i}_{L,g} \otimes Q_g \right) - R_n \left( X^{s,i}_L \right) \right) \tag{7.14}$$

and for microwave channels

$$E^{s,i}_{n,g} \simeq \Theta_n \left( X^{s,i}_L + \delta X^{s,i}_{L,g} \otimes Q_g \right) - \Theta_n \left( X^{s,i}_L \right) \tag{7.15}$$

Since $\delta X_{L,g}$ is an RSS error estimate it can be correlated vertically and spectrally and correlated with respect to other parameters (*e.g.*, surface spectral emissivity error can be correlated with skin temperature). We use $Q_g$ as a scaling to compensate for assumed anti-correlation in these error estimated. Currently we set $Q_g$ to 0.5 for $T(p)$ and $q(p)$ error estimates and 1.0 for all other error estimates.

The instrument noise correlation matrix, $I_{n,n'}$, is given by

$$I_{n,n'} = \mathrm{NE\Delta N}_n \cdot \delta_{n,n'} \cdot \mathrm{NE\Delta N}_{n'} \tag{7.16}$$

where, the Kronecker delta function, $\delta_{n,n'}$

$$\begin{aligned} \delta_{n,n'} &= 1 \quad \text{if} \quad n = n' \\ &= 0 \quad \text{if} \quad n \neq n' \end{aligned} \tag{7.17}$$

For an apodized interferometer the correlation matrix and noise reduction factor for the apodization function would replace the Kronecker delta function (see Barnet *et. al*, 2000).

The iterative methodology to determine clear column radiances consists of four passes to determine $\eta_s$ (s = 1, 2, 3, 4), using four sets of conditions, described later, to compute $R_{clr}(n)$. At each iteration, both $R_{clr}(n)$ and $\eta_s$ become increasingly more accurate. Each set of conditions has its own covariance matrix , reflecting expected errors in $R_{clr}(n)$ and $R_j(n)$. The diagonal term of the noise covariance matrix is modeled according to:

$$\begin{aligned}(W^s_{n,n})^{-1} = (I_{n,n})^2 + [\frac{\partial R_n}{\partial T_{surf}}\delta T^s_{surf}]^2 + [\frac{\partial R_n}{\partial \epsilon_n}\delta \epsilon^s_n]^2 \\ +[\frac{\partial R_n}{\partial \rho_n}\delta \rho^s_n]^2 + [\frac{\partial R_n}{\partial T(p)}\delta T(p)^s]^2 \\ +[\frac{\partial R_n}{\frac{\partial q(p)}{q}}\frac{\delta q(p)^s}{q}]^2 + 0.1^2 \cdot (\frac{dB}{dT})^2_{\Theta_{n,clr}} \\ +{N'_{n,n}}^2(\frac{dB}{dT})^2_{Theta_{n,CLR}}\end{aligned} \tag{7.18}$$

where $I_{n,n'}$ is the channel i instrumental noise and the next 5 terms are contributions to errors in the computed value $R_{clr}(n)$ resulting from errors in estimated surface skin temperature, surface spectral emissivity, surface spectral bi-directional reflectance of solar radiation, and temperature and moisture profile respectively. Two additional sources of radiance uncertainty are included in the equation, representative of the physics error estimate, $N'_{n,n'}$ (see ahead), and an additional radiance uncertainty term. Both terms are in brightness temperature units. The off diagonal term of the noise covariance matrix is given by:

$$(W^s_{n,n'})^{-1} = [\frac{\partial R_n}{\partial T_{surf}}\frac{\partial R'_n}{\partial T_{surf}}\delta T^s_{surf}]^2 + [\frac{\partial R_n}{\partial \epsilon_n}\frac{\partial R'_n}{\partial \epsilon_{n'}}\delta\epsilon_n\delta\epsilon_{n'}] + ... \tag{7.19}$$

Multiplying both sides of Eqn. 7.10 with Eqn. 7.11 yields

$$W^s_{n,n} \cdot \left(R(n)^{EST} - \overline{R_n}\right) = W^s_{n,n} \cdot S_{n,j} \cdot \eta^s_j \tag{7.20}$$

then multiplying both sides by the transpose of the S-matrix yields

$$(S_{j,n})^T \cdot W^s_{n,n} \cdot \left(R(n)^{EST} - \overline{R_n}\right) = (S_{j,n})^T \cdot W^s_{n,n} \cdot S_{n,j} \cdot \eta^s_j \tag{7.21}$$

and the least squares determination of the extrapolation parameters would be

$$\eta^s_j = \left[(S_{j,n})^T \cdot W^s_{n,n} \cdot S_{n,j}\right]^{-1} \cdot (S_{j,n})^T \cdot W^s_{n,n} \cdot \left(R(n)^{EST} - \overline{R_n}\right) \tag{7.22}$$

In low signal-to-noise or clear scenes the signal-to-noise matrix, $\left[(S_{j,n})^T \cdot W^s_{n,n} \cdot S_{n,j}\right]$, can vanish and the solution would become unstable. In addition, we would like to determine the error covariance of the cloud clearing parameters, $\delta\eta'\delta\eta$, which, we will discover, is equal to the inverse of the signal-to-noise matrix. The error covariance is highly non-diagonal which makes both damping and noise determination difficult.

## 7.1 Selection of optimal fields of view

The effects of instrumental noise on the clear column radiances will generate in general be amplified from single spot noise because the clear column radiance are expressed as a linear combination of the observations in different fields of view. We can compute the *amplification* of the random noise that results from computing cloud cleared using Eqn. 7.3. let's take again the case of two FOVs. First we rewrite Eqn. 7.3 as

$$R_{clr}(n) = R_1(n)\,(1+\eta) - R_2(n)\cdot\eta \tag{7.23}$$

and note that the standard deviation of the error in $R_1$(n) and $R_2(n)$ are both given by NE$\Delta$N. The error in $R_{clr}$ is given by

$$\begin{aligned} \delta R^2_{clr}(n) &= \mathrm{NE}\Delta\mathrm{N}^2\cdot(1+\eta)^2 + \mathrm{NE}\Delta\mathrm{N}^2\cdot\eta^2 && (7.24)\\ &= \mathrm{NE}\Delta\mathrm{N}^2\cdot\left[(1+\eta)^2+\eta^2\right] && (7.25)\end{aligned}$$

therefore, the error has been "amplified" by

$$A = \sqrt{(1+\eta)^2+\eta^2} \tag{7.26}$$

Analogously, for the case of nine field of view, we have:

$$A \equiv [\sum_{j=1}^{9}(\frac{1}{9}\cdot(1+\sum_{j'=1}^{9}\eta_{j'}) - \eta_j)^2]^{1/2} \tag{7.27}$$

A is approximately equal to$[\sum_{j=1}^{9}\eta_j^2]^{1/2}$ because the first term, containing the factor 1/9, is small. It is desirable to find an accurate expression for clear column radiance which minimizes the amplification factor. We can do this by expressing equation 7.6 in terms of radiances in an optimal set of fields of view, given by linear combination of the original set. The matrix to be inverted can be transformed to a vector of eigenvalues, $\lambda_k$, with a unitary transformation matrix, $U_{j,k}$. The index $j$ denotes the parameters in transformed space versus $k$ for the untransformed parameters. This is equivalent to transforming the original $S_{n,j}$ matrix to an optimum linear combination of the original radiance differences, $S_{n,j}\cdot U_{j,k}$.

$$\Lambda_{k,k} \equiv (U_{k,j})^T\cdot(S_{j,n})^T\cdot W^s_{n,n}\cdot S_{n,j}\cdot U_{j,k} \tag{7.28}$$

when $\lambda_k$ are the diagonal elements of $\Lambda_{k,k}$.
Eigenvalues where $\lambda_k < \lambda_c$, where $\lambda_c$ is determined empirically, are NOT used in the solution. Removing low eigenvalues has the effect of reducing noise in the solution. The number of non-zero eigenvalues is an estimate of the number of cloud formations determined by the observed radiances and the signal-to-noise analysis. The linear combination associated with each eigenvalue represents is uncorrelated with the other eigenvalues. The total number of cloud formations, $N_\zeta$ can be computed from the total number of significant eigen-functions, defined by

$$\begin{aligned} \phi^s_k &= 1 \quad \text{if} \quad \lambda_k \geq \lambda_c \\ &= 0 \quad \text{if} \quad \lambda_k < \lambda_c && (7.29)\end{aligned}$$

$$N_{zeta} = \sum_{k=1}^{K} \phi_k^s \tag{7.30}$$

Eqn. 7.10 can then be written in transformed $\zeta$ space or un-transformed $\eta$ space as follows.

$$\begin{aligned} R(n)^{CCR} &= \overline{R_n} + (S_{n,j} \cdot U_{j,k}) \cdot \zeta_k^s & (7.31)\\ &= \overline{R_n} + S_{n,j} \cdot (U_{j,k} \cdot \zeta_k^s) = \overline{R_n} + S_{n,j} \cdot \tilde{\eta}_j^s & (7.32) \end{aligned}$$

Multiplying both sides of Eqn. 7.31 with Eqn. 7.11 yields

$$W_{n,n}^s \cdot \left(R(n)^{EST} - \overline{R_n}\right) = W_{n,n}^s \cdot (S_{n,j} \cdot U_{j,k}) \cdot \zeta_k^s \tag{7.33}$$

then multiplying both sides by the transpose of the *transformed* S-matrix yields

$$(U_{k,j})^T (S_{j,n})^T \cdot W_{n,n}^s \cdot \left(R(n)^{EST} - \overline{R_n}\right) = (U_{k,j})^T (S_{j,n})^T \cdot W_{n,n}^s \cdot U_{j,k} S_{n,j} \cdot \zeta_k^s \tag{7.34}$$

and the least squares determination of the extrapolation parameters would be

$$\zeta_k^s = \left[(U_{k,j})^T (S_{j,n})^T \cdot W_{n,n}^s \cdot S_{n,j} U_{j,k}\right]^{-1} \cdot (U_{k,j})^T (S_{j,n})^T \cdot W_{n,n}^s \cdot \left(R(n)^{EST} - \overline{R_n}\right) \tag{7.35}$$

however, the inverse can be replaced with Eqn. 7.28

$$\begin{aligned} \zeta_k^s &= [\Lambda_{k,k}]^{-1} \cdot (U_{k,j})^T (S_{j,n})^T \cdot W_{n,n}^s \cdot \left(R(n)^{EST} - \overline{R_n}\right) & (7.36)\\ &= \left[\frac{1}{\lambda_k}\right] \cdot (U_{k,j})^T (S_{j,n})^T \cdot W_{n,n}^s \cdot \left(R(n)^{EST} - \overline{R_n}\right) & (7.37) \end{aligned}$$

Eqn. 7.36 is exactly equal to the transform of Eqn. 7.22

$$\eta_j^s = U_{j,k} \zeta_k^s \tag{7.38}$$

however, we can now remove the $\zeta$'s associated with low eigenvectors.

$$\tilde{\zeta}_k^s = \frac{\phi_k^s}{\lambda_k} \cdot (U_{k,j})^T \cdot (S_{j,n})^T \cdot W_{n,n}^s \cdot \left(R(n)^{EST} - \overline{R_n}\right) \tag{7.39}$$

$$\tilde{\eta}_j^s \equiv U_{j,k} \cdot \tilde{\zeta}_k^s = U_{j,k} \cdot \frac{\phi_k^s}{\lambda_k} \cdot (U_{k,j})^T \cdot (S_{j,n})^T \cdot W_{n,n}^s \cdot \left(R(n)^{EST} - \overline{R_n}\right) \tag{7.40}$$

where $\tilde{\eta}_j^s$ is the extrapolation parameters from the damped least squares solution.

Discarding low eigenvalues reduces the noise amplification factor by suppressing noise in the solution for $\eta$, resulting in lower values of $\eta$. the values of $\eta_j^s$ are used in equation 7.6 to determine the cloud cleared radiance.

## 7.2 References

Barnet, C.D., J.M. Blaisdell and J. Susskind 2000. An analytical transformation for use in computation of interferometric spectra for remote sensing applications spectra. *IEEE Trans. Geosci. Remote Sens.* **38** p.169-183.

Chahine, M.T. 1982. Remote sensing of cloud parameters. J. Atmos. Sci. **39** p.159-170.

Chahine, M.T., H.H. Aumann and F.W. Taylor 1977. Remote sounding of cloudy atmospheres. III. Experimental verifications. J. Atmos. Sci. **34** p.758-765.

Chahine, M.T. 1977. Remote sounding of cloudy atmospheres. II. Multiple cloud formations. J. Atmos. Sci. **34** p.744-757.

Chahine, M.T. 1975. An analytic transformation for remote sensing of clear-column atmospheric temperature profiles. J. Atmos. Sci. **32** p.1946-1952.

Chahine, M.T. 1974. Remote sounding of cloudy atmospheres. I. The single cloud layer. J. Atmos. Sci. **31** p.233-243.

Coakley, J.A. and F.P. Bretherton 1982. Cloud cover from high-resolution scanner data: detecting and allowing for partially filled fields of view. J. Geophys. Res. **87** p.4917-4932.

McMillin, L.M. and C. Dean 1982. Evaluation of a new operational technique for producing clear radiances. J. Appl. Meteor. **21** p.1005- 1014.

Press, W.H., Flannery, B.P., Teukolsky, S.A., Vetterling 1986. W.T., Numerical recipes: The art of scientific computing. Cambridge University Press, 818 pgs.

Rodgers, C.D. 1970. Remote sensing of the atmospheric temperature profile in the presence of cloud. Quart. J. Roy. Meteor. Soc. **96** p.654-666.

Smith, W.L., X.L. Ma, S.A. Ackerman, H.E. Revercomb and R.O. Knuteson 1992. Remote sensing cloud properties from high spectral resolution infrared observations. J. Atmos. Sci. **50** p.1708-1720.

Smith, W.L. 1968. An improved method for calculating tropospheric temperature and moisture from satellite radiometer measurements. Monthly Weather Review **96** p.387-396.

Soden, B.J. and F.P. Bretherton 1993. Upper tropospheric relative humidity from the GOES 6.7 um channel: method and climatology for July 1987. J. Geophys. Res. **98** p.16669-16688.

Susskind, J., C.D. Barnet and J.M. Blaisdell 2003. Retrieval of atmospheric and surface parameters from AIRS/AMSU/HSB data in the presence of clouds. IEEE Trans. Geosci. Remote Sens. v.41 p.390-40.

Susskind, J., C.D. Barnet and J. Blaisdell 1998. Determination of atmospheric and surface parameters from simulated AIRS/AMSU sounding data: Retrieval methodology and cloud clearing methodology. Adv. Space Res. **21** p.369-384.

Swaroop, A., A.J. Nappi, H.J. Bloom and L.M. McMillin 1988. A method of noise reduction for the improvement of clear column radiance estimation in partly cloudy areas. in 3rd Conf. Sat. Meteor. & Oceanography p.13- 15.

# Chapter 8

# Description of the Core Retrieval Algorithm
# Step V: The physical retrieval algorithm

## 8.1 Introduction to the inverse problem

The retrieval of geophysical quantities, such as the atmospheric water, from satellite radiances is highly non-linear, requiring inversion of the equations of the form

$$R_n(X) \simeq \int_{\nu} \Phi_\nu \int_{p} B(T(p)) \cdot \frac{\partial \exp\left( - \int_{z'=\infty}^{z(p)} \sum_i \kappa_i(X, \ldots) dz' \right)}{\partial p} \cdot dp \cdot d\nu \tag{8.1}$$

One should always remember that Eqn. 8.1 is an approximation and that the real radiative transfer equation has non-linear components resulting from

a) the temperature dependence of the transmittance,

b) the non-linearity of the Planck function,

c) the down-welling component of the radiative transfer equation.

Brightness temperature, $\Theta_n$, is usually more linear with temperature (our core product), provides improved numerically stability, and is a convenient way to display multi-spectral radiance information.

$$\Theta_n \equiv B_{\nu_0}^{-1}(R_n) = \frac{\alpha_2 \cdot \nu_0}{\log_e \left[ 1 + \frac{\alpha_1 \nu_0^3}{R_n} \right]} \tag{8.2}$$

Usually, only radiance differences, *e.g.* observations minus computed, are needed in remote sounding so that a radiance difference, $\Delta R_n$, can be converted to a brightness temperature difference, $\Delta\Theta_n$, as follows

$$\Delta\Theta_n \simeq \Delta R_n \cdot \left( \frac{\partial B_\nu}{\partial T}\Big|_{B_\nu^{-1}(R_n(X_L^{s,i-1}))} \right)^{-1} \tag{8.3}$$

The first step to retrieving the atmospheric state is the linearization of the radiative transfer equation.

## 8.2 Linearization of the radiative transfer equation

The idea is to do a Taylor expansion integrand about a reference state, $X_0$.

For a temperature retrieval this is accomplished by first linearizing the Planck function a the reference temperature profile as follows:

$$T(z) \equiv T^0(z) + \Delta T(z) \tag{8.4}$$

so that

$$B_\nu(T(z)) = B_\nu(T^0(z)) + \frac{\partial B_\nu(T^0(z))}{\partial T}\Big|_{T^0(z)} \Delta T(z) \tag{8.5}$$

In general, the radiance of the reference state, $X_0$, can be computed. In our example, we will consider only the atmospheric component of the radiative transfer equation:

$$R_\nu^0 = \int_{z=0}^{\infty} B_\nu(T^0(z)) \cdot \frac{\partial \tau_\nu(X_0)}{\partial z} \partial z \tag{8.6}$$

Everything is known within this equation except the temperature profile correction, $\Delta T(z)$. If we insert Eqn. 8.5 into Eqn. 8.6 we get

$$\Delta R_\nu = R_\nu - R_\nu^0 = \int_{z=0}^{\infty} \left( B_\nu(T^0(z)) + \frac{\partial B_\nu(T^0(z))}{\partial T}\Big|_{T^0(z)} \Delta T(z) \right) \cdot \frac{\partial \tau_\nu}{\partial z} \partial z \quad - \quad R_\nu^0 \tag{8.7}$$

which can be simplified

$$\Delta R_\nu = \int_{z=0}^{\infty} \left( \frac{\partial B_\nu(T^0(z))}{\partial T}\Big|_{T^0(z)} \cdot \frac{\partial \tau_\nu}{\partial z} \right) \Delta T(z) \partial z \tag{8.8}$$

If we define a *kernel* function as

$$K(z,\nu) \equiv \frac{\partial B_\nu(T^0(z))}{\partial T}\Big|_{T^0(z)} \frac{\partial \tau_\nu}{\partial z} \tag{8.9}$$

then we can write the linearized radiance transfer equation as

$$\Delta R_\nu = \int_{z=0}^{\infty} K(z,\nu) \cdot \Delta T(z) \partial z \tag{8.10}$$

Thus, we will ignore the frequency dependence of the Planck function and we will ignore the temperature dependence of the transmittance. Note that for un-apodized interferometers and broad

band instruments this expansion is not justified. For broad band channels (*e.g.*, 10's of $\mathrm{cm}^{-1}$, like MODIS, HIRS, etc.) an effective Planck function can be computed by integration over the band pass. For an un-apodized interferometer the side-lobes are significant for 100's of $\mathrm{cm}^{-1}$. The linearization of the integrand is one of the principal reasons for use of apodized interferometer spectra.

Equation 8.10 can be approximated by a numerical integral which has the advantage of being solved by matrix inversion.

$$\Delta R_n \approx \sum_{L=1}^{N_L} (\Delta z(L) \cdot K(n,L)) \cdot \Delta T(L) = \tilde{K}_{n,L} \cdot \Delta T(L) \tag{8.11}$$

The thickness of the layer for the finite difference form is usually absorbed into the definition of $K$, written as $\tilde{K}$ above.

As an example, For $N_\nu = 3$ and $N_z = 4$ the matrix would look like:

$$\begin{bmatrix} \Delta R(\nu(1)) \\ \Delta R(\nu(2)) \\ \Delta R(\nu(3)) \end{bmatrix} = \Delta z \cdot \begin{bmatrix} K(z(1),\nu(1)) & K(z(2),\nu(1)) & K(z(3),\nu(1)) & K(z(4),\nu(1)) \\ K(z(1),\nu(2)) & K(z(2),\nu(2)) & K(z(3),\nu(2)) & K(z(4),\nu(2)) \\ K(z(1),\nu(3)) & K(z(2),\nu(3)) & K(z(3),\nu(3)) & K(z(4),\nu(3)) \end{bmatrix} \cdot \begin{bmatrix} \Delta T(z(1)) \\ \Delta T(z(2)) \\ \Delta T(z(3)) \\ \Delta T(z(4)) \end{bmatrix} \tag{8.12}$$

which can be written in matrix form as (we include the $\Delta z$ component in the matrix $K_{n,L}$:

$$\Delta R_n = K_{n,L} \cdot \Delta T_L \tag{8.13}$$

If $N_\nu$ is greater than $N_z$ then there are more equations than unknowns and an inverse for $K_{n,L}$ exists, $K^{-1}_{L,n}$, then the correction to the initial temperature profile can be found as follows:

$$K^{-1}_{L,n} \cdot \Delta R_n = K^{-1}_{L,n} \cdot K_{n,L} \Delta T_L = \Delta T_L \tag{8.14}$$

$$\Delta T_L = K^{-1}_{L,n} \cdot \Delta R_n = \left[K^T_{L,n} \cdot K_{n,L}\right]^{-1} \cdot K^T_{L,n} \cdot \Delta R_n \tag{8.15}$$

where we employ the definition of a an inverse of a non-square matrix to find the expression for $K^{-1}$ as follows

$$\begin{aligned} K_{n,L} \cdot K^{-1}_{L,n} &= I_{n,n} && (8.16)\\ K^T_{L,n} \cdot \left(K_{n,L} \cdot K^{-1}_{L,n}\right) &= K^T_{L,n} \cdot I_{n,n} && (8.17)\\ \left(K^T_{L,n} \cdot K_{n,L}\right) \cdot K^{-1}_{L,n} &= K^T_{L,n} && (8.18)\\ K^{-1}_{L,n} &= \left(K^T_{L,n} \cdot K_{n,L}\right)^{-1} \cdot K^T_{L,n} && (8.19) \end{aligned}$$

Unfortunately, $N_\nu$ is usually much smaller than $N_z$. This is because the kernel functions tend to overlap and, therefore, are not independent. This is a condition generally referred to as *information redundancy* which makes the inversion equation ill-posed. Least squares techniques need to be applied and the solution for $\Delta T$ can be found by iterative techniques.

before going any further let's generalize the above expression as it follows. Using the notation of the generalized sensitivity matrix, $S_{n,L}$, in place of the traditional kernel function, $K_{n,L}$ the unconstrained expression we wish to solve has the form of

$$\Delta R_n = R_n - f(X_L) = S_{n,L} \cdot \Delta X_L \tag{8.20}$$

The inverse solution is given by:

$$\Delta X_L = S_{L,n}^{-1} \cdot \Delta R_n \tag{8.21}$$

Again, from the definition of an inverse

$$\begin{aligned} S_{n,L} \cdot S_{L,n}^{-1} &= I_{n,n} && (8.22)\\ S_{L,n}^T \cdot \left(S_{n,L} \cdot S_{L,n}^{-1}\right) &= S_{L,n}^T \cdot I_{n,n} && (8.23)\\ \left(S_{L,n}^T \cdot S_{n,L}\right) \cdot S_{L,n}^{-1} &= S_{L,n}^T && (8.24) \end{aligned}$$

therefore, for a non-square matrix, $S_{n,L}$, the inverse is given by

$$S_{j,n}^{-1} = \left[S_{L,n}^T \cdot S_{n,L}\right]^{-1} S_{L,n}^T \tag{8.25}$$

So that Eqn. 8.21 becomes

$$\Delta X_L = \left[S_{L,n}^T \cdot S_{n,L}\right]^{-1} \cdot S_{L,n}^T \cdot \Delta R_n \tag{8.26}$$

In addition to the redundancy problem, $_n$ has a large fraction of noise (due to low signal-to-noise related to the low temperatures) which makes the solution unstable. Careful attention must be given to the select channels containing the maximum amount of unique information fromthe spectra and with the lowest instrumental noise. See ahead the section on the channel selection methodology. To take into account the noise problem, we can compute a weighted least squares solution:

$$\Delta X_L = \left[S_{L,n}^T \cdot W_{n,n} \cdot S_{n,L}\right]^{-1} \cdot S_{L,n}^T \cdot W_{n,n} \cdot \Delta R_n \tag{8.27}$$

Another critical problem is represented by the fact that the kernel functions $S_{n,L}$ are very broad functions and, therefore, are insensitive to high frequency oscillations in $\Delta X_L$. As a result, the inversion process usually converges with unrealistic vertical profiles.

In the most crude sense, regularization is the stabilization of the inverse by adding something to the matrix to avoid an in-determinant solution (*i.e.*, a zero divided by zero). This, in effect, will dampen the solution, $\Delta X_L$, and make it "stick" to the previous iteration. This results in a need for a *background* term, $\Psi_n$, if we are going to iterate the solution.

$$\Delta X_L = \left[S_{L,n}^T \cdot W_{n,n} \cdot S_{n,L} \quad + \quad H_{L,L}\right]^{-1} \cdot S_{L,n}^T \cdot W_{n,n} \cdot (\Delta R_n - \Phi_n) \tag{8.28}$$

## 8.3 The physical retrieval algorithm

The atmospheric state, $X_L^s$, and the error estimate of that state, $\delta X_L^s$, are used to minimize the residuals in observed minus computed radiances in each retrieval step=$s$.

The current AIRS/AMSU-A/HSB retrieval system is a modular set of retrieval steps. Each retrieval step solves for certain parameters while holding all others constant. The geophysical state of the clear atmosphere, $X_L^{s,i}$, at a given retrieval step, $s$, and iteration, $i$, is given in Table 8.1.

Table 8.1: Definition of the geophysical state, $X_L^{s,i}$, in the AIRS science team physical algorithm

| | |
|---|---|
| $T(p)$ | vertical temperature profile |
| $q(p)$ | vertical water vapor profile (7.7 g/kg @ surface) |
| $L(p)$ | vertical liquid water profile |
| $O_3(p)$ | vertical ozone profile (0.4 ppmv, 8ppmv @ 6 mb)) |
| $T_s$ | surface temperature |
| $\epsilon(\nu)$ | spectral surface emissivity |
| $\rho_{\odot}(\nu)$ | spectral surface reflectivity of solar radiation |
| $CO_2(p)$ | carbon dioxide profile |
| $CH_4(p)$ | methane profile |
| $CO(p)$ | carbon monoxide profile |
| $N_2O(p)$ | nitrogen oxide profile |
| $SO_2(p)$ | sulfur dioxide profile |
| $HNO_3$ | nitric acid profile |

Each step solves for specific geophysical parameters while holding others constant. The parameters considered as error sources in the error covariance matrix are shown in the table. Some parameters are not accurately known and, therefore, they are only considered on the diagonal of the error covariance matrix. These are shown with a dagger symbol, †.

Each step uses its own subset of channels. If the error covariance matrix is large for a given channel or it has large spectroscopic uncertainties then it is permanently removed from the computation. This has obvious improvements for execution time and it also improves results, since error estimates and damping are the least accurate components of the retrieval process.

The clear column radiance is calculated from the $N_F$ FOV's using the equation:

$$R(n)^{CCR} = \overline{R_n} + \sum_{j=1}^{N_F} \left( \overline{R_n} - R_{n,N_F+1-j} \right) \cdot \tilde{\eta}_j^{s,i} \tag{8.29}$$

It is possible for the cloud cleared radiance observations to be close to zero or even negative due to instrumental noise and cloud clearing errors. Therefore, we never attempt to compute a clear column brightness temperature from these radiances.

The retrieval algorithm minimizes the weighted difference between the clear column radiance observations, $R(n)^{CCR}$, and radiances computed using a forward model, $R_n\left(X_N^{s,i}\right)$, by varying the geophysical state, $X_L^{s,i}$, where $i$ is the iteration number within the current retrieval step, $s$. The forward model at iteration $i = 1$ uses the previous iteration's retrieved geophysical state, $X_L^{s,i}$. For $s = 1, i = 1$, $X_L^{1,1}$ comes from a first guess (climatology) and for $s > 1, i = 1$ the retrieval uses the result from the last iteration, $I + 1$, from the previous step as a first guess, $X_L^{s,1} = X_L^{s-1,I+1}$.

For multi-spectral retrievals the radiances can vary many orders of magnitude over the spectral regions (*e.g.*, microwave, long-wave infrared, and short-wave infrared). To maintain numerical precision it is desirable to normalize the "obs-calc" (O-C). We would like to mimic a brightness temperature difference and we can approximate this by

For infrared channels we compute O-C as given by8.30:

Table 8.2: Retrieval Steps in NUCAPS v1.0 Algorithm

| $s$ | solve for: | step name | computational error sources in error covariance | channels used AIRS | ATMS |
|---|---|---|---|---|---|
| 1 | $T(p), \epsilon(\nu), T_s$ | MIT | $q(p), L(p)$ | | 12 |
| 2 | $q(p), L(p)$ | MIT | $T^{\dagger}(p), T_s, \epsilon(\nu), \rho_{\odot}(\nu)$ | | 3 |
| 3 | $T(p), \epsilon(50.3), T_s$ | AMSU(Ts) | $q(p), L(p)$ | | 11 |
| 4 | $P_{cld}(i), \alpha_{cld}(i)$ | ETA | $T^{\dagger}(p), q^{\dagger}(p), T_s, \epsilon(\nu), \rho_{\odot}(\nu)$ | $\leq 58$ | |
| 5 | $R_{ccr}$ | ETA | $T^{\dagger}(p), q^{\dagger}(p), T_s, \epsilon(\nu), \rho_{\odot}(\nu)$ | $\leq 58$ | |
| 6 | $T(p), q(p), O_3(p)$ | RT_NOAA | | 1680 | |
| 7 | $T_s, \epsilon(\nu), \rho_{\odot}(\nu)$ | RT_NOAA | | 1680 | |
| 8 | $T(p), \epsilon(50.3), T_s$ | AMSU(Ts) | $R_{ccr}(\nu), q(p), L(p)$ | | 11 |
| 9 | $P_{cld}(i), \alpha_{cld}(i)$ | ETA | $T^{\dagger}(p), q^{\dagger}(p), T_s, \epsilon(\nu), \rho_{\odot}(\nu)$ | $\leq 58$ | |
| 10 | $R_{ccr}$ | ETA | $T^{\dagger}(p), q^{\dagger}(p), T_s, \epsilon(\nu), \rho_{\odot}(\nu)$ | $\leq 58$ | |
| 11 | $T_s, \epsilon(\nu).\rho_{\odot}(\nu), \overline{q}$ | SURFACE | $T^{\dagger}(p)$ | 25 | |
| 12 | $T(p)$ | TEMP | $R_{ccr}(\nu), q(p), O_3(p), L(p), T_s,$ $\epsilon(\nu), \rho_{\odot}(\nu)$, $CO_2$ | 108 | 7 |
| 13 | $q(p)$ | WATER | $R_{ccr}(\nu), T^{\dagger}(p), L(p), T_s,$ $\epsilon_{mw}(f), \rho_{\odot}(\nu)$, $CH_4$(p) | 44 | 3 |
| 14 | $O_3(p)$ | OZONE | $R_{ccr}(\nu), q(p), T_s, \epsilon(\nu)$ | 34 | |
| 15 | $((T(p), \epsilon(50.3)))$ | AMSU(RJ) | $R_{ccr}(\nu), q(p), L(p), T_s$ | | 11 |
| 16 | $P_{cld}(i), \alpha_{cld}(i)$ | ETA | $T^{\dagger}(p), q^{\dagger}(p), T_s, \epsilon(\nu), \rho_{\odot}(\nu)$ | $\leq 58$ | |
| 17 | $R_{ccr}$ | ETA | $T^{\dagger}(p), q^{\dagger}(p), T_s, \epsilon(\nu), \rho_{\odot}(\nu)$ | $\leq 58$ | |
| 18 | $T_s, \epsilon(\nu), \rho_{\odot}(\nu)$ | SURFACE | $R_{ccr}(\nu), T^{\dagger}(p), q^{\dagger}(p)$ | 25 | |
| 19 | $T(p)$ | TEMP | $R_{ccr}(\nu), q(p), O_3(p), L(p), T_s,$ $\epsilon(\nu), \rho_{\odot}(\nu)$, $CO_2$ | 124 | 7 |
| 20 | $CO(p)$ | CO | $R_{ccr}(\nu), T(p), q(p), T_s$ | 36 | |
| 21 | $CH_4(p)$ | CH4 | $R_{ccr}(\nu), T(p), q(p), T_s$ | 71 | |
| 22 | $CO_2$ | CO2 | $R_{ccr}(\nu), T(p), q(p), T_s$ $O_3$, $\rho_{\odot}(\nu)$ | 70 | |
| 23 | $HNO_3(p)$ | HNO3 | $R_{ccr}(\nu), T(p), q(p), T_s$ | 8 | |
| 24 | $N_2O(p)$ | N2O | $R_{ccr}(\nu), T(p), q(p), T_s$ | 52 | |
| 25 | $SO_2(p)$ | SO2 | $R_{ccr}(\nu), T(p), q(p), T_s$ | 63 | |
| | † indicated that off-diagonal elements are not used | | | | |

$$\Delta\Theta_n^{s,i} \equiv \left(R(n)^{CCR} - R_n\left(X_N^{s,i}\right)\right) \cdot \left(\left.\frac{\partial B_\nu}{\partial T}\right|_{B_\nu^{-1}(R_n\left(X_N^{s,i}\right))}\right)^{-1} \tag{8.30}$$

while for microwave channels, where the data is given in brightness temperature, we compute a brightness temperature difference

$$\Delta\Theta_n^{s,i} \equiv \left(\Theta_{n,CCR} - \Theta_n\left(X_L^{s,i}\right)\right) \tag{8.31}$$

where $\Theta_{n,CCR}$ is either the observed microwave brightness temperatures or the average of the 9 brightness temperatures within the ATMS field of regard.

## 8.4 Specification of Geophysical Functions

A change to a group of the geophysical state are represented by a geophysical perturbation parameters, $\Delta A_j^{s,i}$, and an associated perturbation function, $F_{L,j}^s$. This is the generalized sensitivity matrix. For vertical profiles, such as $T(p), q(p), O_3(p)$, the perturbation function, $F_{L,j}^s = F_j^s(p)$, is a trapezoid (with dimensionless maximum value of 1.0) covering a vertical range of layers. For spectral parameters such as $\epsilon(n)$ and $\rho(n)$, $F_{L,j}^s = F_j^s(\nu)$ is a wedge or triangle covering a range of frequencies with a dimensionless peak value of 1.0. For surface temperature and microwave emissivity $F_{L,j}^s$ is a value equal to unity. These are summarized in the following table:.

Table 8.3: Scale size of perturbation functions in v5.0

| retrieval | $\Delta\hat{A}_j^s$ | | | | | |
|---|---|---|---|---|---|---|
| step | $T_s$ | $\epsilon(\nu)$ | $\rho(\nu)$ | $T(p)$ | $q(p)$ | trace |
| RETAMSU | 1K | 1% | | 1K | | |
| RETSURF | 3K | 1% | 0.5% | 3K | 20% | |
| RETTMP | | | | 1K | | |
| RETWATR | | | | | 10% | |
| RETOZON | | | | | | 10% |
| RET_CO | | | | | | 10% |
| RET_CH4 | | | | | | 2% |
| RET_CO2 | | | | | | 1% |
| RET_HNO3 | | | | | | 20% |
| RET_N2O | | | | | | 5% |
| RET_SO2 | | | | | | 50% |

- Temperature functions are additive vertical trapezoids.

$$T^{s,i+1}(p) = T^{s,i}(p) + \sum_j F_j^s(p) \cdot \Delta A_j^{s,i+1} \tag{8.32}$$

$$T_s^{s,i+1} = T_s^{s,i} + F_j^s \cdot \Delta A_j^{s,i+1} \tag{8.33}$$

- Composition functions are multiplicative vertical trapezoids.
  - Radiance kernel is $\propto \exp(\kappa(X_L^{s,i}))$,
  - $\kappa(X_L^{s,i})$, is the optical depth $\propto X_L^{s,i}$.
  - Therefore, composition variables are more linear in $\ln\left(X_L^{s,i}\right)$
  - $\partial \ln(X_L^{s,i}) \propto \frac{\partial X_L^{s,i}}{X_L^{s,i}}$ which is a % change in $X_L^{s,i}$.

$$q^{s,i+1}(p) = q^{s,i}(p) \cdot \left[1 + \sum_j F_j^s(p) \cdot \Delta A_j^{s,i+1}\right] \tag{8.34}$$

- Emissivity functions are additive spectral triangles.

$$\epsilon^{s,i+1}(n) = \epsilon^{s,i}(n) + \sum_j F_j^s(\nu) \cdot \Delta A_j^{s,i+1} \tag{8.35}$$

- A scaling parameter $\hat{A}_j^s$ is used to create dimensionless parameters and adjust scale between different functional groups (*e.g.*, when mixing T(p), q(p), and emissivity in one retrieval).
- The Jacobian, $K_{n,L}^{s,i}$, becomes a set of new derivatives, $S_{n,j}^{s,i}$, in which groups of parameters in $L$ space are grouped together in $J$ space.
- Sub-sets (*e.g.*, temperature) of vertical and spectral functions must sum to unity: $\sum_j \left(F_{L,j}^s\right) = 1$ for a group of functions.

We will write the entire geophysical state as a vector $X_L$, with associated geophysical perturbation functions $\Delta X_{L,j} = F_{L,j}^s \otimes \Delta \hat{A}_j^s$ and perturbation parameters $\Delta A_j^{s,i}$. The $\otimes$ symbol represents a scale factor for $F_{L,j}^s$ and not a matrix multiply and is equivalent to an identity matrix multiplication, $F_{L,j}^s \otimes \Delta \hat{A}_j^s \equiv F_{L,j}^s \cdot I_{j,j} \cdot \Delta \hat{A}_j^s$. For vertical functions the index $L$ will specify pressure intervals while for spectral parameters the functions will represent frequency intervals and $L$ will specify the channel numbers, $n$. For other functions, such as skin temperature the function is a value that is, the index $L$ is single valued, and there is only one value of $j$.

$$X_L^{s,i+1} = X_L^{s,i} + \sum_j \left(F_{L,j}^s \otimes \Delta \hat{A}_j^s\right) \cdot \Delta A_j^{s,i+1} \tag{8.36}$$

The sensitivity matrix, $S_{n,j}^{s,i}$, is calculated for each channel $n$ and each geophysical parameter, denoted by index $j$, to be solved for in the current retrieval step, $s$, and iteration, $i$. The sensitivity matrix is computed for a pre-set perturbation functions, $F_{L,j}^s \otimes \Delta \hat{A}_j^s$ as follows

- For additive functions the S-matrix is given by

for infrared channels

$$S_{n,j}^{s,i} \equiv \Delta \hat{A}_j^s \cdot \left.\frac{\partial R_n\left(X + F_{L,j}^s \cdot A_j\right)}{\partial A_j}\right|_{X_L^{s,i}} \cdot \left(\left.\frac{\partial B_\nu}{\partial T}\right|_{B_\nu^{-1}(R_n\left(X_N^{s,i}\right))}\right)^{-1} \tag{8.37}$$

$$\simeq \left(R_n\left(X_L^{s,i} + F_{L,j}^s \cdot \Delta \hat{A}_j^s\right) - R_n\left(X_N^{s,i}\right)\right) \cdot \left(\left.\frac{\partial B_\nu}{\partial T}\right|_{B_\nu^{-1}(R_n\left(X_N^{s,i}\right))}\right)^{-1} \tag{8.38}$$

and for microwave channels

$$S_{n,j}^{s,i} \simeq \Theta_n\left(X_L^{s,i} + F_{L,j}^s \cdot \Delta \hat{A}_j^s\right) - \Theta_n\left(X_L^{s,i}\right) \tag{8.39}$$

- For multiplicative functions the S-matrix is given by

$$S_{n,j}^{s,i} \equiv \Delta\hat{A}_j^s \cdot \left.\frac{\partial R_n\left(X \cdot \left(1 + F_{L,j}^s \cdot A_j\right)\right)}{\partial A_j}\right|_{X_L^{s,i}} \cdot \left(\left.\frac{\partial B_\nu}{\partial T}\right|_{B_\nu^{-1}\left(R_n\left(X_N^{s,i}\right)\right)}\right)^{-1} \quad (8.40)$$

$$\simeq \left(R_n\left(X_L^{s,i} \cdot \left(1 + F_{L,j}^s \cdot \Delta\hat{A}_j^s\right)\right) - R_n\left(X_N^{s,i}\right)\right) \cdot \left(\left.\frac{\partial B_\nu}{\partial T}\right|_{B_\nu^{-1}\left(R_n\left(X_N^{s,i}\right)\right)}\right)^{-1} \quad (8.41)$$

and for microwave channels

$$S_{n,j}^{s,i} \simeq \Theta_n\left(X_L^{s,i} \cdot \left(1 + F_{L,j}^s \cdot \Delta\hat{A}_j^s\right)\right) - \Theta_n\left(X_L^{s,i}\right) \quad (8.42)$$

- Analytic derivatives on the RT grid do not help our algorithm, $\delta$ function perturbations are sub-optimal (Backus+Gilbert).
- Single sided finite difference is currently used, we will explore the benefit of double-sided and dynamically scaled derivatives someday. This is not our biggest error source!!!

## 8.5 Retrieval Error Covariance Matrix

The error covariance matrix, $N_{n,n'}^s$, is computed in the first iteration of every step and is the estimate of the uncertainty in the observed minus computed effective brightness temperature difference, $\Delta\Theta_n^{s,i}$. It consists of the clear column radiance error estimate, discussed earlier (Eqn. **??**) and computation uncertainties in the forward calculation of $R_n\left(X_N^{s,i}\right)$. The computational uncertainty is calculated for all geophysical parameters, $X$, not modified by the retrieval and, therefore, assumed known in a given step of the retrieval process.

The radiance error estimate, $E_{n,g}^{s,i}$, due to uncertainties in geophysical quantities is computed from error estimates in geophysical groups $X_{L,g}^{s,i}$ (*e.g.*, an entire temperature profile). As with the sensitivity functions, this can be thought of as an error estimate of a parameter, $\delta A_g$, and an associated function, $F_g^s(L)$. The partial derivatives are calculated from the current estimate of the geophysical state, $X_L^{s,i}$, and an estimate of the uncertainty in each geophysical group to be held constant in this stage of the retrieval, $\delta X_{L,g}^{s,i}$, and is calculated by a finite difference

For infrared channels the error estimate is converted to effective brightness temperature units using

$$E_{n,g}^{s,i} \equiv \delta A_j^{s,i} \cdot \left.\frac{\partial R_n\left(X_L^{s,i}\right)}{\partial A_j}\right|_{X_L^{s,i}} \cdot \left(\left.\frac{\partial B_\nu}{\partial T}\right|_{B_\nu^{-1}\left(R_n\left(X_N^{s,i}\right)\right)}\right)^{-1} \quad (8.43)$$

$$\simeq \left(R_n\left(X_L^{s,i} + \delta X_{L,g}^{s,i} \otimes Q_g\right) - R_n\left(X_L^{s,i}\right)\right) \cdot \left(\left.\frac{\partial B_\nu}{\partial T}\right|_{B_\nu^{-1}\left(R_n\left(X_N^{s,i}\right)\right)}\right)^{-1} \quad (8.44)$$

and for microwave channels the computation is

$$E_{n,g}^{s,i} \simeq \Theta_n \left( X_L^{s,i} + \delta X_{L,g}^{s,i} \otimes Q_g \right) - \Theta_n \left( X_L^{s,i} \right) \tag{8.45}$$

Since $\delta X_{L,g}$ is an RSS error estimate it can be correlated vertically and spectrally and correlated with respect to other parameters (*e.g.*, surface spectral emissivity error can be correlated with skin temperature). We use $Q_g$ as a scaling to compensate for assumed anti-correlation in these error estimated. Currently we set $Q_g$ to 0.5 for $T(p)$ and $q(p)$ error estimates and 1.0 for all other error estimates.

The computational covariance matrix, $C_{n,n'}^{s,i}$, is composed of a summation of all the radiance error estimate for all geophysical parameters held constant during a retrieval

$$C_{n,n'}^{s,i} \equiv \sum_g E_{n,g}^{s,i} \cdot \left( E_{g,n}^T \right)^{s,i} \tag{8.46}$$

The retrieval error covariance matrix is a combination of the cloud cleared radiance error covariance and the computational error covariance terms.

$$N_{n,n'}^{s,i} = C_{n,n'}^{s} \quad + \quad \frac{\left[ \delta R(n)^{CCR} \cdot \left( \delta R_{n',OBS} \right)^T \quad + \quad \delta R_n^U \cdot \delta_{n,n'} \cdot \left( \delta R_{n'}^U \right)^T \right]}{\left( \frac{\partial B_\nu}{\partial T} \Big|_{B_\nu^{-1}(R_n(X_N^{s,i}))} \right) \cdot \left( \frac{\partial B_\nu}{\partial T} \Big|_{B_\nu^{-1}(R_{n'}(X_L^{s,i}))} \right)} \tag{8.47}$$

Where $\delta R_n^U$ is a small term for additional unknown sources of error which is presently computed from

$$\delta R_n^U \equiv 0.1^\circ \cdot \left( \frac{\partial B_\nu}{\partial T} \Big|_{B_\nu^{-1}(R_n(X_N^{s,i}))} \right)^{-1} \tag{8.48}$$

In retrieval code the cloud cleared radiance error estimates are computed in the routine noisecv.F and the computation terms are computed and added to the noise covariance matrix in the individual retrieval routines (*e.g.*, rettmpc.F, retwatr.F, etc.)

## 8.6 The retrieval of the geophysical state

The brightness temperature difference residuals can be written in terms of a linear Taylor expansion change to the geophysical parameters, $\Delta A_j^{s,i}$, which is dimensionless due to $\Delta \hat{A}_j^s$ in Eqn. 8.37 or Eqn. 8.40. In any given retrieval step, we separate the parameters we are solving for into the matrix $S_{n,j}^{s,i}$ and the parameters we are not solving for into the matrix $E_{n,g}^{s,i}$. If we assume for the moment that the value of the parameters we are not solving for are known, such that $E_{n,g}^{s,i}$ could be known we could write

$$\Delta\Theta_n^{s,i} = S_{n,j}^{s,i} \cdot \Delta A_j^{s,i+1} + \sum_g \pm E_{n,g}^{s,i} \tag{8.49}$$

But we do not know the sign of the errors in the parameters we are not solving for, if we did we could eliminate that uncertainty. At best we only have an estimate for the covariance and spectral

correlation of these uncertainties, therefore, $\sum_g \pm E^{s,i}_{n,g}$ enters into the error covariance matrix via Eqn. 8.46 and Eqn. 8.47 so that the radiance residuals, $\Delta\Theta^{s,i}_n$, can be related to the parameters we are solving for via

$$\left(N^s_{n,n}\right)^{-1} S^{s,i}_{n,j} \cdot \Delta A^{s,i+1}_j = \left(N^s_{n,n}\right)^{-1} \Delta\Theta^{s,i}_n \tag{8.50}$$

$$\left(S^T_{j,n}\right)^{s,i} \left(N^s_{n,n}\right)^{-1} S^{s,i}_{n,j} \cdot \Delta A^{s,i+1}_j = \left(S^T_{j,n}\right)^{s,i} \left(N^s_{n,n}\right)^{-1} \Delta\Theta^{s,i}_n \tag{8.51}$$

The assumption that is implicit here is that properly weighted geophysical parameter errors, $\left(N^s_{n,n}\right)^{-1} \cdot \sum_g \pm E^{s,i}_{n,g}$, are uncorrelated with the parameters we are trying to solve for. That is, the properly weighted equation is one that has the smallest standard deviation.

The change required to the parameters can be solved in a weighted least-squares sense. If there were no damping then the solution would be given by

$$\Delta A^{s,i+1}_j(0) = \left[\left(S^T_{j,n}\right)^{s,i} \left(N^s_{n,n}\right)^{-1} S^{s,i}_{n,j}\right]^{-1} \cdot \left(S^T_{j,n}\right)^{s,i} \cdot \left(N^s_{n,n}\right)^{-1} \cdot \Delta\Theta^{s,i}_n \tag{8.52}$$

however, this solution would be highly unstable, given the under-determined nature of atmospheric retrievals. As shown in Section **??**, the adjustment to the parameters is found by solving for the eigenvalues, $\lambda^{s,i}_k$, and eigenvector transformation matrix, $U^{s,i}_{j,k}$, of $\left(S^T_{j,n}\right)^{s,i} \left(N^s_{n,n}\right)^{-1} S^{s,i}_{n,j}$, such that

$$\Lambda^{s,i}_{k,k} \equiv \left(U^T_{k,j}\right)^{s,i} \left(S^T_{j,n}\right)^{s,i} \left(N^s_{n,n}\right)^{-1} S^{s,i}_{n,j} U^{s,i}_{j,k} \tag{8.53}$$

See Press *et. al* 1986, pgs. 350-363 for FORTRAN routines to compute $\lambda^{s,i}_k$ and $U^{s,i}_{j,k}$. The 2-d matrix $\Lambda^{s,i}_{k,k}$ has only diagonal elements equal to $\lambda^{s,i}_k$. The transformation matrix, $U^{s,i}_{j,k}$, can be thought of as a transformed sensitivity matrix given by $S^{s,i}_{n,j} \cdot U^{s,i}_{j,k}$. At this point in the derivation we have not changed anything except how we are computing the inverse. Note that when computing $\left[\Lambda^{s,i}_{k,k}\right]^{-1}$ any components of $\lambda_k < (0.05)^2 \cdot \lambda^s_c$ are set to zero, that is we remove the singular values. When $\lambda_k$ is approaching zero both the numerator and denominator are tending toward zero. Therefore, setting those components of $\Delta A^{s,i+1}_k(0)$ to zero is most logical.

$$\Delta A^{s,i+1}_j(0) = U^{s,i}_{j,k} \cdot \frac{1}{\lambda^{s,i}_k} \cdot \left(U^T_{k,j}\right)^{s,i} \cdot \left(S^T_{j,n}\right)^{s,i} \cdot \left(N^s_{n,n}\right)^{-1} \cdot \Delta\Theta^{s,i}_n \tag{8.54}$$

We can utilize these new *optimal* functions to compute a change made in transformed parameter space, is given by $\Delta B^{s,i+1}_k(0)$. Solving Eqn. 8.61

$$\Delta\Theta^{s,i}_n = S^{s,i}_{n,j} \cdot U^{s,i}_{j,k} \cdot \Delta B^{s,i+1}_k(0) \tag{8.55}$$

$$\left(N^s_{n,n}\right)^{-1} \cdot \Delta\Theta^{s,i}_n = \left(N^s_{n,n}\right)^{-1} \cdot S^{s,i}_{n,j} \cdot U^{s,i}_{j,k} \cdot \Delta B^{s,i+1}_k(0) \tag{8.56}$$

$$\left(U^T_{k,j} \cdot S^T_{j,n}\right)^{s,i} \cdot \left(N^s_{n,n}\right)^{-1} \cdot \Delta\Theta^{s,i}_n = \left(U^T_{k,j} \cdot S^T_{j,n}\right)^{s,i} \cdot \left(N^s_{n,n}\right)^{-1} \cdot S^{s,i}_{n,j} \cdot U^{s,i}_{j,k} \cdot \Delta B^{s,i+1}_k(0) \tag{8.57}$$

$$\left(U^T_{k,j}\right)^{s,i} \cdot \left(S^T_{j,n}\right)^{s,i} \cdot \left(N^s_{n,n}\right)^{-1} \cdot \Delta\Theta^{s,i}_n = \Lambda^{s,i}_{k,k} \cdot \Delta B^{s,i+1}_k(0) \tag{8.58}$$

$$\Delta B_k^{s,i+1}(0) = \left[\Lambda_{k,k}^{s,i}\right]^{-1} \cdot \left(U_{k,j}^T\right)^{s,i} \cdot \left(S_{j,n}^T\right)^{s,i} \cdot \left(N_{n,n}^s\right)^{-1} \cdot \Delta\Theta_n^{s,i} \quad (8.59)$$

$$\Delta B_k^{s,i+1}(0) = \frac{1}{\lambda_k^{s,i}} \cdot \left(U_{k,j}^T\right)^{s,i} \cdot \left(S_{j,n}^T\right)^{s,i} \cdot \left(N_{n,n}^s\right)^{-1} \cdot \Delta\Theta_n^{s,i} \quad (8.60)$$

Again, note that when computing $\left[\Lambda_{k,k}^{s,i}\right]^{-1}$ any values of $\Delta B_k^{s,i+1}(0)$ are set to zero when $\lambda_k < (0.05)^2 \cdot \lambda_c^s$. When $\lambda_k$ is approaching zero both the numerator and denominator are tending toward zero, therefore, setting $\Delta B_k^{s,i+1}(0)$ to zero is most logical.

And we note that the transformed parameters are related to the original parameters by the eigenvectors.

$$\Delta\Theta_n^{s,i} = S_{n,j}^{s,i} \cdot \Delta A_j^{s,i+1} = S_{n,j}^{s,i} \cdot U_{j,k}^{s,i} \cdot \Delta B_k^{s,i+1} \quad (8.61)$$

Eqn. 8.61, that is, that $\Delta A_j^{s,i+1} = U_{j,k}^{s,i} \cdot \Delta B_k^{s,i+1}$, is also a statement that the original functions Eqn. 8.36 have been transformed to new *optimal* functions

$$X_L^{s,i+1} = X_L^{s,i} + \sum_j \left(F_{L,j}^s \otimes \Delta\hat{A}_j^s\right) \cdot \Delta A_j^{s,i+1} = \sum_j \left(F_{L,j}^s \otimes \Delta\hat{A}_j^s\right) \cdot U_{j,k}^{s,i} \cdot \Delta B_j^{s,i+1} \quad (8.62)$$

If no damping is required the change made in transformed parameter space, is given by $\Delta B_k^{s,i+1}(0)$. Combining Eqn. 8.52 and Eqn. 8.61 yields

$$\Delta A_j^{s,i+1}(0) = U_{j,k}^{s,i} \cdot \Delta B_k^{s,i+1}(0) = U_{j,k}^{s,i} \cdot \frac{1}{\lambda_k^{s,i}} \cdot \left(U_{k,j}^T\right)^{s,i} \cdot \left(S_{j,n}^T\right)^{s,i} \cdot \left(N_{n,n}^s\right)^{-1} \cdot \Delta\Theta_n^{s,i} \quad (8.63)$$

The changes can be damped by adding a value of $\Delta\lambda_k^{s,i}$ to the $\lambda_k^{s,i}$ such that $\lambda_k^{s,i} \geq \lambda_c^s$. This limits the noise in $\Delta B$ to a maximum value,

$$\delta B_{max}^s \equiv \frac{1}{\sqrt{\lambda_c^s}} \quad \text{or} \quad (8.64)$$

$$\lambda_c^s \equiv \left(\frac{1}{\delta B_{max}^s}\right)^2 \quad (8.65)$$

The damping parameter, $\delta B_{max}^s$ is determined empirically for each step and will be discussed in more detail in the next section (see Eqn. **??**).

Therefore, the fraction of the transformed function solved for is defined as

$$\phi_k^{s,i} \equiv \frac{\lambda_k^{s,i}}{\lambda_k^{s,i} + \Delta\lambda_k^{s,i}} \quad (8.66)$$

which is a diagonal matrix and where $\phi_k^{s,i} = 0$ represents a parameter which is completely damped and $\phi_k^{s,i} = 1$ is completely solved for. For completely damped eigenvalues, the change to the geophysical parameters is set to zero and the first guess is unchanged for that component of the solution.

The size of $\lambda_k^{s,i}$ and, therefore, $\lambda_c^s$ will be proportional to the size of the perturbation functions, $\Delta\left(\hat{A}_j^s\right)^2$ (see Eqn. 8.37 or Eqn. 8.40).

The degrees of freedom (d.o.f.) is given by the sum of the significant eigenvalues. Given that we are employing damping, the d.o.f. is given by

$$\text{d.o.f.} \quad = \quad \sum_{k=1}^{K} \phi_k^{s,i} \quad = \quad \sum_{k=1}^{K} \frac{\lambda_k^{s,i}}{\lambda_k^{s,i} + \Delta\lambda_k^{s,i}} \tag{8.67}$$

The damped change made to the transformed parameters is given by $\Delta B_k^{s,i+1} \equiv \phi_k^{s,i} \cdot \Delta B_k^{s,i+1}(0)$ which makes the damped change equal to

$$\Delta A_j^{s,i+1} = U_{j,k}^{s,i} \cdot \Delta B_k^{s,i+1} = U_{j,k}^{s,i} \cdot \phi_k^{s,i} \cdot \frac{1}{\lambda_k^{s,i}} \cdot \left(U_{k,j}^T\right)^{s,i} \cdot \left(S_{j,n}^T\right)^{s,i} \cdot \left(N_{n,n}^s\right)^{-1} \cdot \Delta\Theta_n^{s,i} \tag{8.68}$$

Therefore, the difference between $\Delta A_j^{s,i+1}$ and $\Delta A_j^{s,i+1}(0)$ is the amount of the solution we did not believe. If Eqn. 8.68 is to be iterated we will ultimately believe all of $\Delta A_j^{s,i+1}(0)$. Therefore, we need to adjust the radiances. First, we will discuss how to compute the damping, $\Delta\lambda_k^{s,i}$.

## 8.7 Rejection Criteria

A profile is rejected if any of the conditions itemized below is true. The # refers to the step # in Table 8.2.

- a row of $S_{n,j}^{s,i}$ is zero. That is all $S_{n,j}^{s,i}$ for a given $j$ are zero in any step.
- determined cloud fraction within AMSU footprint exceeds 80% (step # 18).
- cloud clearing quality indicator (etarej in previous chapter) exceeds 1.75 on the cloud clearing after the NOAA regression (step # 12).
- Effective amplification factor exceeds 10.
- the final temperature profile (step # 21) and the temperature profile from the preceding AMSU temperature retrieval (step # 17) disagree in the RMS of the bottom two 1-km layers by 2°.

$$\left[\frac{1}{2}\sum_{k=1}^{2}\left(F_{L,k}^s \otimes T_L^{s=21} - F_{L,k}^s \otimes T_L^{s=17}\right)^2\right]^{\frac{1}{2}} \geq 2^\circ \tag{8.69}$$

  where $F_{L,k}^s$ are two functions that averages the lower $\approx$ 1 km layers.

- the RMS of O-C brightness temperatures exceed 1.75 for a sub-set of AMSU channels (currently AMSU channels 3, 4, 5, 6, 7, 8, 9, 10, 11 are used after step # 21)

$$\left[\frac{\sum_{n=1}^{L}\left(\frac{1}{\text{NE}\Delta\text{T}}\right)^2\left(\Theta_{n,CCR} - \Theta_n(X_L^{s=21})\right)^2}{\sum_{n=1}\left(\frac{1}{\text{NE}\Delta\text{T}}\right)^2}\right]^{\frac{1}{2}} \geq 1.75^\circ \tag{8.70}$$

- if the amplification factor exceeds 2.0 **and** the retrieval cloud fraction is between 65% and 80% **and** there is more than 10% of the cloudiness with cloud top pressure exceeding 500 mb after step # 19.
- quality indicator from final surface retrieval exceeds 1.25 (step # 20)
- quality indicator from final temperature retrieval exceeds 1.25 (step # 21)

## 8.8 References

Backus, G. and F. Gilbert 1970. Uniqueness in the inversion of inaccurate gross earth data. Phil. Trans. Roy. Soc. Lond. **266** p.123-192.

Ben-David, A., B.M. Herman and J.A. Reagan 1985. Accuracy limitations in satellite temperature retrievals in the 14.0 um $CO_2$ band. in Adv. in Remote Sensing Retrieval Methods (Deepak,Fleming,Chahine) p.233-245.

Conrath, B.J. 1977. Backus-Gilbert theory and its application to retrieval of ozone and temperature profiles. in "Inversion Methods in Atmospheric Remote Sounding (ed. Deepak) p.155-193.

Conrath, B.J. 1972. Vertical resolution of temperature profiles obtained from remote sensing radiation measurements. J. Atmos. Sci. **29** p.1262- 1271.

Hansen, P.C. 1992. Analysis of discrete ill-posed problems by means of the L-curve. SIAM Review v.34 p.561-580.

Kaplan, L.D., M.T. Chahine, J. Susskind and J.E. Searl 1977. Spectral band passes for a high precision satellite sounder. Applied Optics **16** p.322-324.

Schimpf, B. and F. Schreier 1997. Robust and efficient inversion of vertical sounding atmospheric high-resolution spectra by means of regularization. J. Geophys. Res. v.102 p.16037-16055.

Susskind, J., C.D. Barnet and J.M. Blaisdell 2003. Retrieval of atmospheric and surface parameters from AIRS/AMSU/HSB data in the presence of clouds. IEEE Trans. Geosci. Remote Sens. v.41 p.390-40.

Susskind, J., C.D. Barnet and J. Blaisdell 1998. Determination of atmospheric and surface parameters from simulated AIRS/AMSU sounding data: Retrieval methodology and cloud clearing methodology. Adv. Space Res. v.21 p.369-384.

# Chapter 9

# Preliminary Validation Results

In this chapter we perform a thorough validation analysis on the performance of the temperature, water vapor, cloud clearing and trace gas products. We will first concentrate on a global focus day test bed of NUCAPS data acquired on May 15th 2012. For this analysis we will use co-located model analysis (ECMWF and GFS) as a reference truth. At this stage of the NPP mission we have just started collecting dedicated radiosondes that allow for an independent measurement of the atmospheric state which also provides a superior spatial and temporal collocation with respect to the model analysis.

## 9.1 Validation results from focus day May 15 2012

For this analysis we will use co-located ECMWF analysis profiles as a reference truth for temperature and water vapor. Due to a temporary unavailability of ECMWF ozone profiles, we will use GFS data for the validation of ozone.

ECMWF analysis profiles are available with a frequency of 6 hours per day. Although a temporal interpolation among two consecutive analyses that will match the satellite overpass would be preferable, we simply acquire the temporally closest analysis profile because computationally less compelling. For an accurate analysis, it is important then to understand the impact of the temporal mismatch between the retrieval and model on the validation statistics. We begin then by differencing two ECMWF analysis times (0 and 6Z) to effectively get the atmospheric change occurring over a time span of 6 hours at each grid cell. This is shown in figure 1a for 850mb temperature and in figure 1c for 850mb moisture (units are expressed as percentage change in 6 hours). These two figures illustrate that while globally many regions of the Earth do not see significant change over 6 hours (light green regions), some cases have significant changes that will significantly affect the statistics (blue and red regions).

We then computed the amount of time required, , to exceed a given threshold. The thresholds were set to 0.5K for temperature and 5% for moisture change. These thresholds are approximately the level at which the statistics would be noticeably affected. We then look at the distribution of the number cases in Fig. 1a and 1c as a function of . In Fig. 1b and 1c we show the cumulative distribution as a function of time and a expanded view near zero. We see that for 850 mbar temperature 20% of the global cases exceed this threshold when  is about 12 minutes (0.2 hour in the plot). For moisture, 20% of the global cases exceed the threshold in  equal to about 2 minutes (0.03 hour in the plot). These results should be kept in mind when interpreting the statistical results that we are about to present. In other words, this analysis should also be a reminder that significant changes in the atmospheric fields can occur in short time frames and use of forecasts

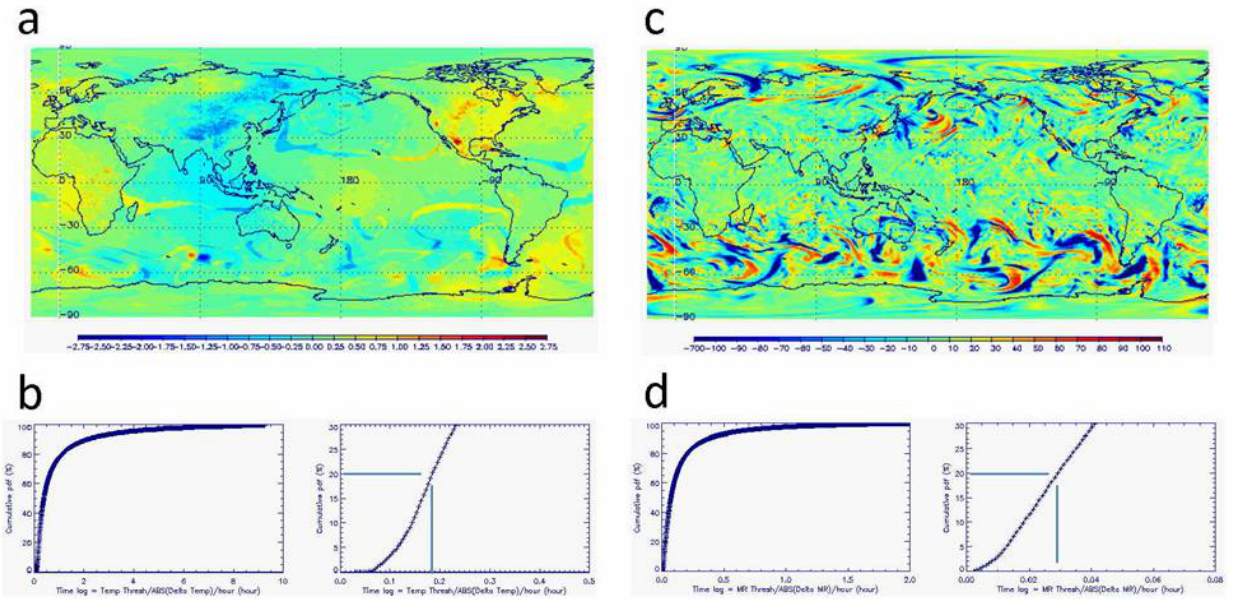


Figure 9.1: Difference of the 6Z and 0Z ECMWF analysis is shown for 850 mbar temperature (Fig. 1a, Kelvin) and 850 mbar moisture (Fig. 1c, % change) for May 15, 2012. The cumulative distribution of the number of cases exceeding a threshold (see text) is shown for temperature (Fig. 1b) and moisture (Fig. 1c) as a function of the time required to exceed that threshold. Lines indicate where 20% of the cases would be exceeding this threshold ( approximately equal to 0.2 hour for temperature and approximately equal to 0.03 hour for moisture).

or other in-situ data for performance characterization is best determined by dedicated radiosondes launched near satellite overpass times.

### 9.1.1 RMS and BIAS statistics results over different geophysical regimes

In the following, we provide an overview of RMS and BIAS validation results using the full focus day of NUCAPS retrieval data over the global (figure 2), tropical (figure 3), mid latitude (figure 4) and polar region (figure 5). Each group of figures is separated into RMS (top) and BIAS (bottom) statistics. Left figure is for temperature, center figure is for water vapor (both respect to ECMWF used as truth). The right figure is for ozone statistics (using the GFS model as truth).

NUCAPS results are shown in red. Solid lines are for the final physical retrieval, while dash lines are for the first guess. For completeness, we are plotting AIRS results using both the operational version 6 (blue curves, from now on referred to as "v6") and the off-line research code equivalent to NUCAPS (cyan curves, from now on referred to as "v5.9").

The vertical red bars in figure 2 (top part) indicate the specification requirements of the CrIMSS JPSS program. The first and most important observation that can be made is that NUCAPS global RMS and BIAS temperature, water vapor and ozone statistics generally meet the required specifications. After only one year in orbit, NUCAPS RMS and BIAS performance is comparable to the AIRS products (both AIRS v5.9 and v6) which have more than 10 year of maturity. NUCAPS

global acceptance yield (top left side on the temperature figure) is about 60%, while AIRS v5.9 is 75%. They both use the same rejection criteria. AIRS v6 yield is based on a different criterion and amounts to 86%. Possible sources of difference in the acceptance yield and retrieval performance are: AIRS v6 has improved surface emissivity first guess; AIRS v5.9 has a multi-year temperature and water vapor first guess regression training; AIRS radiance tuning uses a dedicated RAOB training ensemble; AIRS retrieval quality controls are fully optimized. These aspects are element of work in progress for NUCAPS.

We also separate ocean and land (figure 6) and day night ensembles (figure 7). The results we find are consistent with what observed above and are in support of the stability of the NUCAPS product.

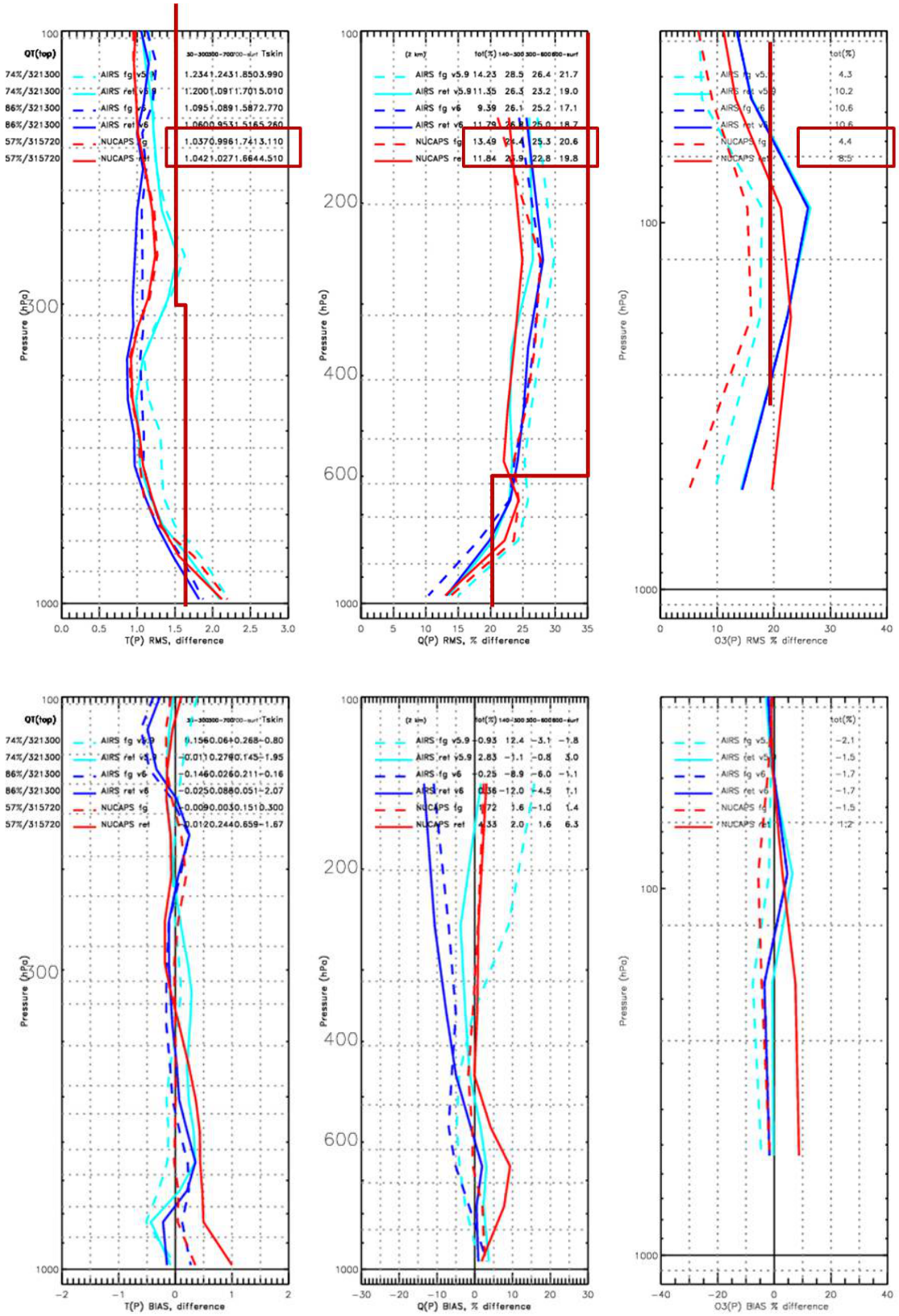


Figure 9.2: RMS (top) and BIAS(bottom) global statistics for temperature (left) , water vapor (center) and ozone (right). Solid curves are for the final physical retrieval, dash lines are for the first guess. Red curve is for NUCAPS, blue is for AIRS v6 and cyan is for AIRS v5.9. See text for details.

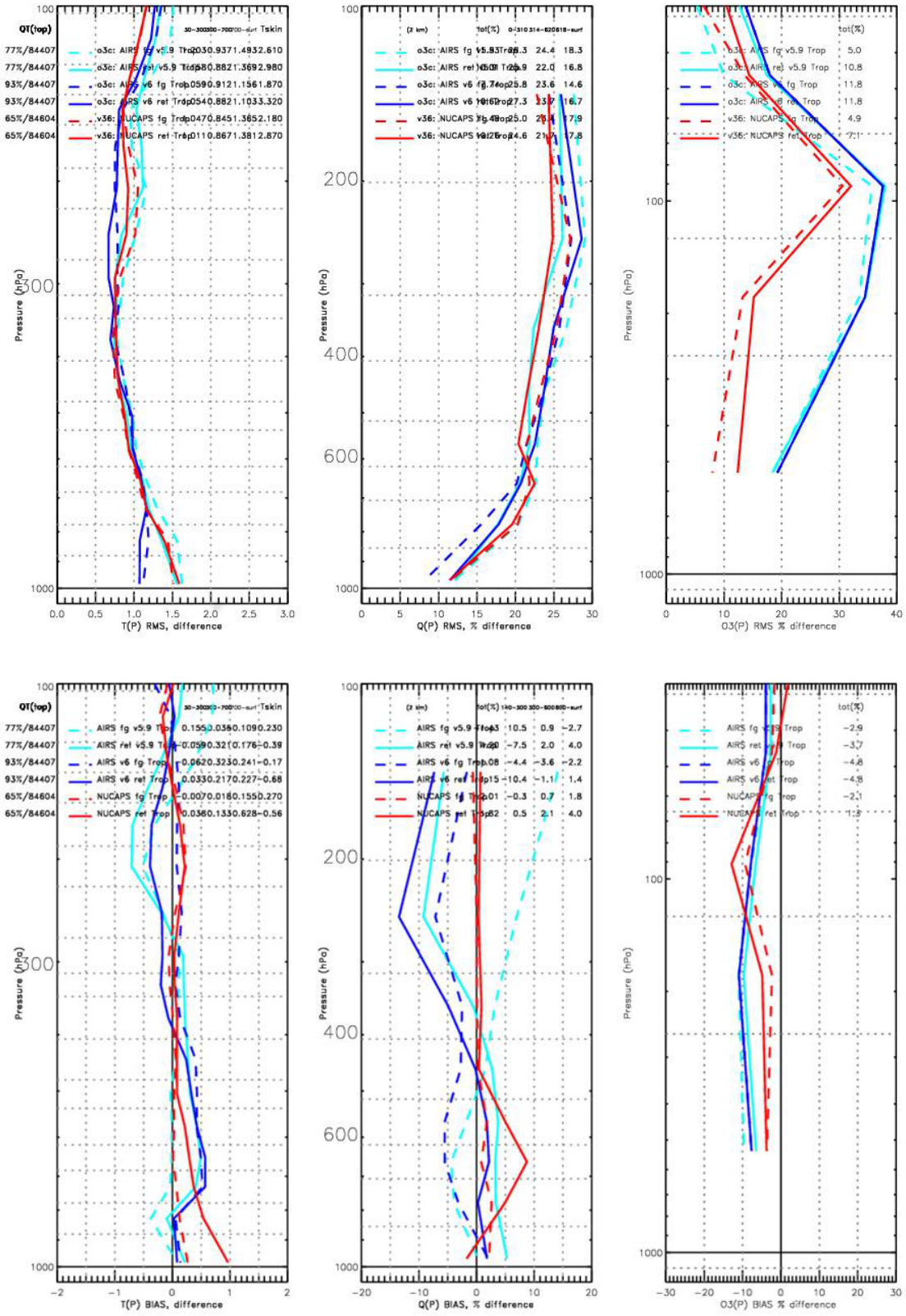


Figure 9.3: Same as figure 2, but for tropical regimes.

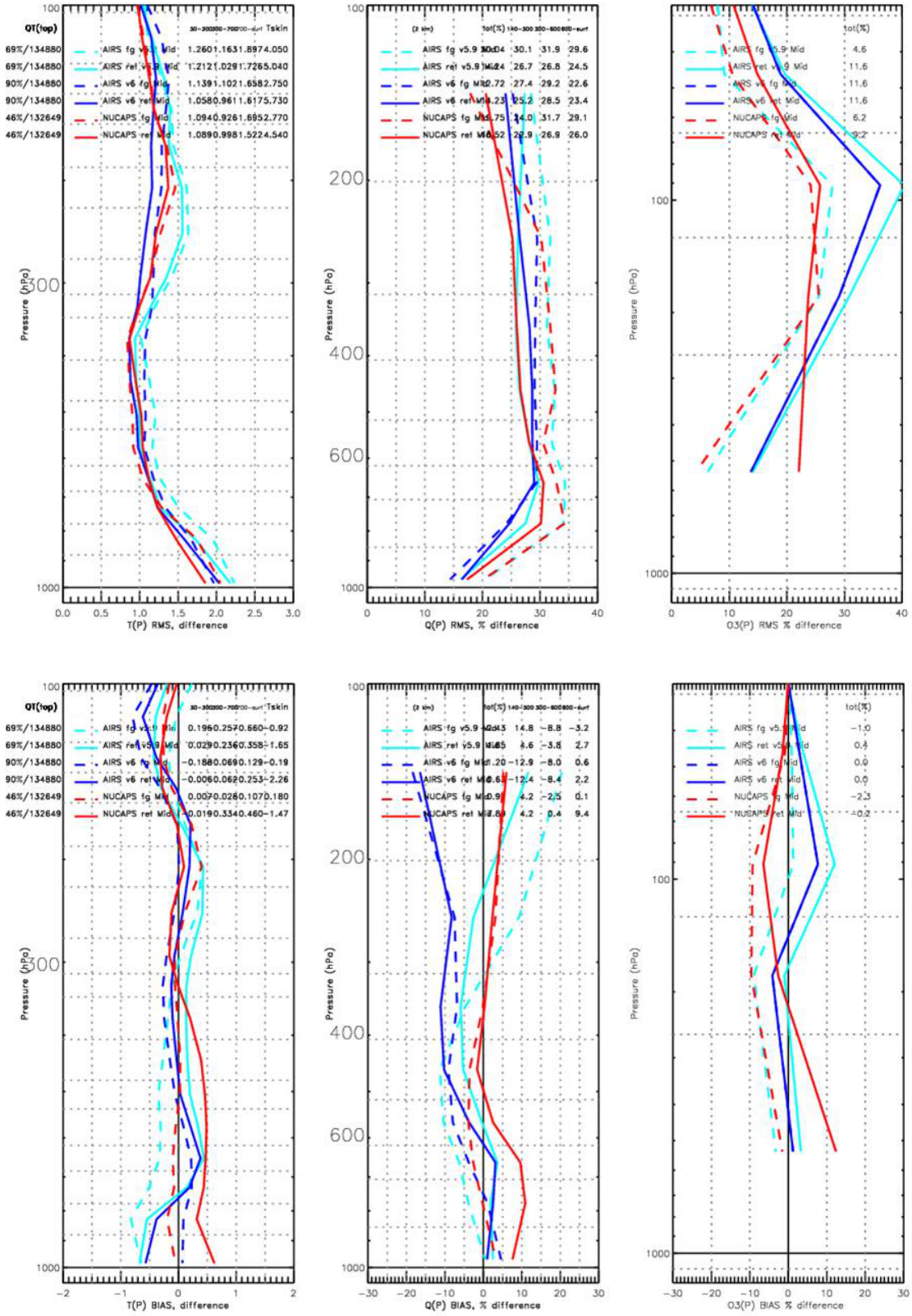


Figure 9.4: Same as figure 2, but for mid-latitude regimes.

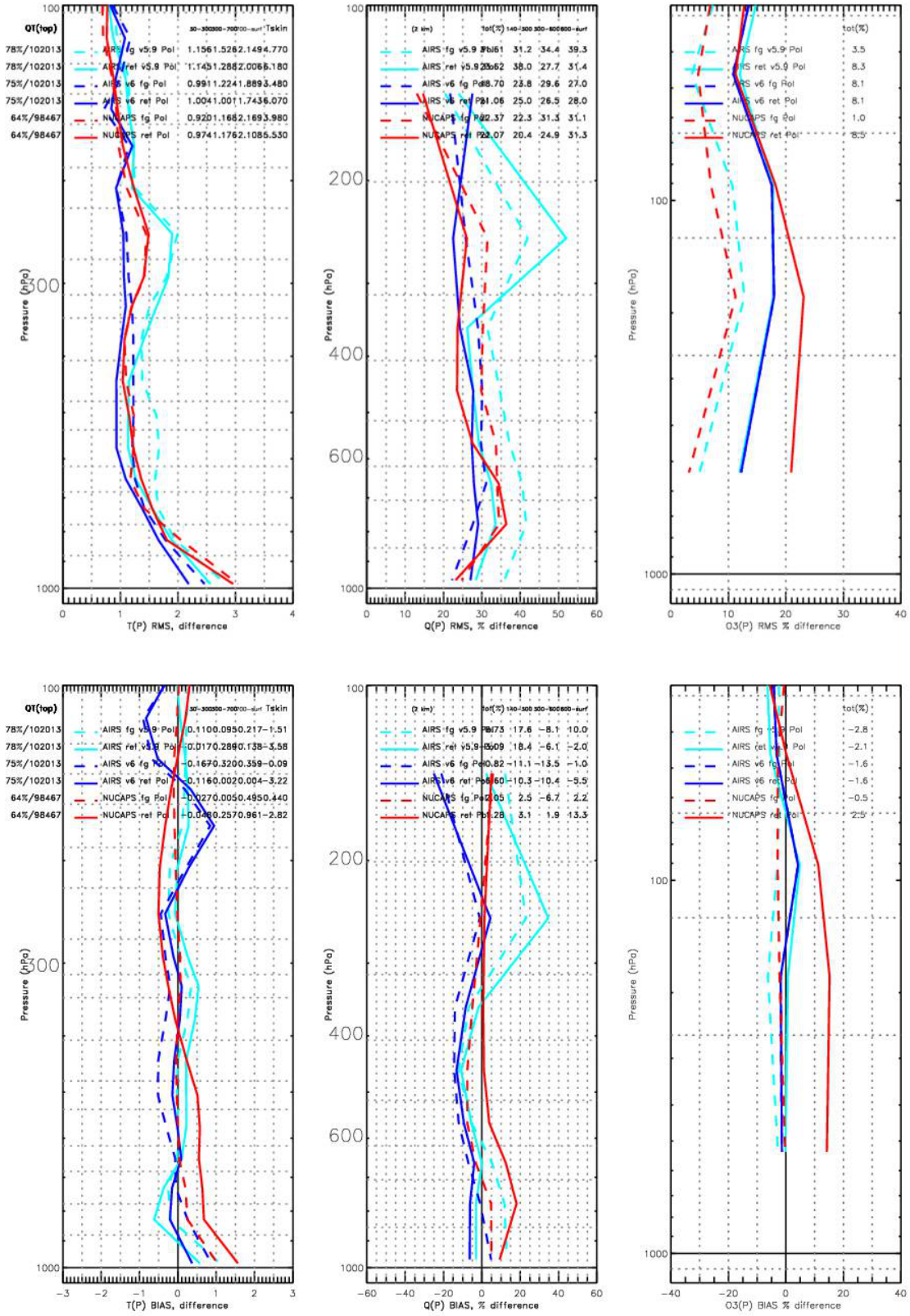


Figure 9.5: Same as figure 2, but for polar regimes.

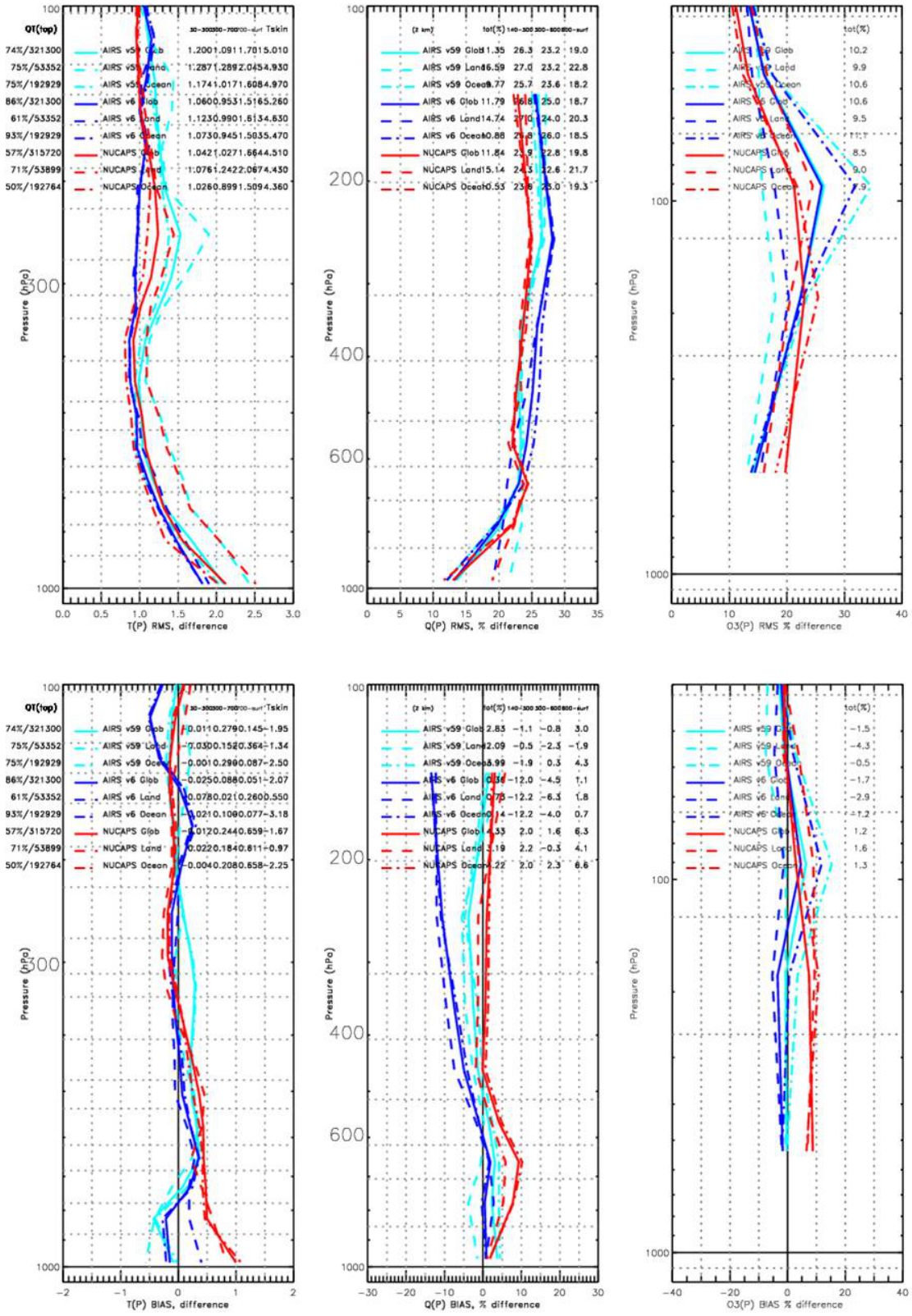


Figure 9.6: Same as figure 2, solid is global, dash is night and dash-dot is day regimes.

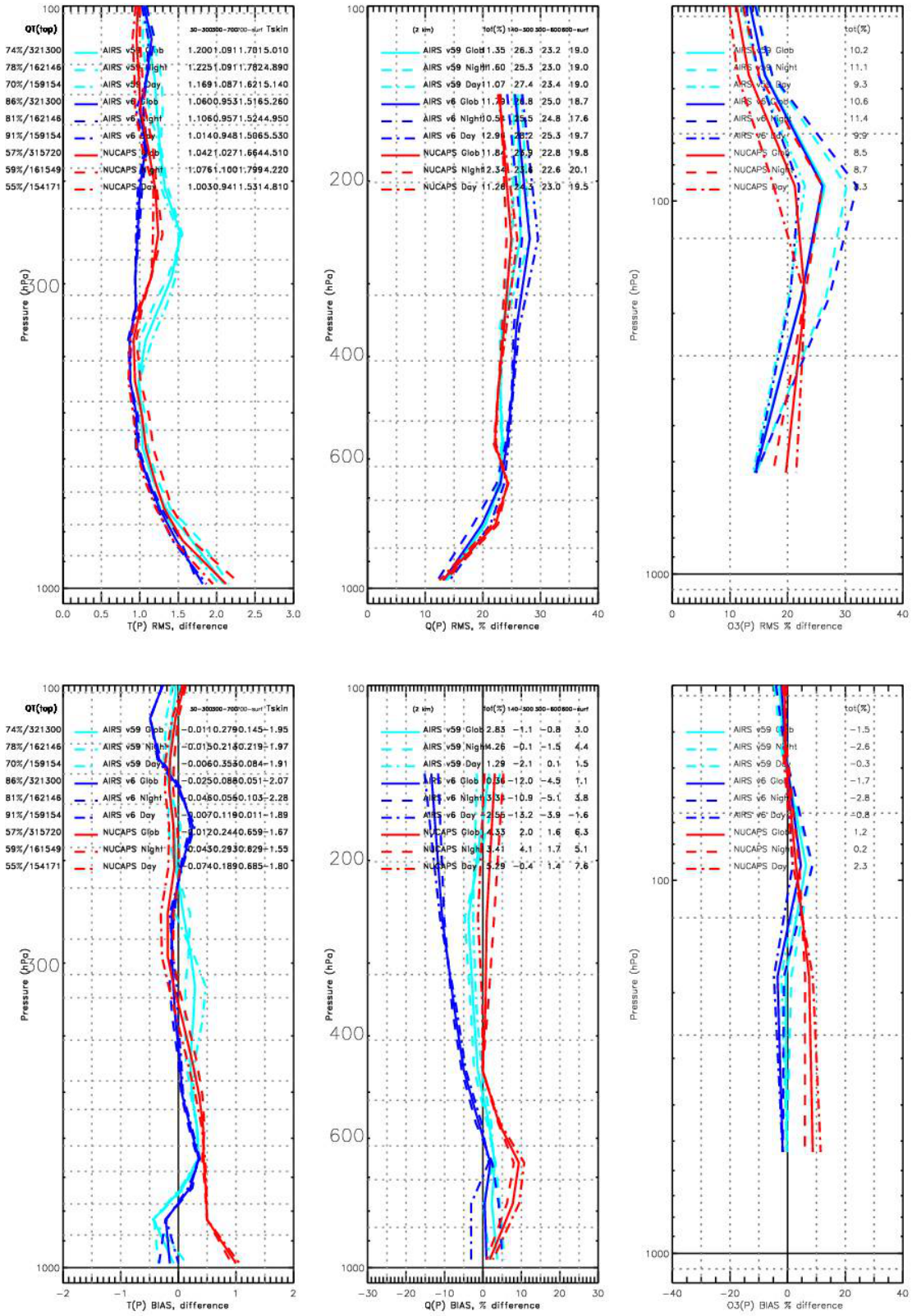


Figure 9.7: Same as figure 2, solid is global, dash is land and dash-dot is ocean regimes.